A Numerical Model of the Cardiovascular System for Clinical Assessment of the Hemodynamic State

by

Edwin Tomoya Ozawa

Master of Science in Mechanical Engineering
(Massachusetts Institute of Technology, 1992)

Submitted to the Department of Health Sciences and Technology,
Medical Engineering - Medical Physics
in partial fulfillment of the requirements for the degree of
Doctor of Philosophy in Medical Engineering

at the

MASSACHUSETTS INSTITUTE OF TECHNOLOGY
September 1996

Author .....
Department of Health Sciences and Technology
August 16, 1996

Certified by .....
Roger D. Kamm
Professor of Mechanical Engineering
Thesis Supervisor

Accepted by .....
Martha L. Gray
Associate Professor of Electrical Engineering
Chairman, Departmental Committee on Graduate Studies

A Numerical Model of the Cardiovascular System for Clinical Assessment of the Hemodynamic State

by

Edwin Tomoya Ozawa

Submitted to the Department of Health Sciences and Technology, September 1996
in partial fulfillment of the requirements for the degree of

Doctor of Philosophy in Medical Engineering

Abstract

A robust and comprehensive numerical model of the cardiovascular system has been developed to assess the effects of cardiovascular disease, and of various mechanical and pharmaceutical interventions, on the hemodynamic parameters of patients. Such a model would provide the clinician with a more refined method of non-invasively determining the hemodynamics than is currently available in practice. The model was based upon a numerical solution of the one-dimensional equations of motion in a geometrically accurate branching network of the arterial system including energy losses at bifurcations, a ventricular model incorporating specified time-dependent wall compliances and unidirectional valves, and lumped parameter venous and pulmonary circulatory systems. Also incorporated are damping mechanisms related to the phase dependence of the wall shear during periodic flows, and the viscoelastic behavior of the arterial walls, both of which have been shown to be physiologically important. The model is capable of reproducing the complex waveforms observed *in-vivo*, and agrees well with literature and measured waveforms obtained by the author.

System identification techniques were then applied to the model in order to obtain a method to quantitatively assess the hemodynamic state of a patient, as a function of hemodynamic parameters which are of interest to the clinician. A set of six governing model parameters were identified through a sensitivity analysis of all model parameters, followed by model simplification and non-dimensionalization. A library of data was then constructed using 337 runs of the model, varying each of the parameters independently over discrete grid points in the six-dimensional space. The proposed parameter estimation scheme makes use of the parameter space-containing library to construct *surrogates* (approximations of the actual functions) to describe the behavior of "features" extracted from the computed waveforms at each grid point. Thus, if a feature set is created from the patient waveforms to be tested, this set of feature functions can be solved for iteratively to determine the six unknowns (governing parameters) unique to the specified feature set.

The parameter identification technique was tested first against a number of generated runs corresponding to random positions in the parameter space. The parameter estimation scheme was able to estimate values of peripheral resistance within 5% error, given that the ill-defined nature of the features as a function of parameters can be somewhat overcome by specifying one or more of the parameters (such as central venous

pressure or heart rate). The heart failure patient data sets obtained by the author for model validation were applied to the present estimation scheme, which pointed the way for future directions of improvement. Thus, this thesis demonstrates the strong potential of the proposed scheme to clinically measure numerous hemodynamic parameters. Further work will have to be performed to obtain a robust system capable of estimating six or more hemodynamic parameters with little error.

Thesis Supervisor:

Roger D. Kamm, Ph.D.
Title: Professor of Mechanical Engineering, Department of Mechanical Engineering, Massachusetts Institute of Technology.

Thesis Committee:

Richard T. Lee, M.D.
Title: Director, Non-invasive Cardiac Laboratory, Brigham and Women's Hospital; Assistant Professor of Medicine, Harvard Medical School.

Roger G. Mark, M.D., Ph.D.
Title: Grover M. Hermann Professor of Health Sciences and Technology, Harvard-M.I.T. Division of Health Sciences and Technology; Professor of Electrical Engineering, Department of Electrical Engineering and Computer Science, Massachusetts Institute of Technology.

Ascher H. Shapiro, Sc.D.
Title: Professor Emeritus, Department of Mechanical Engineering, Massachusetts Institute of Technology.

Acknowledgments

There are many people which have helped me through the years, but first I want to start with those who have helped me make my work germinate and flourish.

Firstly, I want to thank my advisor, Dr. Roger Kamm, for all of his patience and for guiding me through what will probably be the hardest thing I have ever done in my life. I also want to thank my committee members; Dr. Roger Mark, who was the first person I met when I came to visit HST as a prospective student many years ago, and who helped me onto the path to medical school; Dr. Richard Lee, who introduced me to the realities of clinical research and the daily life of a practicing cardiologist; and Professor Shapiro, for his great insight, and who has in many ways acted like a father in guiding and encouraging this work.

I also owe much to Dr. Mariano Gurfinkel, since the idea of applying parameter estimation to the problem of hemodynamic measurement was really his idea from the start. Also, I want to thank Dr. Serhat Yesilyurt who developed much of the ideas and techniques behind the parameter estimation for his own thesis, and who made development of the system outlined in this thesis much less painful than it could have been. Thanks to Dr. Luis Rosario and Dr. Michael McConnell, both of whom were instrumental in the clinical study.

I also wish to thank all of the members of my lab who made life enjoyable and unforgettable over the years. I also want to thank all of the administration, faculty, and all of my friends in the HST program. Some of the best times of my life were spent at M.I.T., and I will miss you all.

Table of Contents

List of Figures

List of Tables

Chapter 1

Introduction

1.1 The Arterial Pressure Pulse

Throughout history, physicians have always looked towards the "pulse" as a source of information, a window onto the state of health of their patients. When one speaks of the pulse, or "taking one's pulse," the image that readily comes to mind is that of the two forefingers of one hand, firmly positioned over the radial artery at the wrist. This procedure is known in the medical lingo as "palpation." An image of what appears to be the hand of God palpating the wrist of Man is incorporated into the seal of the Royal College of Physicians of London (Figure 1.1), and harks back to an earlier day in medicine when physicians had to rely solely on the five senses to gain information and clues regarding the health of their patients. In modern times, palpation of the pulse is not expected to yield much more information than the heart rate, possibly the strength of the heart's contraction. Doctors nowadays will write, for example, "pulse 72, RRR" in their patient's charts, referring to 3 pieces of information that are garnered from feeling the pulse: one, that the heart rate is 72 beats per minute (normal); two, that the rate is regular (i.e. the heart rate does not appear to deviate significantly over the course of palpation); and three that the *quality* of the pulse, or the rhythm, is also normal. Hence the abbreviation RRR: Regular Rate and Rhythm. One should note that although we speak of the pulse as a manifestation of pressure, the pulse as a description of velocity or flow rate as a function of time through a vessel is equally as valid.

The quality of the pulse was once a more important piece of information before the advent of technologies that now allow for accurate imaging and quantification of the cardiovascular system. The ancient Chinese, for instance, believed that a competent physician could diagnose disease, detect pregnancy, and even determine the sex of the unborn child from palpating the pulse. The examination of the pulse took on a mystical quality in many cultures, including the Hindu as well as the Chinese, where pronouncements made on the feel of the pulse was based more on a tried and true art than on real science. The examination of the patient was introduced by the Greek

Figure 1.1. Crest of the Royal College of Physicians of London. From O'Rourke, 1992.

philosopher and physician Hippocrates, who categorized the pulse based on its correlation to known disease states. Among his contemporaries was the great physician Galen, who noted the relationship between the heart, vessels, and blood: a revolutionary idea for his time, when it was commonly believed that arteries transported air, rather than fluid, around the body.

The understanding of the circulation increased as time progressed, and science became more formalized during the "Age of Enlightenment." The evolution of cardiovascular physiology is highlighted by the first complete description of the cardiovascular system as a closed loop network of tubes transporting blood, by William Harvey in 1628, published in the monograph "An Anatomical Essay on the Movement of the Heart and Blood in Animals." Harvey also described in his classical work the interaction between the contraction of the heart, and the consequent filling of the arterial system resulting in expansion of the vessel walls and the sensation of the "pulse" (O'Rourke, 1992). It is fitting that the seal of the Royal College of Physicians bears tribute to Harvey's work, which was published while Harvey was a faculty member of the College.

One of the most important and earlier descriptions of arterial system dynamics was made by the Reverend Stephen Hales in 1769, when he recorded the arterial pressure of a horse using a fluid-filled manometer. Hales compared the ejection of blood into an elastic arterial system to that of the air-filled chamber of a fire engine, which converted pulsatile flow from the pump into a steady stream. His description of arterial compliance was given the German name "windkessel", or "air chamber", to capture the essence of the "cushioning" effect on the force of the pressure pulse that he had observed. The windkessel model translates well into an simple electrical circuit analog consisting of a single resistor and capacitor, as shown in Figure 1.2. Hale's description was soon followed by classical mathematical descriptions of fluid flow, most notably for flow in tubes by J.M. Poiseuille in the early 19th century. Poiseuille also performed experiments in cardiovascular physiology, and demonstrated using a fluid-filled manometer that differences in mean pressures between distal and proximal arteries were negligible (O'Rourke, 1992).

Eventually, measurement techniques of the arterial pulse improved over that of the manometer, which was inherently noisy and gave poor impressions of the shape of the pulse. E. Marey was the first to develop a reliable device that translated the pressure fluctuations in arteries to tracings on a rotating drum (Figure 1.3). Hence, for the first time physicians could make use of the "sphygmograph" to visually study changes in the

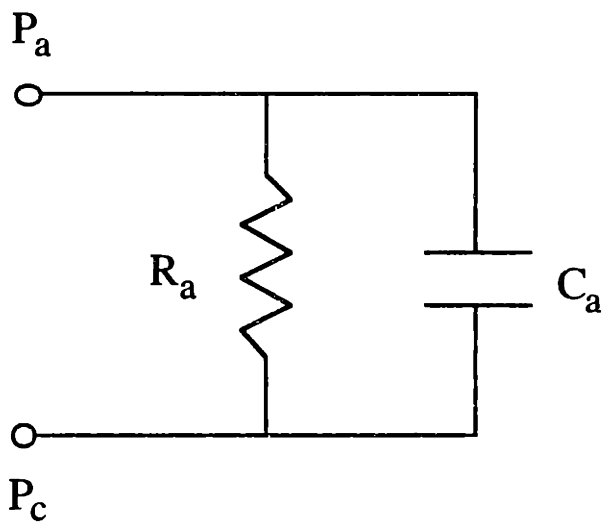

Figure 1.2. RC electrical analog of Hale's windkessel. P_a is the systemic arterial pressure, P_c is the capillary bed pressure, C_a is the systemic arterial compliance, and R_a is the systemic vascular resistance.

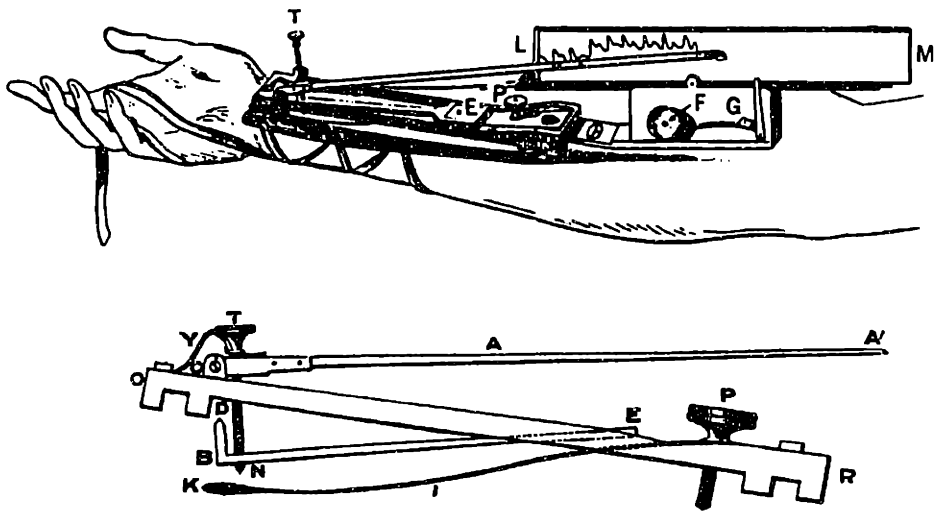

Figure 1.3. Plate of Marey's mechanical sphygmograph attached to the arm, and the tracing of the arterial pulse on the traveler labeled M. From Fishman, 1964.

pressure pulse with cardiovascular disease. This led physicians such as F.A. Mahomed in 1872 to proclaim "by his pulse you will know him." Mahomed gave a description of how the pulse changes in patients with chronic hypertension, and how through measurements and palpation one could identify patients with the ailment. The technology of blood pressure measurement advanced with the development of the sphygmomanometer in the late 19th and early 20th centuries, which completely supplanted the use of the sphygmograph. Korotkoff in 1905 described the characteristic tapping noise of blood jetting through a collapsed artery heard during auscultation with the sphygmomanometer (Fishman, 1964). This is the basis for measurement of the systolic and diastolic components of the brachial pressure pulse, and is a technique that persists to this day.

The study of the arterial pressure pulse continued with the development of devices and techniques that allow for more quantitative measurement with high signal to noise ratios. The standard clinical instrument of today is the fluid-filled catheter, a slender and hollow plastic tube with an opening at one end and a port for connection to a pressure transducer at the other. These catheters are placed intravenously or intra-arterially to monitor pressures in various locations throughout the body, particularly the radial artery, the thoracic and abdominal aorta, the left or right heart, and the pulmonary arteries. Fluid-filled catheter/transducer assemblies give highly accurate measurements of the pulse with little distortion of the true signal. Indwelling catheters allow continuous monitoring of hemodynamics at the bedside. Alterations in the hemodynamic states can therefore be quickly assessed and acted upon by the patient's caregivers.

In general, the studies of the arterial pulse to date are qualitative descriptions of how alterations in the material or mechanical properties of the arterial system affect measurable quantities. This is, of course, assuming that the arterial system can be easily modeled as a purely mechanical system, a construct of elastic tubes driven by pumps. It is simple enough to look at the plotted images of arterial pressure and flow pulses and conclude that differences do indeed exist between various states, normal or pathological (Figure 1.4). However, it may be possible to determine more quantitative information from the shape of the pulse that could be of tremendous use to the clinician. A system coupled with a model of the cardiovascular system might be constructed which analyzes the waveforms in a systematic pattern, and extracts specific values for hemodynamic parameters that are difficult or impossible to obtain directly from patients. These waveforms may be obtained by a simple, non-invasive technique such as an electronic version of the 18th century sphygmograph described above.

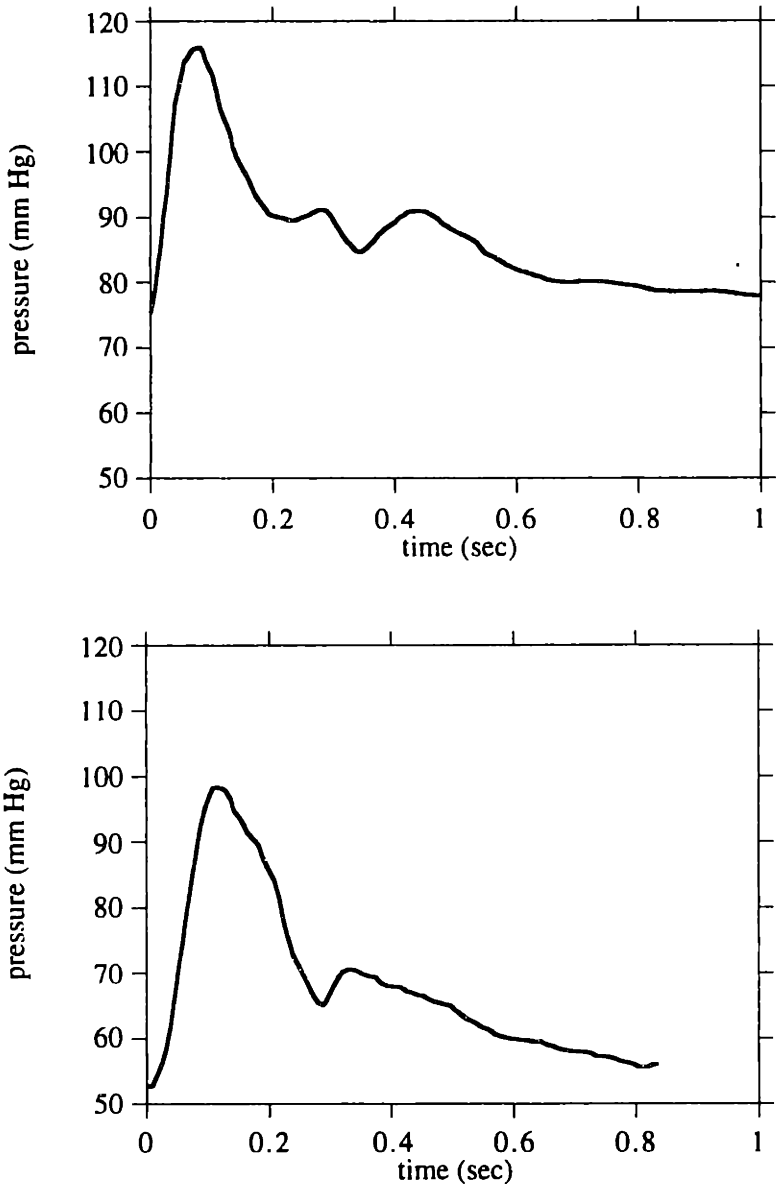

Figure 1.4. Comparison of radial pressure pulses obtained by the author in a normal individual (top) and a patient with congestive heart failure (bottom).

Our interest in the arterial pulse, then, lies in our ability to model its behavior, and how the pulse might be expected to change with *mechanical* alterations in the cardiovascular system. Furthermore, since in a model we have complete control over the theoretical equations and the coefficients that they contain, manipulation of the model hemodynamic parameters allows us the luxury of observing the close interrelationships between the pulse and these parameters. Many types of models have been developed over the years, and it is therefore worthwhile to briefly review the current literature. This will aid in determining what model may be suitable for use in this dissertation.

1.2 Previous Models of the Cardiovascular System

Numerous models of either the whole or portions of the circulation have been extensively developed in order to duplicate both qualitatively and quantitatively the observed clinical measurements and behavior. The earliest models were mechanical constructions of rubber and glass, and provided insight into the importance of both the geometry and the material properties of the cardiovascular system from a fluid mechanics point of view (Helal, 1993; McMahon, 1971; Westerhof, 1971). More recently, with the advent of computers which allow for accurate and efficient numerical modeling of dynamic systems, additional models have been developed that simulate the circulation in equal or greater detail. These models mimic the propagation of pressure and flow waves through the circulatory system, either through an electrical analog or a transmission line model. A brief glance at the literature for circulatory mechanics reveals numerous applications of numerical modeling of the circulatory system in the realms of physiology research, clinical medicine, and engineering design. Numerical modeling is useful in the investigation of changes in arterial impedance and wave propagation behavior that occur with different disease states or drug interventions. Arterial wave reflection in heart failure, for instance, is of great interest since optimal drug treatments using vasodilation should be aimed at lowering the pulse waves that return to the left ventricle from the periphery during systole, thus decreasing ventricular afterload. Additionally, flow past various circulatory abnormalities is of great interest and has been studied in extensive detail. Two particular examples include the study of the abdominal aortic aneurysm and bypass grafts, and how the local flow and pressure surrounding the abnormal regions in the main arterial tree are affected (Helal, 1994; Taylor, 1994).

Additional motivations for a circulation model stem from space physiology research, where the effects of zero gravity, tilt, and lower body negative pressure (LBNP) on the dynamics of the cardiovascular system have been extensively studied and modeled

(White, 1983). Many studies of cardiovascular control has been performed, and a large majority of these involve system identification techniques to develop expert models of the regulatory mechanisms involved. System identification allows a model to adaptively modify its parameters such that for a given series of inputs, the model output matches that of the real system with as little error as possible. Such techniques are commonly used in engineering control and design; their application to cardiovascular control mechanisms and lumped parameter models of the circulation are in common use for studying LBNP, heart rate variability resulting from regulation by the autonomic nervous system, and control of hypovolemia, to name a few applications (Symposium, 1994; White, 1983).

Studies have been conducted to investigate the interaction between the circulation and various cardiac assist devices (CAD's), which are designed to augment blood flow when the failing or diseased heart is unable to satisfy the physiological needs of the body. These devices include: the intra-aortic balloon pump (IABP), a catheter-like device tipped with an inflatable balloon which is placed into the abdominal aorta, and inflates during diastole to increase perfusion pressure and deflates just prior to systole to decrease afterload (Niederer and Schilt, 1988); the left ventricular assist device (LVAD), a mechanical pump which reduces the workload on the heart; and the external counterpulsation (ECP) device, which uses pressurized mast pants to compress the lower extremities, thereby augmenting diastolic pressures and resulting in improved coronary perfusion (Soroff et al., 1986). Research into other forms of mechanical cardiac assist is currently underway in the Fluid Mechanics Laboratory, specifically an LVAD which is being tested both computationally and on the bench. Cardiac assist devices have profound effects on the pressure and flow behavior of the arterial system, and in the case of ECP, the venous system as well.

It is fairly clear that a model, specifically a numerical one, may provide the means for understanding the connection between the measured arterial pulse and the hemodynamic parameters. As a fantasy goal, one might envision a physician using an electronic device that obtains, non-invasively, the pressure pulse from a major artery, and with the input of a few other easily measured patient parameters (age, height, weight, etc.) can generate predicted values for clinically useful hemodynamic parameters. These include the cardiac output, left ventricular peak elastances, peripheral resistance, mean arterial wall stiffness, and so forth. Such a device may also be easily integrated into standard hospital monitoring techniques, thus making unnecessary the need for traditional hemodynamic monitoring through an indweiling catheter. Much work stands in the way of the development of such a device, and the first basic steps require the construction of a system that demonstrates the *potential* ability to accomplish these goals.

1.3 Thesis Scope and Goals

In light of the potential of a complete cardiovascular model, the scope of this thesis will be structured in context with a common clinical problem involving the interactions between cardiovascular mechanics, monitoring, and medical interventions. In the clinical setting, patients are evaluated by physicians using the available hemodynamic data in order to determine the most appropriate choice of therapy. It is therefore desirable to develop a predictive clinical tool incorporating a model of the cardiovascular system such that estimations of useful hemodynamic parameters can be obtained. Thus, for this thesis a one-dimensional numerical model of the cardiovascular system was developed, founded on sound fluid mechanics principles and generic data from the literature. This model was combined with parameter estimation techniques so that hemodynamic properties could be estimated from the arterial pulse pressure obtained from patients. Such a set of clinical measurments was easily obtained using the available monitoring equipment, such as Doppler ultrasound and indwelling pressure transducer catheters. This accomplished the dual purpose of both providing the data needed to perform the parameter estimation, as well as the model validation by assessing its ability to predict the changes in behavior following a pharmaceutical perturbation.

1.3.1 Construction of a Comprehensive Model

The initial goal was the development of a computer model to emulate the pulse propagation of pressure waves and flow behavior in the human arterial tree, to include the aorta and the major branches and bifurcations to several generations. Modeling was accomplished by one-dimensional finite difference calculation of the equations of momentum and continuity, as well as a constitutive relationship for compliant vessel wall behavior. Work on compliant vessel networks has been extensively developed by our group and others (Kamm, 1982; Kimmel et al., 1988; Raines, 1972; Shapiro, 1977; Stettler et al., 1981). It is further important to note that finite difference calculations provide a greater wealth of information, as a function of anatomical position, than do corresponding lumped parameter models, which make up the majority of numerical circulation models in existence today.

Several other factors were investigated while developing this model of the arterial system. One concerned the need for appropriate representation of losses at a bifurcation. For this, the results of Collins (Collins et al., 1993) and Wolf (Wolf, 1990) obtained from experiments in branching networks were useful. Also of interest was the effect of viscoelastic artery walls and frequency-dependent wall friction in transient pipe flow. The circulation loop was closed by representing the venous and pulmonary system as a

lumped parameter model consisting of resistors and capacitors. The model also incorporated a transient compliance-based model of the left and right ventricles in order to obtain realistic waveforms both for normal and heart failure patients, the latter of which was represented by a compliance function which can be altered as a result of decreased myocardial contractility, in addition to compensatory changes in the periphery. Additionally, the effects of the autonomic nervous system by way of the baroreceptor reflex were included using a simple linear control model, as the reflex has important effects in the distribution of blood volume and the maintenance of systemic blood pressure.

1.3.2 The Model as a Diagnostic Tool

The model described above contains the physics needed to simulate the cardiovascular system, although it lacks the parameters needed to represent an individual physiological system. To a great extent, these parameters can be estimated using data from a specific patient. In this thesis system identification techniques were applied to the model in order to match selected measured waveforms taken from the literature or measured in a specific individual. Thus, given a series of measurements of velocity and pressure at selected points in the body, the parameter estimation routines described here can be applied to "eke out" model parameters such that the difference (or "error") between the computed and measured pulse waveforms is at a minimum. This can be described in loose terms as the "inverse problem," where a set of hemodynamic parameters can easily give rise to an output of pressures and flowrates using a cardiovascular model, but a solution for the parameters from a set of pressure and flow measurements becomes a much less trivial problem. The actual parameters to adjust were carefully selected so that they contained enough information to allow the model to reproduce individual features from a patient, and were few enough in number so that parameter estimation could actually be carried out with reasonable effort. For example, it is possible to characterize geometry and material properties for the entire arterial tree by specifying a small, selected number of parameters. Likewise, only a few parameters may be selected to specify arteriolar resistances and the distribution of cardiac output. System identification techniques currently in use at the Fluid Mechanics Laboratory were extremely useful in providing a method for estimation of the hemodynamics.

The model was applied clinically during a portion of the dissertation work by perturbing the conditions of several patients pharmacologically, and attempting to quantify the resulting changes using the model. Mechanical alterations in physiology through the use of vasodilators were applied to the patient "process" as the perturbation.

Vasodilators are commonly used clinically as "afterload reducing" agents, and include the drugs sodium nitroprusside, hydralazine, and the class known as angiotensin converting enzyme (ACE) inhibitors. Hence, model validation required clinical measurements of a patient both before and after the intervention. With respect to vasodilation, the effects were defined as a generalized decrease in peripheral resistance due to increased arteriolar dilatation, as well as an increase in peripheral capacitance. As will be shown later in this thesis, parameter estimation may be used to detect the alteration in peripheral resistance as a decrease in the value of the corresponding parameter.

1.3.3 Goal of the Study

Many additional applications other than system identification exist for a flexible yet comprehensive cardiovascular system model. Until now, no single model existed with the flexibility to address all of the various types of problems and applications listed above. Many of the various numerical models mentioned above decompose the circulation into lumped parameter approximations which have significant shortcomings in that specific geometric and anatomical detail is omitted. Such detail is necessary when considering the optimal placement of a CAD, for instance. Other models used previously also are deficient in that they consider only the circulation local to the device, and neglect the complex interaction between the device and the circulatory system as a whole. Hence, the various possible applications provided an excellent opportunity for the development of a more complete model. To summarize, a robust, comprehensive numerical model of the cardiovascular system was constructed to apply parameter estimation techniques on an individual patent's arterial pulse data. This constitutes merely the first step in the development of an intelligent diagnostic and treatment planning tool; completion of this thesis will open up further opportunities to strengthen the cardiovascular model, and to apply it to other problems in clinical and experimental medicine. These additional applications and the future directions for the model will be discussed in further detail in Chapter 6.

1.4 Thesis Organization

The structure of this thesis divides the work into two main parts. First, a description of the numerical model theory is given, including all of the relevant mathematical relationships and structural organization of the numerical code. This is followed by the definition of the standard case (composed of data representing the "normal" individual, taken from literature) and validation of the standard case by comparison of model results also with literature. This portion alone may be thought of as a separate work, since the

model is made adaptable enough to be applied to problems other than measurement of hemodynamic parameters which was briefly mentioned above. The second part of the thesis investigates the dependence of the model output on its specified parameters, and also gives a description of the parameter estimation scheme that is the major original application of the developed model. This is followed by a test of the parameter estimation technique against the data obtained at Brigham and Women's Hospital on both heart failure patients and normal individuals, and analysis of results.

Chapter 2

The Numerical Model of the Cardiovascular System

2.1 Cardiovascular Modeling

In order to accomplish the goals outlined in the introduction, it is necessary to construct a model of the cardiovascular system to allow quantitative control over the input parameters that define a particular patient. An animal model would not be appropriate, since one cannot have complete control of the physiology, thus making it difficult to observe changes in system behavior as a function of changes in the parameters. Additionally, there is the difficulty in obtaining accurate measurements of those parameters, which is a partial goal that this thesis attempts to address. Mechanical models give many more degrees of freedom in allowing physical properties to be changed at will, but a computer model is perhaps the most flexible of all possible model systems, since the physical characteristics can be altered by simply changing the number contained an input file.

It is therefore worthwhile to overview the current status of numerical cardiovascular modeling, and to point out which models in particular influenced the development of the model outlined in this chapter. Although the theory presented in this thesis is taken from many separate sources, this in no way implies that the model is merely a copy of other numerical cardiovascular simulators. Although many of the features are identical to those found in others, a great many innovations and improvements were made on existing models to capture as much of the true physiological behavior of the cardiovascular system as possible. There are advantages to constructing a model as detailed as the one presented in this chapter, as will become clear later.

One of the most useful, simple models of the cardiovascular system available is an educational tool known as CVSIM (CardioVascular SIMulator), developed by Sah and Davis and implemented on the Athena computer network at M.I.T. (Davis, 1991; Sah, 1985). The model consists of a lumped parameter approximation of the major components of the circulation, namely the systemic arteries, systemic veins, pulmonary

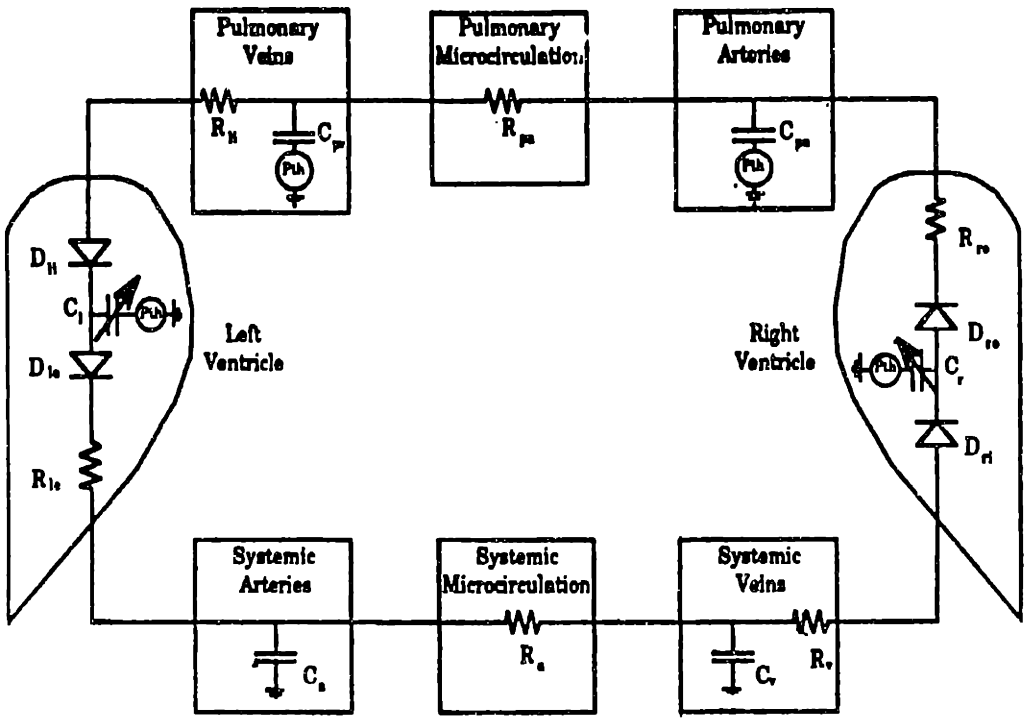

Figure 2.1. Schematic of the lumped parameter model of the cardiovascular system, CVSIM. From Davis, 1991.

arteries, pulmonary veins, and the left and right ventricles (Figure 2.1). Each component is specified by a representative resistor-capacitor windkessel approximation. The electrical analog equations used to describe the lumped parameter network are solved numerically using 4-step Runge-Kutta. The model is advantageous in that the overall behavior of the circulation can be described for a small computational cost. Its implementation of windows system user interfaces, which allow real time manipulation of hemodynamic parameters, gives the user the sense of how each parameter contributes to modulation of pressures and flows throughout the circulation. Additionally, a simple baroreflex control loop is included so that transient effects can also be examined. The simplicity of the equations that describe the system allow for real-time computation, allowing the user to adjust system parameters at will to observe the effect of the baroreceptor reflex loop.

In terms of describing the effect of wave transmission and propagation in the arterial system, however, CVSIM has serious shortcomings. The arterial pressure pulse produced by the simulation is qualitatively much different than the actual pulse, and the effects of wave propagation, reflection, and augmentation due to changes in arterial properties as a function of distance from the heart are unaccounted for. Nonetheless, CVSIM provides the groundwork for the lumped parameter approximation of the venous and pulmonary circulations, as well as the baroreceptor reflex, that is included in this thesis. However, in order to capture the behavior of these phenomena, a more complex and accurate model is required. This requires a better understanding of the fluid mechanics of a network of elastic tubes than a simple lumped parameter model can provide.

The groundwork for modeling flow in a straight elastic segment was laid out in extensive detail by faculty and students in the Fluid Mechanics Laboratory at M.I.T. during the 1970's. One of the earliest models developed in the Fluid Mechanics Laboratory was created in 1972 by Raines in his doctoral thesis, which attempted to characterize arteriosclerosis in the lower limbs by analysis of the arterial pressure pulse (Raines, 1972). This was later followed by the work of Kamm, who developed a model of the behavior of a single collapsible tube using one-dimensional momentum and continuity (Kamm, 1977). This was subsequently applied to study the effects of external pressures on the tube as a model for the disturbed venous flow conditions associated with deep vein thrombosis. A paper was later published by Kimmel, Kamm, and Shapiro, in which a numerical simulation of flow in pulmonary airways was performed (Kimmel et al., 1988). In this model, the equations of momentum and continuity, coupled with a

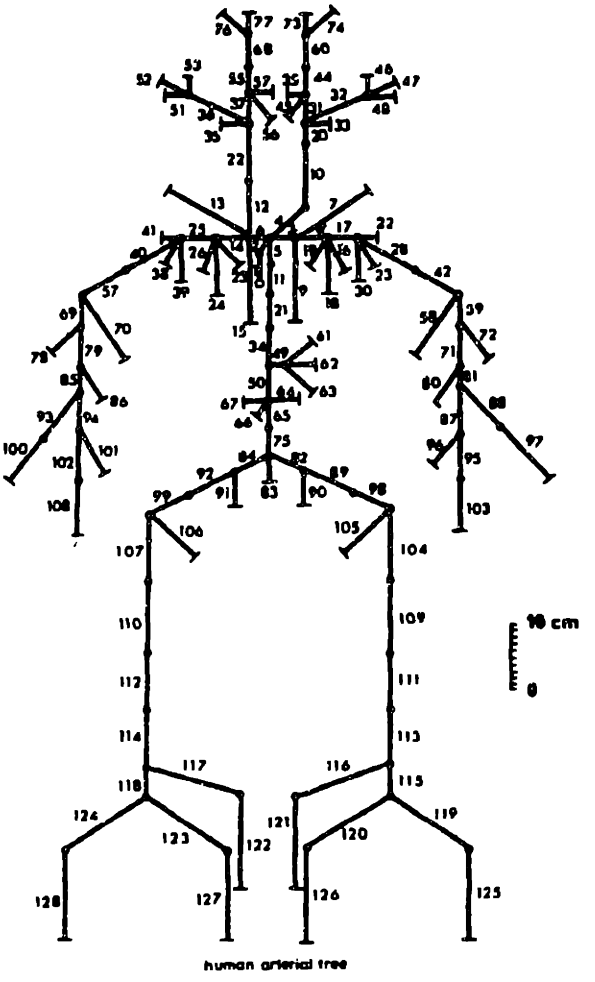

Figure 2.2. Schematic of distributed arterial model from Avolio et al., 1980.

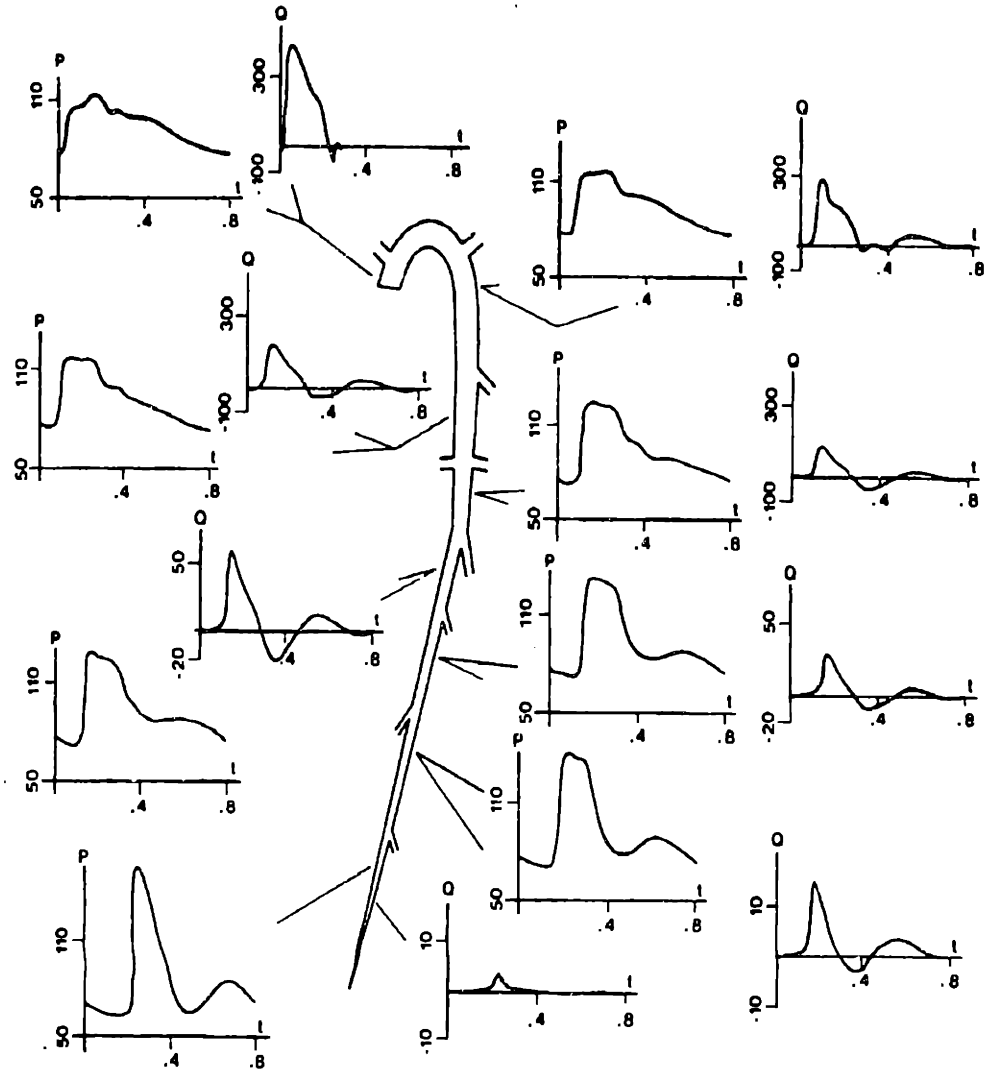

Figure 2.3. Output of the arterial distributed model of Stettler et al., 1981.

tube law, were solved using finite difference. The model was used to investigate the effects of nonuniformities in the stiffness distribution of the tube on flow behavior.

One of the earliest lumped parameter models of the circulation was constructed by Westerhof (Westerhof et al., 1969). Their model consisted of an electrical analog model composed of numerous elements containing LRC circuits. The model reproduced the expected pressure and velocity tracings at specific anatomical locations throughout the body, as well as the effect of wave reflections, which the simpler RC model CVSIM is unable to produce. Additionally, Westerhof's model was used to investigate the effect of changing peripheral resistance on input impedance. Avolio later described a numerical version of Westerhof's model (Avolio, 1980), in which the equations describing its 128 lumped parameter elements were solved computationally (Figure 2.2). Avolio obtained similar results to those of Westerhof, and further validated the computational model by comparing the calculated input impedances at various locations in the circulatory system to literature.

Many of the equations used to describe the model constructed in this thesis were influenced heavily by the work of Stettler and Niederer, who developed a distributed model of the arterial system (Stettler et al., 1981). Unlike the earlier models by Avolio and Westerhof, however, Stettler solved the fluid mechanics equations for one-dimensional momentum and continuity using the method of characteristics. Stettler also included in his model the effects of wall viscoelasticity and periodic wallshear. Sample calculated arterial waves from Stettler's model are shown in Figure 2.3. This model was particularly useful in developing the simulation outlined in this thesis, although differences exist. For instance, Stettler solves for the equations of motion using the method of characteristics and ignores the losses at bifurcations. In our model, the equations of motion are solved using finite difference, and the bifurcations losses are included. Additionally, our model makes use of a sophisticated venticular model which contributes to a more acccurate representation of the physiological behavior of the cardiovascular system.

Additional models have been constructed to investigate the interrelationship between hemodynamics and cardiovascular control. This has been useful in studying the response of the human body to the extremes of military flight and space travel. A model constructed by White consisted of a rather sophisticated lumped parameter model of the circulation, where many individual major organ systems were modeled as separate windkessels (White et al., 1983). The model was connected to a control system of cardiovascular control in order to asses the effects of changes in gravity due to flight or space travel. estimation of the influential parameters of cardiovascular control using

system identification techniques is an active field of study at present, where the control system can be represented as a closed loop system composed of black box transfer functions containing the governing parameters.

The problem of developing a numerical model of the circulation has been approached by many different paths, and thus the theory surrounding blood flow in elastic arteries is well established. However, none of the models are suited to address the issues of parameter estimation, in that each of the models previously developed address specific aspects of the circulation but fail to adequately model the global behavior. Since the behavior of an individual's circulatory system is strongly dependent on the interaction between these many diverse aspects, it is necessary to be able to model this interaction to a reasonable degree. The model presented here addresses this need, and as such is capable of handling many other existing problems and issues in cardiovascular physiology.

2.2 Model Theory

The cardiovascular model is a multi-component system, and therefore the remainder of this chapter is devoted to describing each of these components individually. The model as it stands presently can be viewed as a "tinker-toy" set consisting of the basic mechanical elements of the circulation, which can be organized into any conceivable arterial network, human or otherwise, without modification to the actual code. The input files are made flexible and global enough to include all of the information necessary to specify a particular system, and subsequently allow for easy alteration of its contents. We begin first by describing the theory of flow in elastic tubes, and how these tubes may be linked to form an arterial network. Considerable time is also spent describing the boundary conditions for the network, as well as lumped parameter modeling of extra-arterial vascular compartments and baroreflex control. Selection of model parameters, and general model validation, is covered in Chapter 3.

2.2.1 Model Assumptions

Before describing the equations used to construct the numerical model, it is useful to identify the primary modeling assumptions. The following list of assumptions are similar to those made by Stettler (Stettler et al., 1981) in the construction of their distributed model:

- Blood is an incompressible, Newtonian fluid.
- Blood flow in the aortic tree is one-dimensional (justified by the unidirectional, primarily axial nature of blood flow in arteries (Pedley, 1980).

- The walls are linearly elastic.
- Viscous friction can be approximated by considering the periodic behavior of wall shear, when appropriate.
- Curvature is ignored. The segments are assumed to be linearly tapered with respect to the cross-sectional area between bifurcation regions, and the angle of departure of a daughter branch from the main branch and the additional losses associated with the branched flow are taken into account.
- Leakage occurs along artery length. This leakage is a function of transmural pressure, and represents flow through small side branches that are either too small or too numerous to be included as individual artery segments.

The application of the above assumptions, in conjunction with the sound formulation of the equations of motion and other relationships that describe the constitutive behavior of the circulation, make it possible to construct a finite-difference numerical model of the circulatory system. This model will encompass the major arteries down to the second or third generation, and will provide an effective means of monitoring the circulatory system as a function of both time and anatomical position, while the system is perturbed by numerical systems representing any of a number of medical devices, or physiologic or pathologic stresses. Using the same modeling procedures, one could likewise model the major veins and vessels of the pulmonary circulation. However, because we are primarily interested in alterations in the behavior of the arterial system, we are able to neglect much of this finer detail.

2.2.2 Straight Segments

We consider in this model only one-dimensional flow, since we are interested in the mean values of pressure and flow at specific locations in the arteries, and also since higher dimensional flow problems are at present too computationally expensive to be of practical use. Hence, we begin by considering the control volume shown in Figure 2.4. The one dimensional flow in an elastic artery can be described using the basic equations for momentum and continuity:

$$\frac{\partial u}{\partial t} + \frac{\partial}{\partial x}\left(\frac{u^2}{2} + \frac{P}{\rho}\right) + F = 0 \tag{2.2.1}$$

$$\frac{\partial A}{\partial t} + \frac{\partial}{\partial x}(uA) + \Psi = 0 \tag{2.2.2}$$

where u and P are the average velocity and pressure, and A is the cross-sectional area at any axial location within an element. The leakage term Ψ in the continuity expression

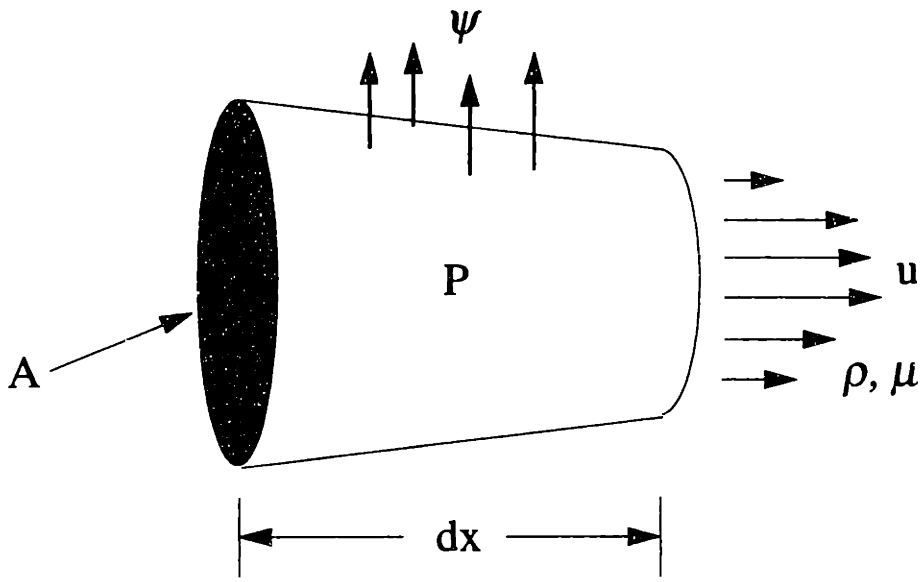

Figure 2.4. Finite segment of an elastic element.

represents the flow of blood through side branches that are too small to be represented as discrete branches. This term can be approximated as a linear resistive term, where the driving force for flow is the pressure drop between the local arterial internal pressure and the uniform venous pressure P_v.

$$\Psi(P,z) = \Phi(z)(P - P_v) \tag{2.2.3}$$

The friction term F in the momentum equation may be appropriately modeled given that the flow is steady or quasi-steady. Flow in the arterial system is periodic with significant flow reversals, and thus the Poiseuille approximation is inaccurate. Other, more appropriate replationships will be described in more detail in the later section covering damping mechanisms (Section 2.2.4).

The equations of motion (2.2.1) and (2.2.2) can be reduced to matrix form:

$$\frac{\partial}{\partial t}[A] + \frac{\partial}{\partial x}[B] + [C] = 0 \tag{2.2.4}$$

where

$$[A] = \begin{bmatrix} u \\ A \end{bmatrix}, \quad [B] = \begin{bmatrix} u^2/2 + P/\rho \\ uA \end{bmatrix}, \text{ and } [C] = \begin{bmatrix} F \\ \Psi \end{bmatrix}$$

(2.2.5), (2.2.6), (2.2.7)

At this point the pressure-area relation or "tube law" may be incorporated to provide a third independent equation to equations (2.2.1) and (2.2.2). From a simple definition of wave speed, one may obtain a constitutive relationship for arterial wall behavior. This begins with the relationship:

$$c^2(P,z) = A(P,z) / \left(\rho \frac{\partial A}{\partial (P - P_e)} \right) \tag{2.2.8}$$

where P_e is the pressure acting external to the artery. It is important to define such a pressure when considering intrathoracic arteries or vessels subjected to external compression.

An estimate of the wave speed c in an artery segment can be obtained using the following expression derived by Stettler

$$c(P,z) = (\chi_o + B(P - P_e)) \cdot g(z) \tag{2.2.9}$$

where the constants B and χ_0, and the function $g(z)$ are obtained from experimental measurements, to the extent that data are available (Stettler et al., 1981). Integration of equation (2.2.8) yields the tube law:

$$A(P,z) = A_o(z) \cdot \exp\left[\frac{(P - P_e) - P_o}{c(P_o,z) \cdot \rho \cdot c(P,z)}\right] \qquad (2.2.10)$$

where $A(P,z)$ represents the cross sectional area of the vessel at a position z and reference transmural pressure P - P_e. This expression is used, but in a form modified to account for wall viscoelasticity as described in Section 2.2.4.

Thus, three equations have been defined that give rise to three unknowns, which we refer to as the *state variables*: pressure P, velocity u, and cross-sectional area A. Due to the non-linearity of the governing equations, an analytical solution cannot be obtained. Thus, a numerical scheme to solve the series of partial differential equations must be implemented. The numerical two-step scheme for solving the equations of motion on a one-dimensional grid is described next.

2.2.3 Numerical Solution: MacCormack Scheme

The equations of motion are hyperbolic wave equations that are best solved using an explicit method, such as forward Euler in time and space. A more sophisticated finite difference scheme is the MacCormack two-step predictor corrector method, which is similar to the Lax Wendroff method. This particular method was used successfully by Kimmel et. al in their model of pulmonary flow (Kimmel et al., 1988), in which equations of motion almost identical to the ones we have outlined above were solved for. Thus, we employ the MacCormack scheme to calculate the internal points in any given artery segment (or *element*) for our model as well.

The set of hyperbolic, partial differential equations (2.2.4) for the elements are solved using an adaptation of the MacCormack two step predictor-corrector method. The method is commonly used for solving problems involving gas dynamics, although it also lends itself to the differential equations in the form given. Computations of the one-dimensional flow of air in collapsible tubes, representing the respiratory system, were performed in our lab using similar numerical techniques (Shin, 1992; Wolf, 1990). A single elastic tube segment may be discretized into n nodes, separated by a distance Δx, where the total segment length is equal to $(n\text{-}1)\Delta x$. A finite difference scheme requires the specification at each timestep of the state variables at the two boundary nodes (referred to here as the *distal*, or downstream, boundary end node and the *proximal*, or upstream, boundary end node). The boundary may be updated by a number of methods, depending on the type of boundary. The internal points, however, are solved for using the MacCormack scheme.

The form of the numerical method is given below in two parts; the predictor step:

$$[A]_j^{\overline{n+1}} = [A]_j^n - \frac{\Delta t}{\Delta x}\left\{[B]_{j+1}^n - [B]_j^n\right\} - \Delta t[C]_j^n \tag{2.2.11}$$

and the corrector step:

$$[A]_j^{n+1} = \frac{1}{2}\left\{[A]_j^n + [A]_j^{\overline{n+1}} - \frac{\Delta t}{\Delta x}\left([B]_j^{\overline{n+1}} - [B]_{j-1}^{\overline{n+1}}\right) - \Delta t[C]_j^{\overline{n+1}}\right\} \tag{2.2.12}$$

where Δx and Δt are the chosen spatial and temporal stepsizes, respectively, and j is the number of the node being solved for at the new timestep n+1. The over bars represent the intermediate timestep from the corrector step. For numerical stability, the Courant stability criterion:

$$\frac{\Delta x}{\Delta t} \geq |u| + c \tag{2.2.13}$$

must be applied. As the algorithm marches forward in time, the timestep Δt is updated by determining its smallest value for the entire system during the previous position in time, using equation (2.2.13) set to equality. The above numerical calculation scheme is stable for all values of Δt smaller than that calculated from the Courant stability criterion. The simulation may be run such that the ratio of the timestep to the criterion (also called the *cfl number*) can be less than unity. This has important implications towards the stability of the calculation, which will be discussed later.

2.2.4 Damping Mechanisms in the Arterial Tree

Sufficient evidence has been presented in previous studies to support the need for damping mechanisms that have not been included in the model theory to this point. The equations of motion presented above assume a purely elastic constitutive relationship for the artery walls, and one may derive the expressions for wall shear stress based on the Poiseuille model for *steady* flow in tubes. However, it has been clearly shown that for values of the Womersley number $\alpha > 2$, the Poiseuille approximation significantly underestimates the shear stress. While the Poiseuille approximation for the frictional losses in the elastic tube is appropriate for tubes of relatively small diameter, the actual frictional losses may be reduced in the larger arteries during oscillatory flow due to the inability of the viscous boundary layer to fully propagate from the wall to the center. In pulsatile flow through a large artery, the transient inertial effects dominate over the viscous forces. Thus, it is necessary to take into consideration the ratio between the transient inertial and viscous terms, which may be expressed by the following relationship:

$$\alpha = \frac{D}{2}\sqrt{\frac{\omega}{\nu}} \tag{2.2.14}$$

where D is the tube diameter, and ω is the characteristic frequency (the frequency of the heart beat). In the human aorta, α generally has a value of about 20.

For low α, the resistance to an oscillating flow in a tube approaches the Poiseuille resistance. However, for high α, the ratio of the Womersley profile resistance to the Poiseuille resistance approaches $\alpha\sqrt{2}/8$. Thus, the apparent resistance to periodic flow in the large arteries is less than that for steady flow in tubes of the same size and mean velocities. Such a result is consistent with the observation that viscous forces dominate only in a small annular boundary layer adjacent to the artery wall.

Thus, the need arises to include time-dependent wall shear in order to obtain accurate waveforms in the arterial system. Additionally, wall viscoelasticity associated with periodic fluid flow in tubes has also been shown to be of major importance in the reduction of shocks in the arterial tree (Holenstein et al., 1980; Holenstein et al., 1983; Niederer, 1985) The theoretical details associated with each are outlined in the next two subsections.

2.2.4.a Influence of Blood Viscosity

As previously mentioned, for large values of the Womersley number α the assumption of fully-developed viscous flow is inappropriate. As the frequency of unsteadiness increases, the magnitude of the wall shear stress increases and there develops a significant phase lag between the axial velocity and the friction force as the time for the fluid deceleration to diffuse from the center to the wall approaches the characteristic time of the unsteadiness. A more realistic approximation of the frictional losses in periodic flow was developed by Zeilke (Zeilke, 1968), and is outlined as follows. Zeilke first begins with the one-dimensional momentum equation in cylindrical coordinates:

$$\frac{\partial^2 u}{\partial r^2} + \frac{1}{r}\frac{\partial u}{\partial r} - \frac{1}{u}\frac{\partial u}{\partial t} = \frac{1}{u\rho}\frac{\partial P}{\partial x} \tag{2.2.15}$$

An assumption for this equation must be made that the convective acceleration term does not have a significant effect on the axial velocity profile. By taking the Laplace transform of the momentum equation, we can solve for the velocity u in the Laplace domain, with transformed variables denoted by the tilda superscript:

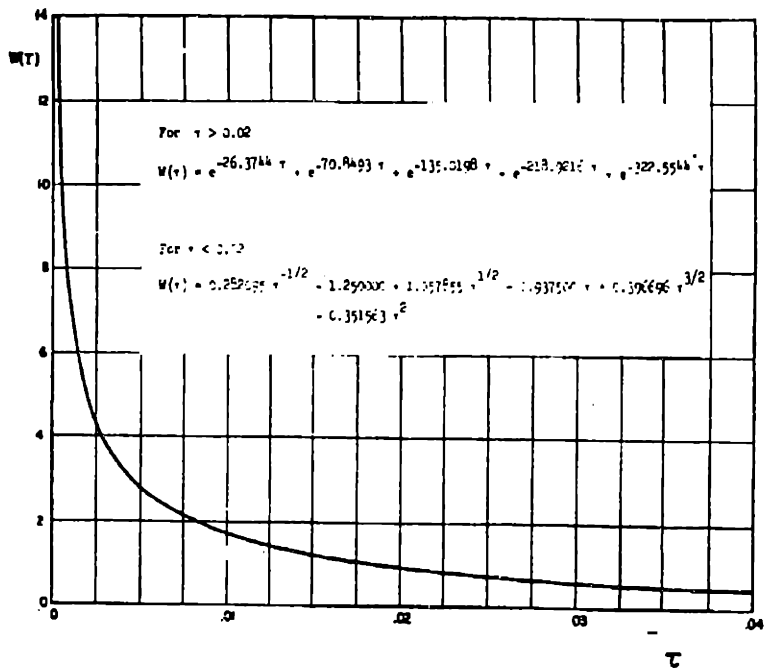

Figure 2.5. The weighting function W as a function of τ . From Zeilke, 1968.

$$\tilde{U}(r,s)=\frac{\tilde{P}_z}{\rho s}\left[\frac{J_o\left(i\sqrt{\frac{s\rho}{\mu}}r\right)}{J_o\left(i\sqrt{\frac{s\rho}{\mu}}R\right)}-1\right] \tag{2.2.16}$$

where the boundary conditions $v = 0$ at $r = R$ (tube radius), and $dU/dt = 0$ at $r = 0$ have been applied. In equation (2.2.16) J_0 denotes the Bessel functions of the first kind and zero order. From the velocity distribution, one may solve for the mean velocity:

$$\tilde{u}(s)=\frac{\tilde{P}_z}{s}\left[\frac{2J_1\left(i\sqrt{\frac{s\rho}{\mu}}R\right)}{i\sqrt{\frac{s}{u}}J_0\left(i\sqrt{\frac{s\rho}{\mu}}R\right)}-1\right] \tag{2.2.17}$$

where J_1 are the Bessel functions of the first kind and first order. Using the definition of shear stress at the wall

$$\tilde{T}(s)_{wall}=-\mu\left.\frac{\partial\tilde{U}}{\partial r}\right|_{r=R} \tag{2.2.18}$$

with the symbol $\tilde{T}$ representing shear in the Laplace domain, an expression for the wall shear using equation (2.2.16) may be written as

$$\frac{\tilde{T}}{s\tilde{u}}=\frac{R\rho}{i\sqrt{\frac{s\rho}{\mu}}R\dfrac{J_o\left(i\sqrt{\frac{s\rho}{\mu}}R\right)}{J_1\left(i\sqrt{\frac{s\rho}{\mu}}R\right)}-2}=\tilde{W}(s). \tag{2.2.19}$$

The inverse Laplace transform of the shear stress yields the relationship in the form of a convolution integral

$$T(t)=\int_0^\infty \dot{u}(t')W(t-t')dt' \tag{2.2.20}$$

where t' is the time used to integrate the history of the acceleration backwards from the present time t. This shear term can be incorporated with the Poiseuille approximation for steady flow to yield the following expression for the viscous loss term:

$$F=\frac{2}{\rho R}\left(\frac{4\mu}{R}u(t)+\frac{2\mu}{R}\int_0^\infty\frac{\partial u(t')}{\partial t}W(t-t')dt'\right) \tag{2.2.21}$$

where $W(t)$ has been solved for by Zeilke from the inverse Laplace transform of equation (2.2.19), and is represented by two separate functions:

$$W(t) = e^{-26.3744\frac{\mu t}{\rho R^2}} + e^{-70.8493\frac{\mu t}{\rho R^2}} + e^{-135.0198\frac{\mu t}{\rho R^2}} + e^{-218.9216\frac{\mu t}{\rho R^2}} + e^{-322.5544\frac{\mu t}{\rho R^2}} \qquad \frac{\mu t}{\rho R^2} > 0.02 \tag{2.2.22}$$

$$W(t) = 0.282095\left(\frac{\mu t}{\rho R^2}\right)^{-1/2} - 1.250000 + 1.057855\left(\frac{\mu t}{\rho R^2}\right)^{1/2} + 0.937500\frac{\mu t}{\rho R^2} + 0.396696\left(\frac{\mu t}{\rho R^2}\right)^{3/2} - 0.351563\left(\frac{\mu t}{\rho R^2}\right)^{2} \qquad \frac{\mu t}{\rho R^2} \le 0.02 \tag{2.2.23}$$

Graphically the weighting function $W(t)$ is shown in Figure 2.5, where the x-axis is expressed in terms of the dimensionless time

$$\tau = \frac{\mu t}{\rho R^2}. \tag{2.2.24}$$

The expression (2.2.21) may be incorporated into the momentum equation (2.2.1) by replacing the friction term F term, thus yielding the final form of the momentum equation:

$$\frac{\partial u}{\partial t} + \frac{\partial}{\partial x}\left(\frac{u^2}{2} + \frac{P}{\rho}\right) + \frac{2\pi\mu}{\rho A}\left(4u(t) + 2\int_0^\infty \dot{u}(t')W(t-t')dt'\right) = 0 \tag{2.2.25}$$

which includes both a Poiseuille friction term and a history dependent convolution term. Note that as the acceleration term in the convolution integral approaches zero, the friction term approaches the limit of steady Poiseuille friction. This frequency dependence on friction has been incorporated into the cardiovascular models developed by Niederer and his colleagues.

The integral term in expression (2.2.21) may be evaluated using the following summation as an approximation:

$$\sum_{j=1,3,\ldots}^{k-1}(u_{i,j+1} - u_{i,j-1})W((k-j)\Delta t) = \sum_{j=1,3,\ldots}^{k-1}(u_{i,k-j+1} - u_{i,k-j-1})W(j\Delta t) \tag{2.2.26}$$

This summation requires the storage of local velocity for every nodal position within a window of 0.5 seconds backwards in time, a number obtained from the observation that

increasing the window beyond this point had no appreciable effect on the quality of the generated waveforms. However, given that the timestep Δt calculated from the Courant condition is on the order of 0.001 seconds, this requires the storage and subsequent integration over 500 timesteps for *each* individual node. Such a repeated operation is extremely computationally expensive. To reduce the computational time, a strategy is employed in which the velocities at either every other or every third time step is used. This reduces both the memory required, and the number of operations required to evaluate the summation described by equation (2.2.26).

2.2.4.b Influence of Wall Viscoelasticity

Although the arterial walls have been modeled as purely elastic up to this point, we have already stated that the viscoelastic damping properties of arteries are important and cannot be neglected in order to obtain accurate physiological results. Furthermore, in our experience the use of the constitutive wall expression (2.2.10) has led to difficulties numerically, in that high frequency noise is generated by the present model in the absence of more robust damping mechanisms such as wall viscoelasticity. Thus, it is justified to include viscoelastic damping into the wall behavior, again using the analysis presented by Holenstein et al.

From linear viscoelastic theory, a relationship between stress and strain may be written as a convolution integral and rewritten in order to take into account the quasistatic nonlinearities, resulting in the expression for area A as a function of pressure p and time t:

$$A(t) = A^e(P(t)) + \int_0^\infty \dot{J}(t')A^e(P(t-t'))dt' \tag{2.2.27}$$

where again t' is the time used to integrate the history backwards from the present time t, $J(t)$ represents the creep function for the material of interest (in this case the artery wall) and A^e is the instantaneous elastic response, or the cross-sectional area of an artery immediately after a step function in pressure is applied, as a function of that pressure. As with the transient wall shear, the wall viscoelasticity is dependent on the wall area history. Holenstein et al. uses the creep function derived by Fung (Fung, 1972) given in the form

$$J(t) = 1 + a\log\frac{\tau_2}{\tau_1} + a\left(E_1\left(\frac{t}{\tau_1}\right) - E_1\left(\frac{t}{\tau_2}\right)\right) \tag{2.2.28}$$

where

$$E_1(z) = \int_z^\infty \frac{e^{-t}}{t}dt \,. \tag{2.2.29}$$

The three parameters in equation (2.2.28) are selected as

$$a = 0.3$$
$$\tau_1 = 0.00081$$
$$\tau_2 = 0.41$$

and are obtained from experimental data (Niederer, 1985). This results in the time derivative of the creep function used in the convolution, given by

$$\dot{J}(t) = a\frac{e^{-t/\tau_2} - e^{-t/\tau_1}}{t} \quad . \tag{2.2.30}$$

In order to solve for the convolution integral, an expression has to be found for the instantaneous elastic response. Holenstein derives the following expression:

$$A^e(p) = A(p_o) \times \exp\frac{|E(\omega^*)| \cdot (p - p_o)}{E(0) \cdot \cos\frac{\phi(\omega^*)}{2} \rho c_{ph}(p_o, \omega^*) \cdot c_{ph}(p, \omega^*)} \tag{2.2.31}$$

where ω^* is a representative frequency, ϕ is the phase velocity, p_o is a reference pressure, and the modulus of elasticity E is defined as

$$E(\omega) = |E(\omega)| e^{i\phi(\omega)} \tag{2.2.32}$$

which is dependent on frequency. The modulus of elasticity, however, is weakly dependent on frequencies greater than 50 Hz. Anliker has demonstrated that waves are nondispersive and between 20 and 200 Hz (Anliker et al., 1968). Thus, the frequency dependence may be neglected and the phase velocity approximated by the measured wave speeds. The expression for instantaneous elastic response thus reduces to the following relation:

$$A^e = A_o^e(p_o, z) \cdot \exp\left(\frac{p - p_o}{\rho \cdot c(p_o, z) \cdot c(p, z)}\right) \tag{2.2.33}$$

which is nearly identical to the original tube law, with the exception that the reference response A^e_o represents the instantaneous elastic response to a reference pressure. To calculate the reference response, the steady state reference cross-sectional area may be used. If one considers the convolution expression (2.2.28) in *steady state* at the reference pressure where measurements can be obtained, then the instantaneous elastic response within the integral becomes a constant. Thus, the expression reduces to:

$$A_o(z) = A_o^e(p_o, z) \cdot \left(1 + \int_0^\infty \dot{J}(\tau) d\tau\right) = A_o^e(p_o, z) \cdot 1.8681 \tag{2.2.34}$$

and the reference instantaneous elastic response may be solved for. The expression (2.2.27) in conjunction with expression (2.2.33) is the form of the tubelaw that is used in the numerical calculation to convert pressures at a given node to the corresponding area. The equation may also be solved for pressure as a function of area, giving the "inverse" tubelaw, which is required for certain calculations.

2.3 Boundary Conditions

Once the internal points within the arterial segments have been solved for, it is necessary to update the proximal and distal endnodes using a series of routines. As mentioned previously, the elemental segments are joined at bifurcations to form an arterial tree network. The network is bounded most proximally by a model of the left ventricle, while at the most distal nodes of the terminal elements, the boundary condition is provided by a windkessel approximation of the small artery vasculature, ending in arteriolar beds. We begin this section with a discussion of the most extensively used boundary condition, the bifurcation control volume.

2.3.1 Bifurcations

We have thus far described the behavior of individual arterial segments, but that is far from adequate for defining the whole circulation system, where flow is divided by bifurcations. Additionally, bifurcations act as a source of wave reflections in the actual physiological system, and as we shall demonstrate, are also present in the model. It is thus necessary to consider the coupling of several elements at a bifurcation region, which we define as a single tube branching into N-1 separate daughter tubes. Previous investigators have chosen to model the influence of bifurcations as division points for characteristic lines using the method of characteristics. However, such an analysis fails to take into account losses due to flow separation or to the generation of secondary flows. Thus, the equations used to describe the behavior of flow in this region were taken from the work of Wolf (Wolf, 1990), which described the behavior of air passing through a pulmonary bifurcation during inspiration, including dissipative effects. Since Wolf assumed the fluid medium to be incompressible, the same equations may be applied to describe the flow of blood as it passes from the parent branch to several daughter branches.

2.3.1.a Equations of Motion

The bifurcation is treated as a control volume, across which unsteady Bernoulli with an added term for dissipation can be applied from station 1 (the parent branch) to station

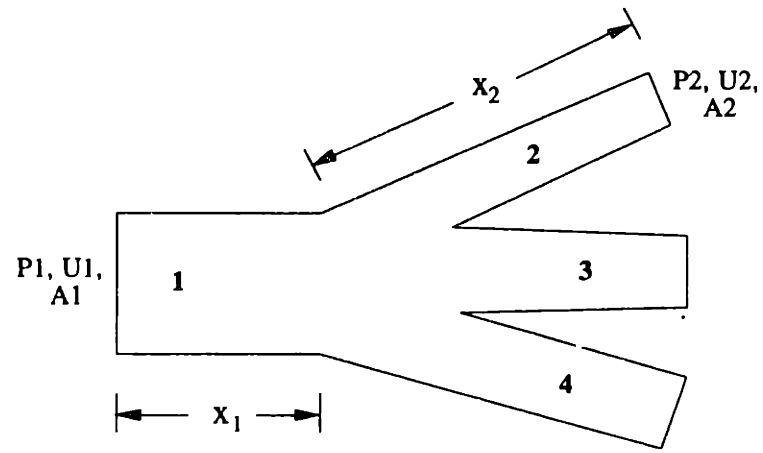

Figure 2.6. Bifurcation control volume for the case of N=4 N-1=3 daughter branches.

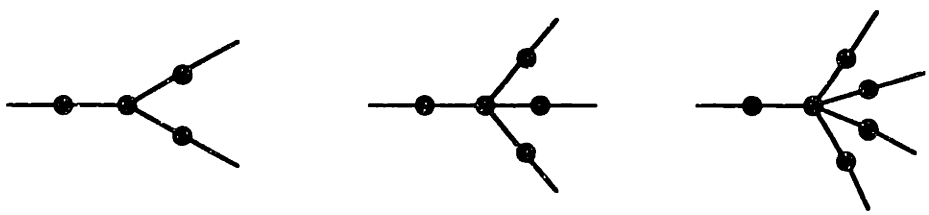

Figure 2.7. Branching patterns at the bifurcation with 2, 3, and 4 daughter branches.

2 (a daughter branch), and from station 1 to station n (another daughter branch), where there are N-1 total daughter branches:

$$\rho\frac{\partial U_1}{\partial t}x_1+\rho\frac{\partial U_2}{\partial t}x_2+P_2+\frac{1}{2}\rho U_2^2+F_{12}=P_1+\frac{1}{2}\rho U_1^2 \tag{2.3.1}$$

...

$$\rho\frac{\partial U_1}{\partial t}x_1+\rho\frac{\partial U_N}{\partial t}x_N+P_N+\frac{1}{2}\rho U_N^2+F_{1N}=P_1+\frac{1}{2}\rho U_1^2 \tag{2.3.2}$$

The bifurcation control volume is shown schematically in Figure 2.6, for the case of 4 total branches, or N-1=3 daughter branches, indexed n=2...N. Note that the energy equations are written as following streamlines from the parent branch at station 1, to the station n corresponding to each daughter branch. Additionally, the F terms represent the frictional losses occurring within the control volume along each streamline, and contain information about the angle of branching. The losses will be described in more detail shortly. A second necessary relation is the unsteady continuity equation for the control volume:

$$\frac{\partial A_1}{\partial t}x_1+\frac{\partial A_2}{\partial t}x_2+...+\frac{\partial A_N}{\partial t}x_N-U_1A_1+U_2A_2+..+U_NA_N=0 \tag{2.3.3}$$

The equations of motion can be coupled with momentum and continuity between the interface of an element with the bifurcation control volume, and the element's interior points. Thus, at each interface there are three unknown values: pressure, velocity, and cross-sectional area. An additional equation that is not shown is the pressure-area relationship including wall viscoelasticity, which is identical to the relationship (2.2.34). The equations are flexible enough to allow for any number of daughter branches, although beyond four is not required for the construction of the network model (Figure 2.7).

2.3.1.b Frictional Losses

Much of the groundwork for describing the frictional losses in bifurcation regions comes from the work of Pedley, who describes the ratio of the dissipation in a daughter tube downstream of a bifurcation to the dissipation due to Poiseuille flow in the same tube as

$$Z=\frac{C}{4\sqrt{2}}\left(\mathrm{Re}\frac{d}{L}\right)^{\frac{1}{2}} \tag{2.3.4}$$

where C = 1.85 (Pedley et al., 1970). Wolf incorporated the above expression for dissipation with a kinetic energy factor k to obtain the semi-empirical relationships for the rate of energy dissipation between the parent branch at station 1 and station n of the nth daughter branch (n=2...N):

$$\Phi_{1n} = (\frac{1}{2}\rho U_1^{\frac{1}{2}} A_n)\lambda_n U_n^{\frac{5}{2}} + \frac{1}{2}\rho U_n^3 A_n k_n \tag{2.3.5}$$

where λ is defined as the losses due to dissipation based on Pedley's expression shown in equation (2.3.4), and k_n is a kinetic energy factor. Expression (2.3.5) consists of a Pedley-type dissipation (the first term), summed with turbulent-like or separation losses (the second term). If we define the rate of energy loss in a pipe from Poiseuille flow as Φ, = $8\pi\mu U^2 L$ then using equation (2.3.5) we may write the following non-dimensional expression for the nth daughter branch:

$$\lambda_n = \frac{16C}{\sqrt{2}}\left[\frac{1}{\mathrm{Re}_1}\frac{D_1}{D_n}\frac{L_n}{D_n}\right]^{\frac{1}{2}} \tag{2.3.6}$$

where Re_1 is the Reynolds number of the parent branch. It is also necessary to define a second kinetic energy factor

$$f = \frac{1}{A}\int(\frac{u}{U})^3 dA \tag{2.3.7}$$

which represents the ratio of the kinetic energy flux for a parabolic velocity profile to that for a blunt velocity profile at the same volume flowrate. Equations (2.3.5) and (2.3.7) may be incorporated into the two equations for energy (2.3.1) and (2.3.2). The resulting energy equations have the following final form:

$$\rho\frac{\partial U_1}{\partial t}x_1 + \rho\frac{\partial U_2}{\partial t}x_2 + P_2 + \frac{1}{2}\rho\left(U_2^2 f_2 + U_2|U_2|k_2\right) - P_1 - \frac{1}{2}\rho U_1^2$$
$$+\frac{1}{2}\rho U_2|U_1U_2|^{\frac{1}{2}}\lambda_2 = 0 \tag{2.3.8}$$

...

$$\rho\frac{\partial U_1}{\partial t}x_1 + \rho\frac{\partial U_N}{\partial t}x_N + P_N + \frac{1}{2}\rho\left(U_N^2 f_N + U_N|U_N|k_N\right) - P_1 - \frac{1}{2}\rho U_1^2$$
$$+\frac{1}{2}\rho U_N|U_1U_N|^{\frac{1}{2}}\lambda_N = 0 \tag{2.3.9}$$

The absolute values of velocity are incorporated to preserve the directionality of the losses as the flow changes direction.

2.3.1.c Selection of Loss Parameters

The values of the kinetic energy and dissipation factors are dependent on the nature of flow at the bifurcation. For highly symmetric bifurcation regions with two daughter branches departing at small angles from each other, one would expect little flow separation and hence little energy dissipation. In this limit of unseparated flow, we allow the factors k to approach zero and f to approach 1, which is borne out by the definitions of the factors as defined by Wolf:

$$k = \left(1 - \frac{1}{K_c}\right)^2 \quad \text{and} \quad f = \left(\frac{1}{K_c}\right)^2 \qquad (2.3.10), (2.3.11)$$

The constant K_c is defined as the contraction coefficient, which represents the ratio between the area of a daughter branch normal to the flow leaving the parent branch, and the cross-sectional area of the branch itself. Hence, for smaller angles between adjacent daughter branches, K_c should approach 1. If we now consider a case in which a highly asymmetric daughter branch departs from the main conduit at a large angle, then the limit of highly separated flow is reached and K_c approaches zero, resulting in large kinetic energy coefficients. Furthermore, it is appropriate to neglect λ in the limit of high flow separation. For computational purposes, both K_c and λ are assumed constant through time for each specific bifurcation branch.

Data regarding the contraction coefficients as a function of branch angle are difficult to obtain for the arterial system. Intuitively, for instance, one would expect K_c at the renal bifurcation, where the renal arteries depart from the aorta at close to 90°, to lie at some intermediate value between 0 and 1. Likewise, K_c at the bifurcation of the brachial artery into the ulnar and radial arteries would be expected to be close to unity, where the angle of departure of the daughter branches is small. The actual specified values for the contraction coefficient will be discussed in further detail in Chapter 3, although it will be later shown in Chapter 4 that exact values are not required due to the small effect that bifurcation losses exert on the system as a whole.

2.3.1.d Solution Scheme for Bifurcation Regions

The equations of energy (2.3.1) and (2.3.2), and the unsteady form of continuity (2.3.3) are difficult to solve implicitly, due to the highly nonlinear nature of the equations and the large number of variables. One could expand all of the related equations, including momentum and continuity connecting the end nodes that comprise the bifurcation boundaries with the internal points, using Taylor series approximations. Such an expansion, however, would involve the inversion of a matrix iteratively to solve for

the boundary conditions at the new timestep, a costly process in terms of computational time. Instead, an alternative method of estimating the boundary values may be obtained by combining the energy and continuity relations with the previously described MacCormack predictor-corrector scheme to couple the state variables of the endnodes with the internal points.

Again refer to Figure 2.6. The two energy relationships are discretized using the explicit forward Euler's method into a predictor form which allows calculation of the predicted velocities at stations 2 through N. The predicted areas at the same stations are calculated using the predictor step for continuity from the MacCormack two-step scheme, applied between the endnode and its adjacent internal point. Predicted values of velocity and area at station 1 are also obtained by using the predictor step for momentum and downwind continuity, respectively, from the MacCormack scheme. The corresponding predictor step pressures are calculated using the inverse tube law $P=P(A,z)$ at all three stations. Corrected values for the velocity and area at stations 2 through N are then calculated using the respective MacCormack corrector form of momentum and upwind continuity. As in the predictor step, the inverse tube law is used to obtain the pressures at the new timestep for all stations. The velocity at station 1, however, is solved using a MacCormack corrector form of the energy equations (2.3.1) and (2.3.2), which may be written as follows for the path from station 1 to station n, n=2...N:

$$\frac{U_1^{j+1} - \tfrac{1}{2}(U_1 + \overline{U}_1)}{\tfrac{1}{2}\Delta t} x_1 + \frac{U_n^{j+1} - \tfrac{1}{2}(U_n + \overline{U}_n)}{\tfrac{1}{2}\Delta t} x_n + \overline{P}_n + \frac{1}{2}\rho \overline{U}_n^2 (f_n + k_n) + \overline{F}_{1n} = \overline{P}_1 + \frac{1}{2}\rho \overline{U}_1^2 \tag{2.3.12}$$

where the F term represents the dissipation as described by Pedley. The updated value for velocity at the new timestep at station 1 is evaluated from both energy equations and then averaged. The corrected area at station 1 is obtained from the following discretized form of continuity:

$$\frac{A_1^{j+1} - \tfrac{1}{2}(A_1 + \overline{A}_1)}{\tfrac{1}{2}\Delta t} x_1 + \frac{A_2^{j+1} - \tfrac{1}{2}(A_2 + \overline{A}_2)}{\tfrac{1}{2}\Delta t} x_2 + \ldots + \frac{A_N^{j+1} - \tfrac{1}{2}(A_N + \overline{A}_N)}{\tfrac{1}{2}\Delta t} x_N + \overline{U}_2\overline{A}_2 + \ldots + \overline{U}_N\overline{A}_N - \overline{U}_1\overline{A}_1 = 0 \tag{2.3.13}$$

which is also derived using the MacCormack scheme. This outlined scheme is implemented following calculation of the internal points, since the predictor-corrector requires explicit values of the adjacent, internal nodes. The driving force for the model is described next as a boundary condition for the most proximal endnode in the arterial model.

2.3.2 Ventricular Mechanics

In order to obtain a model that reacts correctly to changes in conditions which may alter the reflection of pressure waves from the periphery (and thus the load imposed at the left ventricle) the common approach of using a synthesized pressure or velocity wave at the root of the aorta to drive the model was not followed here. The changes in ventricular function as a result of alterations in the afterload profile can only be captured if a compliance-based model of the left ventricle is used, in which wall compliance as a function of time is specified. A similar model may be implemented for the right ventricle as well. Additionally, unidirectional valves to prevent backflow into the ventricles must be included in the model.

2.3.2.a The Left Ventricle

In the cardiovascular model the left ventricle acts as a boundary between the lumped parameter approximation of the pulmonary circulation and the more detailed, one-dimensional network model of the arterial tree. The ventricle may be approximated by a chamber with an entrance (mitral) and exit (aortic) valve, whose compliance changes as a function of time, thus driving flow. The ventricular wall elastance E varies as a function of time, and the ventricular volume V_{vent} is assumed to be a linear function of the ventricular pressure P_{vent}:

$$P_{vent} = E(t) \cdot \left(V_{vent} - V_{vent,o} \right) \tag{2.3.14}$$

where $V_{vent,o}$ is the zero-pressure filling volume. Suga and Sugawa have shown in canines that the left ventricular elastance curve is well-preserved when non-dimensionalized with respect to peak elastance and time to peak elastance (Figure 2.8). Hence, previous researchers have used equation (2.3.14) in conjunction with the estimated E versus time curve as a complete model for left ventricular mechanics. Although in subsection 2.3.2.b this model will be shown to be incorrect, and significant modifications will be made there, it is still illustrative to use this form of the model in developing the formalism of the approach. Additionally, here the discussion will be restricted to the mechanics of the left ventricle, while the right ventricle will be described in detail in Section 2.4 with the remainder of the lumped parameter model.

A single cycle of the left ventricle can be subdivided into four parts: 1) early systole, during which time the pressure in the left ventricle begins to rise as a result of increasing ventricular wall stiffness, which causes the mitral valve to shut and the ventricle to isovolumetrically increase its internal pressure to arterial levels; 2) the ejection phase of systole, when the ventricular pressure exceeds aortic pressure, causing the aortic valve to

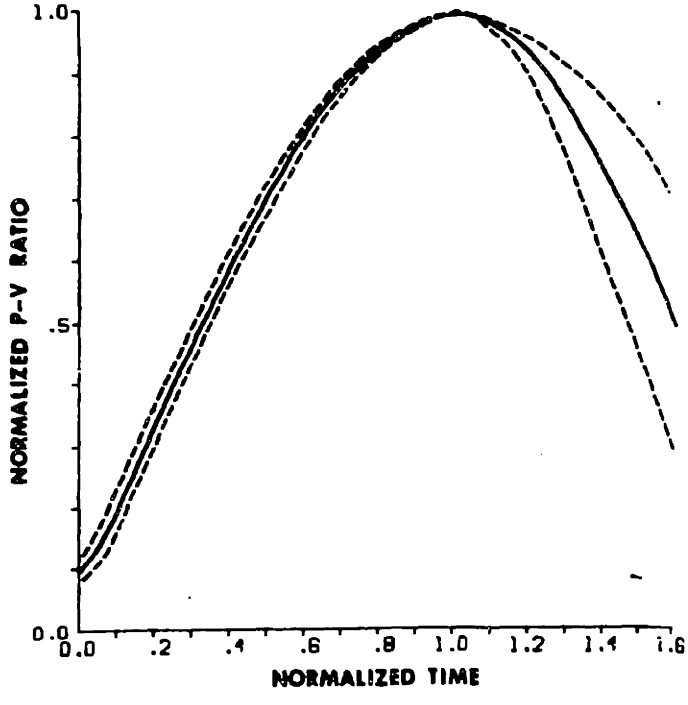

Figure 2.8. Normalized ventricular elastance (pressure-volume) curve, mean ±SD (two broken lines). From Suga and Sugawa, 1974.

open and the ventricle to drain; 3) flow reversal, where pressure in the left ventricle drops below aortic pressure, causing blood to accelerate backwards to close the aortic valves and fill the sinuses of valsalva; 4) diastole, during which the left ventricle fills through the mitral valve, with stasis of the aortic valves. Each of these identified phases represents a separate process of calculation. These phases will be described in terms of theory in chronological order, but is also summarized in Figure 2.9.

Phase 1 and 2: isovolumetric contraction and ejection:

At end diastole from the previous cycle, the ventricle is filled passively via the left atrium, which is neglected in this model. As the function $E(t)$ begins to increase with systole, the left ventricular pressure rises during the isovolumetric period when both the mitral and aortic valves are closed (phase 1). In equation (2.3.14) this is accomplished by holding the left ventricle volume terms constant, and solving for the new pressure values for each specified $E(t)$. Eventually, left ventricular pressure exceeds aortic root pressure, and the ventricle begins to empty. The equations needed to couple the left ventricular pressure to the first element boundary node during ventricular emptying (phase 2) are the one-dimensional equations of motion and the elastic tubelaw. These equations are solved in predictor-corrector fashion for the boundary node state variables U_1, P_1, and A_1 using upstream momentum and continuity and unsteady Bernoulli:

$$U_1^{n+1} = \frac{1}{2}\left(U_1^{\overline{n+1}} + U_1^n + \frac{\Delta t}{\rho a}\left(P_{lv}^{\overline{n+1}} - P_1^{\overline{n+1}} - \frac{1}{2}\rho U_1^{\overline{n+1}} \cdot U_1^{\overline{n+1}} \right) \right) \tag{2.3.15}$$

where a is a characteristic length equal to 3 times the radius of the aortic root. The predictor equation form (2.2.11) for momentum and continuity is applied to solve for predicted values of velocity and area; the inverse tubelaw is used to determine the predicted pressure. A corrector form of unsteady Bernoulli of the following form is then applied to determine the corrected velocity:

$$U_1^{n+1} = \frac{1}{2\rho s}\left[U_1^{\overline{n+1}} + U_1^n + dt\left(P_{vent}^{\overline{n+1}} - P_1^{\overline{n+1}} - \frac{\rho U_1^{\overline{n+1}} \cdot U_1^{\overline{n+1}}}{2} \right) \right] \tag{2.3.16}$$

The updated value for outflow U_1A_1 is then used to update ventricular volume:

$$U_1 A_1 = -\frac{dV_{vent}}{dt} \tag{2.3.17}$$

and V_{vent} is in turn used to calculate P_{vent} for the new timestep using equation (2.3.14). Calculation using these equations is continued until the left ventricular pressure falls

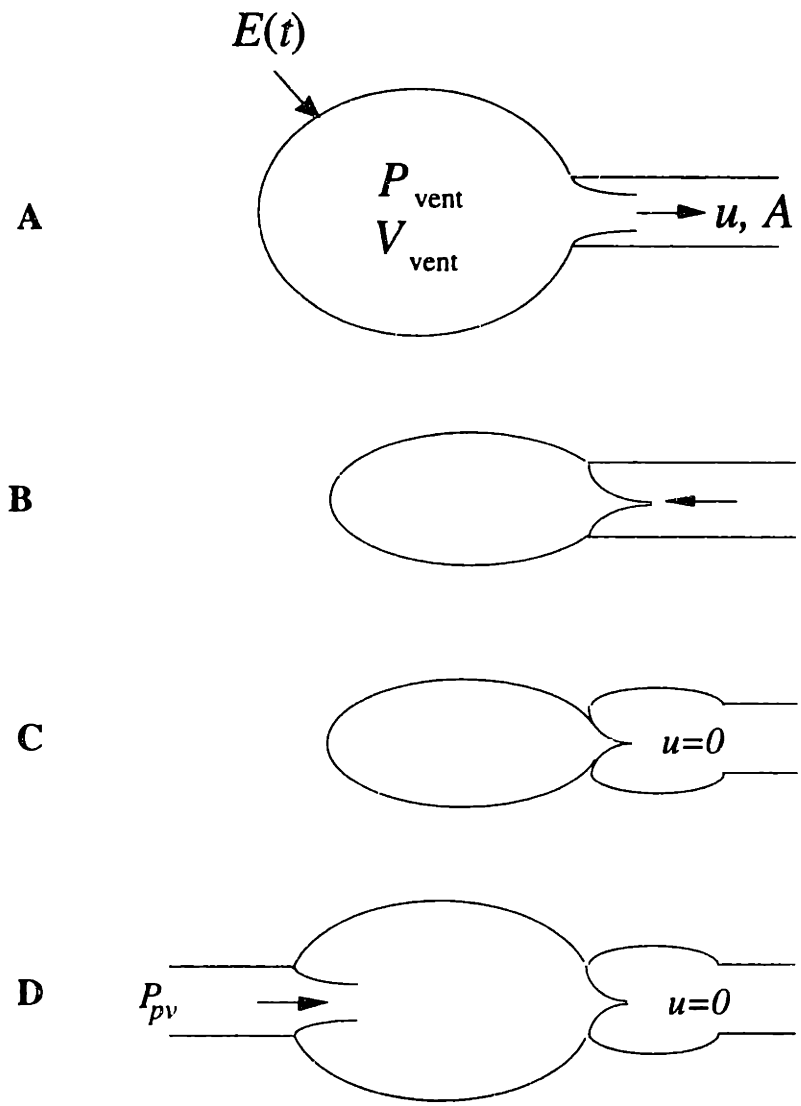

Figure 2.9. The phases of the left ventricle; A: early systole; B: late systole, with onset of flow reversal; C: filling of the sinus of Valsalva, and arrest of flow at aortic root; D: diastolic filling from the pulmonary venous system.

below aortic pressure due to ventricular emptying. The algorithm then proceeds to the next phase.

Phase 3: aortic valve closure and filling of sinuses of valsalva

As flow begins to move retrograde towards the aortic valve, the valve leaflets are swept backwards and closed without sustaining a significant pressure gradient. Numerically this is modeled by allowing to fluid to move backwards as though the left ventricle were refilling with negative flow from the aorta, using the identical equations from the description of the first and second flow phases. However, we eliminate equation (2.3.17) since this retrograde filling volume does not increase left ventricular volume, due to the fact that the valve leaflets are closed, but rather fills the sinuses of valsalva. This approximation is correct if one realizes that the pressure of the sinuses is close to left ventricular pressure, which is again true in light of the fact that the valve leaflets are unable to sustain a pressure gradient during this phase of the cycle.

Filling of the sinuses continues until the valve leaflets arrive at their maximally distended position, at which time the valve leaflets are able to sustain a large pressure gradient. This may be modeled as an abrupt decrease in the aortic root compliance to a new value, C_{sinus}. Thus, an equation can be written relating the aortic root pressure (at the upstream boundary node of the aortic root segment), the velocity in the same position, and the area (from the tubelaw) as follows:

$$\frac{dP_1}{dt} = -\frac{U_1 A_1}{C_{sinus}} \tag{2.3.18}$$

This equation is coupled with an upwind predictor-corrector scheme using momentum and continuity between the first two upstream nodes of the aortic root segment. This boundary condition is held during the entire diastolic phase, during which time the left ventricle refills.

Phase 4: diastolic left ventricle filling

During diastole when the left ventricle wall is in its inactive phase, the pressure in the left ventricle drops below left atrial pressure, which in the numerical simulation is set equal to the pressure at the pulmonary venous windkessel of the lumped parameter model, P_{pv} (see section 2.7). Once this valve opening condition is reached, the flowrate q_{pv}, across the left heart inflow resistive element R_{li} driven by the pressure gradient $\Delta P = (P_{pv} - P_{vent})$, is solved for. This corresponds to an increase in left ventricular volume:

$$\frac{dV_{vent}}{dt} = q_{pv} \tag{2.3.19}$$

which in turn leads to an increase in left ventricular pressure, governed by equation (2.3.14). Thus, filling continues until ΔP becomes negative, at which time q_{pv} is set to zero (corresponding to a closed mitral valve), and the calculation proceeds to the next phase. It is possible, however, for filling to continue into the next phase of early systole, where rising ventricular pressures due to the early contraction in systole forces ΔP to become negative, thus closing the mitral valve. The cycle then continues again, beginning with early systole and phase 1.

2.3.2.b Wall Compliance

The $E(t)$ curve is of importance in determining the shape of the forward pressure wave. Additionally, alterations in the strength of contraction due to impaired myocardium in heart failure can be modeled as alterations in this curve. As previously mentioned, extensive studies of the pressure-volume relationship in canine ventricles have been performed by Suga and Sugawa (Suga and Sugawa, 1974). From a large sampling they determined that the basic shape of the systolic portion of the pressure-volume curve remained unchanged, regardless of loading or inotropic changes. Thus, the systolic wall elastance may be characterized by two parameters only; the maximum wall elastance E_{max}, time to peak elastance T_{max}, and the dimensionless systolic elastance curve. The total length of the cycle is extrapolated from data presented by Suga and Sugawa suggesting that T_{max} spans approximately 30 - 50% of the total cycle. It is assumed that the falling and steady portions of the curve are less important to the simulation since the aortic valve is closed during these segments.

The basic mechanics which were elucidated in this classical study apply well to the mechanics of the ventricle in humans, although the exact form cannot be applied directly to a model of the human circulation, since certain parameters, most notably the ventricular elastance curve itself, do not scale from the canine to the human. A Fourier approximation made from the elastance curve was constructed and used to drive the ventricular model, coupled to the distributed arterial model (Figure 2.10-a). The elastance curve was scaled to match the maximum elastance values for the left and right ventricles. Explicit use of the elastance curve from Suga and Sugawa results in the incorrect result of an overshoot in left ventricle pressure early in systole, followed by a plateau or second peak during late systole immediately preceding valve closure (Figure 2.10-b).

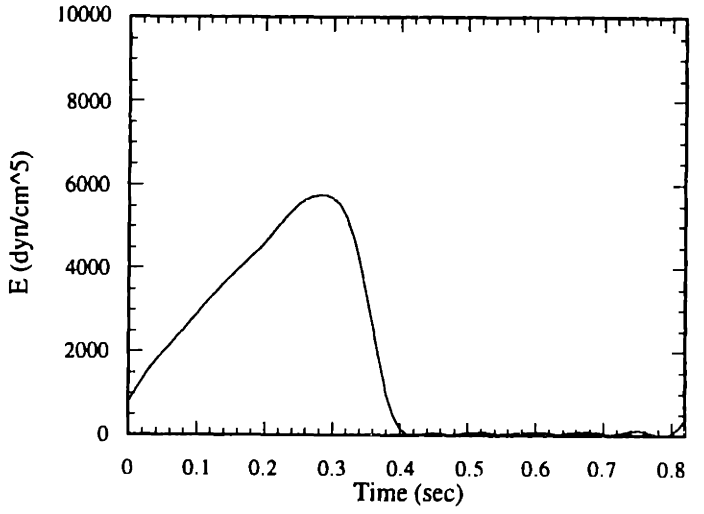

Figure 2.10-a. Fourier approximation of the left ventricular elastance curve, the shape of which was obtained from Suga and Sugawa's model.

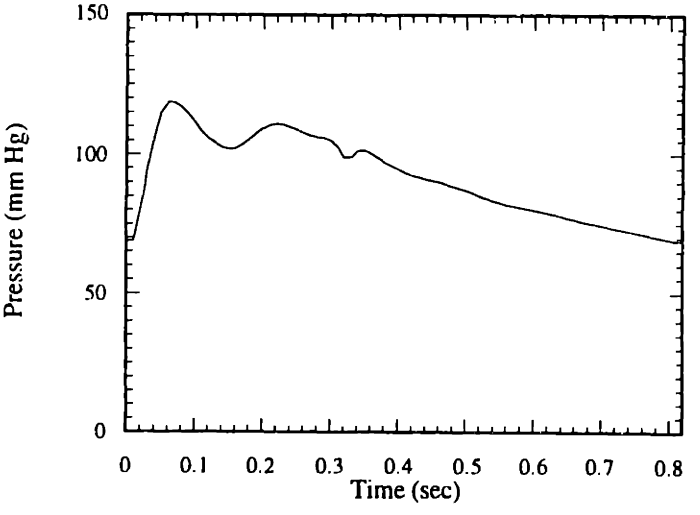

Figure 2.10-b. Resultant computed aortic root pressure curve using the left ventricular elastance curve in Figure 2.10-a.

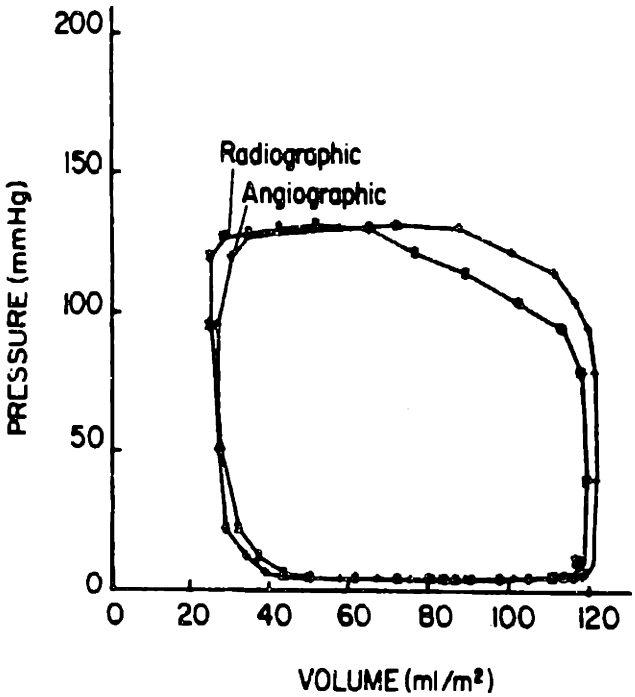

Figure 2.11-a. Left ventricle P-V loop measured from patients using angiographic techniques (MacKay, 1984). Each point corresponds to a measurement, each taken at equal intervals 50 msec apart.

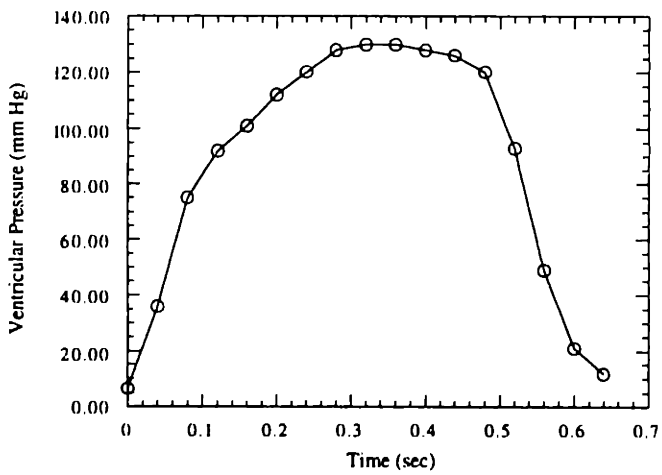

Figure 2.11-b. Left ventricle pressure as a function of time, extrapolated from Figure 2.12-a. The open circles indicate the individual points in time used to construct the curve.

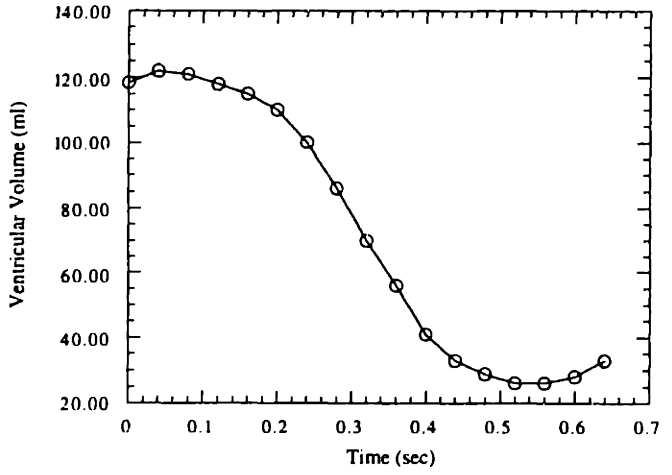

Figure 2.11-c. Left ventricle volume as a function of time, extrapolated from Figure 2.12-a.

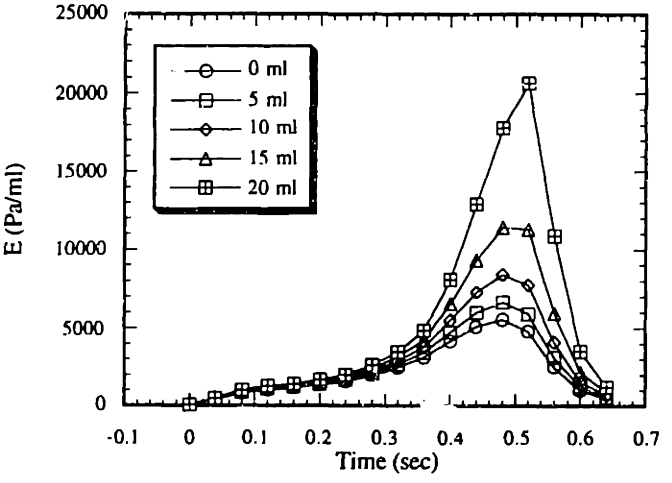

Figure 2.11-d. Left ventricle elastance as a function of time, extrapolated from Figure 2.12-a, for left ventricle zero-pressure volumes of 0, 5, 10, 15, and 20 ml.

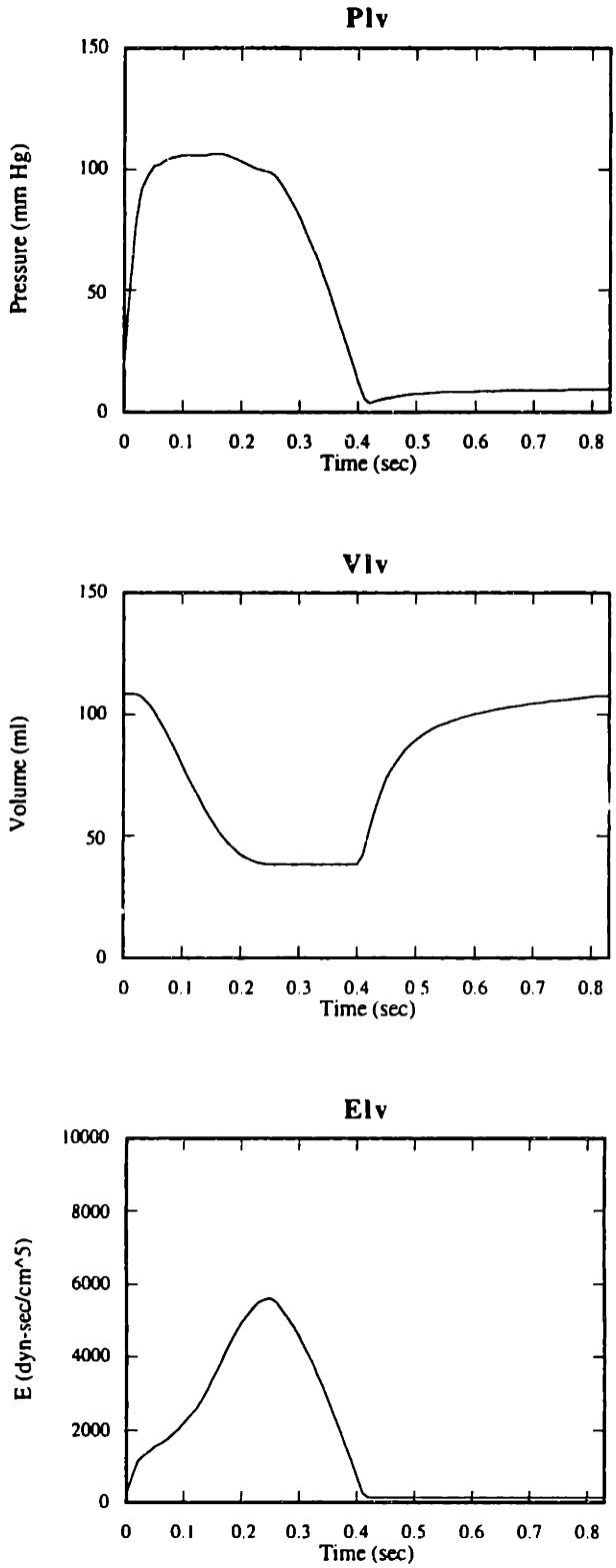

Figure 2.12. Plot of left ventricle pressure (top), volume (middle) and elastance (bottom) for the standard case, over one cycle. The zero pressure filling volume was equal to 15 ml.

Close investigation of the pressure-volume curve obtained in humans again demonstrates that there is a fundamental, morphological difference between the elastance curve in humans, and that obtained by Suga and Sugawa in the canine. A simple demonstration taken from measured pressure-volume (P-V) loops using catheterization techniques can help to elucidate the nature of the problem. If one considers the human P-V loop shown in Figure 2.11-a, obtained by McKay, and extracts from the plots pressure and volume in time (the individual data points are equally spaced in time), the plots shown in Figure 2.11-b and 2.11-c can be obtained for pressure and left ventricular volume versus time. Using equation (2.3.14), one can back calculate the $E(t)$ curve for the measured data, which is plotted in Figure 2.11-d. Clearly, the elastance curve shown here is qualitatively different from the curves measured in canines by Suga and Sugawa. The new curve follows the original curve suggested in Figure 2.10-a until about 0.08 seconds, when the curve is markedly characterized by a concavity during early systole.

Several investigators have already suggested that the form of the left ventricular pressure-volume relationship (2.3.14) for describing the coupling between left ventricular pressure and volume is overly simplistic. Indeed, tissue models of myocardial contraction often include, in parallel to the contractile element, both a resistive and elastic element which may be expected to cause a lag between pressure and volume. Suga and Sugawa have suggested the following form of the pressure-volume relationship in the canine as an improvement over their previous measurement of elastance:

$$P(t) = E^{*}(t)\left[V(t) - V_d\right]\left[1 - 0.0014(-dV/dt) - 0.0007(-dV/dt, \text{peak}) - 0.0054\left(\int -dV\right)\right] \tag{2.3.20}$$

where the coefficients are derived from experimental measurements on dogs, and $E^{*}(t)$ is the isovolumetric elastance curve (Suga and Sugawa, 1980). The time dependent *dV/dt* and derivative terms are most likely due to myocyte properties associated with uncoupling of the contractile elements during myocardial contraction. Additional investigators have also pointed out the significance of the *dV/dt* term. For the purposes of our model, we have found that the following form provides sufficient modeling of the physics to give realistic results:

$$P_{vent} = E(t)^{*} \cdot \left(V_{vent} - V_{vent,o}\right) \cdot \left(1 - \sigma\left(-\frac{dV_{vent}}{dt}\right)\right) + P_{th} \tag{2.3.21}$$

The coefficient σ is a scaling factor for the time-dependent effects, and P_{th} is the transthoracic pressure (the pressure difference between the thorax and the atmosphere),

which is expected to alter the left ventricular pressure and hence the peak pressures achieved in the arterial tree. This relationship is incorporated into the cardiovascular model in place of equation (2.3.14). The *isovolumetric* contraction curve $E^*(t)$ is assumed to be a pure half sinusoid, whose duration over the entire cycle can be specified as a parameter, the systolic to cycle time ratio. The resulting computed left ventricle pressure curve and volume curves are shown in Figure 2.12, and the calculated curve for $E(t)$ again using equation (2.3.14) is shown plotted at the bottom of Figure 2.12. One may compare these plots with the data shown in Figure 2.11 and be convinced that there is generally good agreement between the measured data and the computed curves. Some modification, however, may be made to the isovolumic elastance curve, in that the computed left ventricle pressure and apparent elastance both appear to have downward side slopes (during late systole) that are less steep than those observed *in-vivo*. The difficulty in refining the elastance curve comes from a lack of solid measurements of the human isovolumic contraction curve, which is extremely difficult to obtain.

2.3.3 Terminal Boundary Condition

In the physiological arterial system, the arteries continue to bifurcate until they reach diameters on the order of 100 micrometers, at which point they are called "arterioles". Arteries in general are characterized by their highly elastic properties (due to high amounts of elastin contained in their walls), as well as a smooth muscle cell layer which is responsible for regulation of tone. At the level of the arterioles, control of smooth muscle tone by both hormonal and neural mechanisms allows for control of both stiffness as well as diameter. Since arterioles are in general one or two generations away from the capillary bed, much of the control of flow into the capillary circulation in organ beds is done at the level of the arteriole, where the diameter and hence resistance to flow can be locally regulated. The process of regulation is a dynamic one, and tone can conceivably vary independently between arterioles as local tissue demands for oxygen and nutrients change with level of activity.

The numerical model described here allows for incorporation of linear segments that represent the larger vessels in the arterial tree, but to model the finer branching structure, as well as the arterioles, is completely impractical to use this method. Thus, to approximate the behavior of the smaller vessels we chose to model them as a lumped parameter windkessel, of the form used by previous investigators. Noordergraf's group introduced a modified form of the windkessel, shown schematically in Figure 2.14 (Berger et al., 1994; Berger et al., 1995). The model is advantageous in that it allows the behavior of an entire arteriolar and small vessel bed to be captured using few parameters.

It is further advantageous in that the phenomenon of wave reflections is reasonably approximated using this model, thus avoiding many of the artifactual and spurious reflections obtained if one uses a single resistive element instead, as many researchers have done in the past. The windkessel consists of a resistance R_s in parallel with a compliance C_s, where the resistance represents the high pressure drop associated with constriction of the arteriolar smooth muscle, and C_s represents the total compliance of the small artery network. In series with the traditional windkessel is an additional element Z_o, which represents the impedance of the parent branch to which the boundary condition is attached. The impedance may be approximated as the inverse of admittance Y, where $Y = A/\rho c$, where A and c are the cross-sectional area and wavespeed of the parent branch, respectively, and ρ is the density of the fluid medium.

From the electrical analog, the following equations may be written as a function of the resistances and capacitances:

$$\frac{P_c - P_v}{R_s} + C_s \frac{dP_c}{dt} = Q \tag{2.3.22}$$

$$Q = \frac{1}{Z_o}(P - P_c) \tag{2.3.23}$$

where Q is the entrance flow into the windkessel passing through Z_o, the entrance impedance. The impedance may be calculated from the inverse of admittance:

$$Z_o = \frac{\rho c}{A} \tag{2.3.24}$$

using values of area A and wavespeed c from the adjoining terminal element end node. A velocity or pressure wave which approaches the windkessel traveling down the parent branch would be expected to reach the terminal windkessel and be reflected backwards up the parent branch. The reflection coefficient Γ, which is the ratio of the amplitude between the incident and reflected wave is given by the following expression:

$$\left|\Gamma_A(\omega)\right| = \frac{R_s}{\left[\left(R_s + 2Z_o\right)^2 + \left(2\omega C_s R_s Z_o\right)^2\right]^{1/2}}. \tag{2.3.25}$$

As can be seen from the equation, an increase in R_s produces an increase in the reflection coefficient, which in turn produces an increase in the amplitude of the reflected wave. This phenomenon is observed physiologically when the tone of the arterioles increases with vasoconstriction, thus producing more pronounced reflected pressure waves. Generally speaking, if the tone of the arterioles and the smaller branching vessels increase with vasoactivity, then accompanying the increase in resistance is a decrease in vessel

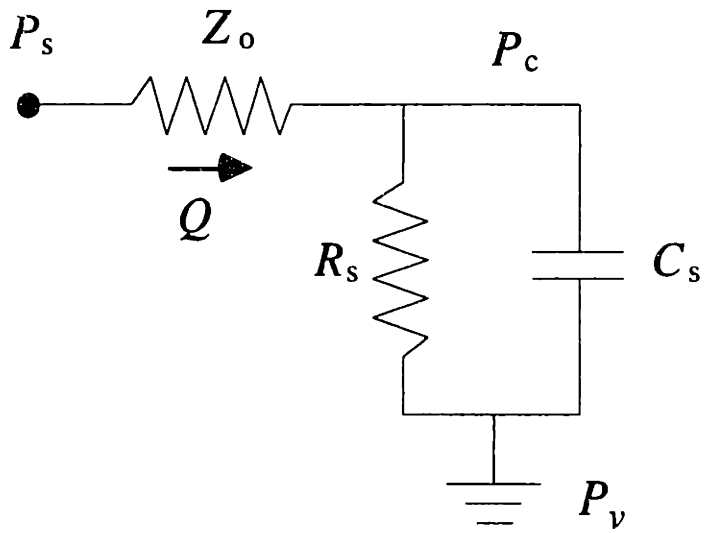

Figure 2.13. Modified windkessel for terminal boundary condition.

compliance; one notes from the equation that if the compliance C_s of the windkessel were to be decreased, then the same effect of increasing the reflection coefficient would be achieved. This relation only describes the wave reflection produced within the windkessel. An potential source of wave reflection is the impedance mismatch between the entrance impedance Z_0 and the parent branch. Thus, in order to avoid the generation of spurious reflections it is important that the impedances be matched so that the pure effects of modulating reflection at the terminal boundary condition comes from alterations in R_s and C_s alone.

2.3.4 Method of Characteristics

It is necessary to couple the windkessel to the parent segment using the method of characteristics, which is a standard numerical technique used to update boundary conditions on a one-dimensional grid. A derivation of the characteristic equations used is given below in the same manner as that derived by Kamm (Kamm, 1977). We begin with the equations of motion, for the straight elastic segments. After multiplying the continuity equation (2.2.2) by an undetermined factor λ and adding it to the momentum equation (2.2.1), we obtain the following relation:

$$\frac{\partial u}{\partial t}+u\frac{\partial u}{\partial x}+c^2\frac{1}{A}\frac{\partial A}{\partial x}+F+\lambda\left(\frac{\partial A}{\partial t}+\frac{\partial (uA)}{\partial x}+\Psi\right)=0 \tag{2.3.26}$$

where the pressure gradient has been substituted for using the definition of wavespeed:

$$c^2=\frac{A(P,z)}{\rho}\frac{\partial P}{\partial A}=\frac{A(P,z)}{\rho}\frac{\partial P}{\partial x}\frac{\partial x}{\partial A} \tag{2.3.27}$$

Using the following substitutions:

$$du=\frac{\partial u}{\partial x}dx+\frac{\partial u}{\partial t}dt \quad \text{and} \quad dA=\frac{\partial A}{\partial x}dx+\frac{\partial A}{\partial t}dt \tag{2.3.28}$$

we may obtain the reduced expression:

$$du(u+\lambda A)+dA(\frac{c^2}{A}+\lambda u)+\frac{\partial u}{\partial t}(dx-dt(u+\lambda A))+\frac{\partial A}{\partial t}(\lambda dx-dt(\frac{c^2}{A}+\lambda u))$$
$$+Fdx+\lambda\Psi dx=0 \tag{2.3.29}$$

leading to the final form of the characteristic equation:

$$du\pm c\frac{dA}{A}\pm\frac{c}{A}\Psi' dt+Fdt=0 \tag{2.3.30}$$

provided that the following definitions are made:

$$\lambda = \pm\frac{c}{A} \quad \text{and} \quad \frac{dx}{dt} = u \pm c \qquad (2.3.31), (2.3.32)$$

Equation (2.3.30) describes the movement of information passing from one node to the next, either in a rightward (upper sign), or a leftward (lower sign) direction. The equation can be written in a modified form, in terms of flowrate Q using equation (2.3.27), yielding the result:

$$dQ = \frac{A}{\rho c^2}(u\mu c)dP + (-F\mu c\Psi)dt = 0 \qquad (2.3.33)$$

The friction term F is replaced by the expression for unsteady friction derived previously as equation (2.2.21) in Section 2.2.4.a. This is the final form of the characteristic equation to be used to update the end node of the terminal branches.

Discrete finite difference forms of the characteristic equations can be developed as follows. Using linear interpolation, one can determine the value of the state parameters at the terminal node by following a characteristic line from its origin at the previous timestep (Figure 2.14). We therefore introduce the following notation. Given that the state variables of pressure P, velocity U, area A , and wavespeed c are known for the present timestep t at the terminal node (denoted by the subscript N) and its adjacent node (denoted by the subscript N-1) then we can seek a solution for the state variables at the next timestep $t+\Delta t$ denoted by the superscript j+1 (where j denotes the present timestep). The origin of the rightward (R) and leftward (L) running characteristic lines from the timestep t into the next timestep may be calculated using the following:

$$\underset{L}{X_R} = X_N - \frac{dt}{2}[(U_N^{j+1} \pm C_N^{j+1}) + (\underset{L}{U_R} \pm \underset{L}{C_R})] \qquad (2.3.34)$$

For the initial iteration, due to the implicit nature of the equation, we make the following approximations:

$$C_R = C_L = C_N^{j+1} = C_N^j \qquad (2.3.35)$$

$$U_R = U_L = U_N^{j+1} = U_N^j \qquad (2.3.36)$$

Hence using equation (2.3.34) we are able to estimate the values of P at the points X_R and X_L as follows:

$$P_R = P_{N-1}^j + \frac{(X_R - X_{N-1})}{\Delta X}(P_N^j - P_{N-1}^j) \qquad (2.3.37)$$

Similar calculations may be made for the other state variables A, U, Q, C, and Ψ. Since we are only applying the method of characteristics in the downstream direction at the out

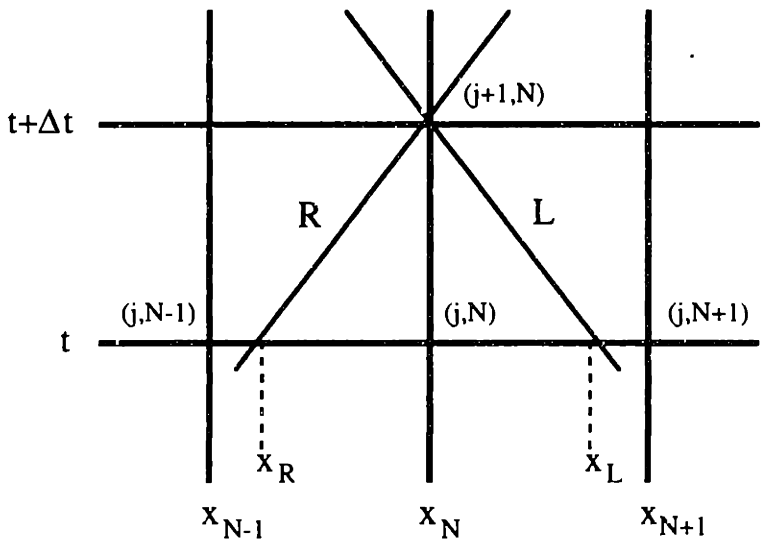

Figure 2.14. Characteristic lines at the boundary.

flow end of the terminal branches, we need only concern ourselves with the rightward running characteristics. We may now write equation (2.3.33) in difference form:

$$Q_N^{j+1} = Q_R + \Lambda(P_N^{j+1} - P_R) + \Gamma \tag{2.3.38}$$

where

$$\Lambda = \frac{1}{2}\left\{\left[\frac{A}{\rho C^2}(U-C)\right]_N^{j+1} + \left[\frac{A}{\rho C^2}(U-C)\right]_R\right\} \tag{2.3.39}$$

and

$$\Gamma = \frac{\Delta t}{2}\left\{-[FA + C\Psi]_N^{j+1} - [FA + C\Psi]_R\right\} \tag{2.3.40}$$

To complete the boundary condition, it is necessary to include the constraint provided by the terminal Windkessel. Using the equation (2.3.24) relating windkessel outflow to the terminal node pressure in finite difference form,

$$P_N^{j+1} = P_c^{j+1} + Q_N^{j+1} Z_o \tag{2.3.42}$$

and substituting for the flowrate term with equation (2.3.36), an expression for the updated terminal node pressure can be written as:

$$P_N^{j+1} = \frac{(Q_R - \Lambda P_R + \Gamma)Z_o + P_c^{j+1}}{1 - \Lambda Z_o} \tag{2.3.43}$$

where

$$P_c^{j+1} = P_c^j + dt\left(\frac{Q_N^j}{C_s} - \frac{P_c^j - P_v^j}{C_s R_s}\right) + \left(P_v^{j+1} - P_v^j\right) \tag{2.3.41}$$

may be derived from the governing equations for the terminal windkessel.

Hence, solving first equations (2.3.39) and (2.3.40) followed by equation (2.3.42) gives the values of pressure and flowrate at the endnode N for the new timestep $t+\Delta t$, which also allows for calculation of the area, using the inverse tubelaw, and consequently the velocity. These values are calculated and stored prior to calculation of the internal points, allowing for the explicit calculations required by the discretization scheme described above.

2.4 Lumped Parameter Model of Venous and Pulmonary Circulations

Since this model primarily concerns itself with the interactions of clinical interventions with the arterial tree, the venous and pulmonary circulations are modeled as lumped parameters. It should be noted, however, that given accurate data for these other segments of the circulation, a network model similar to the arterial tree may be constructed. Lumped parameter models are simple to construct and are easily incorporated into the numerical simulation. An electrical analog of the venous circulation, pulmonary circulation, and the right heart may be constructed as previously developed by Davis (Davis, 1991). The system consists of resistors, capacitors (both static and time-varying), and diodes arranged as shown in Figure 2.15. Thus, each venous or arterial bed may be represented as having an inherent resistance and compliance represented by single elements, that reflect the total resistance and wall compliance of every vessel segment that the bed is composed of. This model is fairly typical of other lumped parameter models of the circulation previously constructed, although in this model inertial effects are ignored, which other investigators have chosen to include (Westerhof et al., 1968).

From the electrical analog in Figure 2.15, the following differential equations may be written:

$$\frac{dP_v}{dt} = \frac{q_b - q_{ri}}{C_v} \tag{2.4.1}$$

$$\frac{dP_{rv}}{dt} = \frac{q_{ri} - q_{ro} - (P_{rv} - P_{th}) \cdot dC_{rv}(t)/dt}{C_{rv}(t)} \tag{2.4.2}$$

$$\frac{dP_{pa}}{dt} = \frac{q_{ro} - q_{pa}}{C_{pa}} \tag{2.4.3}$$

$$\frac{dP_{pv}}{dt} = \frac{q_{pa} - q_{pv}}{C_{pv}} \tag{2.4.4}$$

$$q_{ri} = \begin{cases} \dfrac{P_v - P_{rv}}{R_{ri}} & P_v > P_{rv} \\ 0 & P_v < P_{rv} \end{cases} \tag{2.4.5}$$

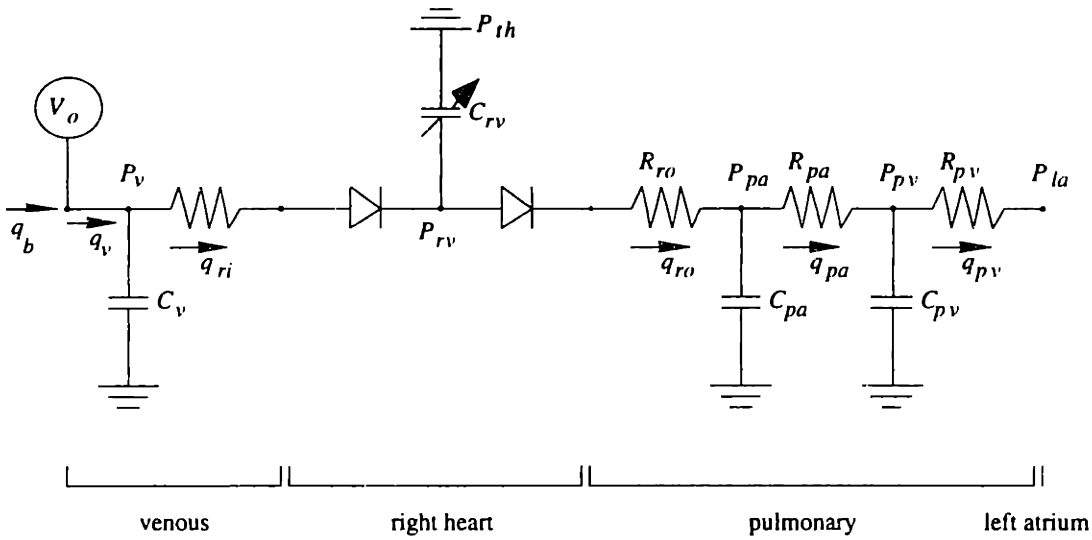

Figure 2.15. Electrical circuit analog of the venous and pulmonary circulation.

$$q_{ro} = \begin{cases} \dfrac{P_{rv} - P_{pa}}{R_{ro}} & P_{rv} > P_{pa} \\ 0 & P_{rv} < P_{pa} \end{cases} \tag{2.4.6}$$

$$q_{pa} = \frac{P_{pa} - P_{pv}}{R_{pa}} \tag{2.4.7}$$

$$q_{pv} = \frac{P_{pv} - P_{la}}{R_{pv}}. \tag{2.4.8}$$

The unidirectionality of the right heart valves are imposed on the right heart inflow and outflow tract flowrates depending on the direction of the pressure gradient across the inflow and outflow resistances, using equations (2.4.5) and (2.4.6). The shape of the compliance curve $C_{rv}((t)$ for the right ventricle is obtained by using the inverse of the normalized elastance curve presented in Section 2.3.2, and adjusting the minimum and maximum elastances to match the compliance values given in Section 3.1.6 (note that elastance is the reciprocal of compliance). Boundary conditions must be applied to the model, and include inflow from the capillary beds q_b which is obtained by summing the total outflow from the arterial system; the flowrate to the left atrium q_{pv} which is calculated from the left ventricular model outlined in Section 2.3.2; and P_{th} which again represents the transthoracic pressure. For the present model the effect of respiration is neglected and thoracic pressure is assumed to be constant. Transthoracic pressure is a negative quantity, owing to the fact that the inspiration of air into the lungs is a process that requires generation of negative intrathoracic pressures to provide the necessary pressure gradients to draw air into the airways. The pressure gradient remains negative during passive exhalation and at end exhalation, due to the elastic recoil of lung tissue. Note that the effect of increasingly negative transthoracic pressures is to increase the left ventricular end-diastolic volume. The equations that govern the lumped parameter model may be solved with fourth-order Runge Kutta, with the arterial outflow q_b as a boundary condition. Since the Runge Kutta scheme requires a timestep that is one order of magnitude larger than the one required for the distributed model solved using the MacCormack scheme, it is necessary to iterate on the lumped parameter model approximately every ten distributed model timesteps. Furthermore, for the period when the distributed model is solved in between the Runge-Kutta timesteps, q_b must be calculated by integrating the volume expelled from the arterial system, then by dividing this quantity with the elapsed time between the Runge-Kutta iterations.

The lumped parameter model allows the user to capture some of the features of certain cardiovascular disease states, which may be seen as alterations in the normal pressures in either the pulmonary or venous compartments. These effects are secondary to alterations in the resistances or compliances of these compartments, although more often their alterations are compensatory changes due to, for instance, decreased pumping ability of the right or left ventricles as seen in heart failure. However, since we are interested primarily in the function of the arterial system as an indicator of disease, and since our non-invasive measurements are primarily limited to this portion of the circulation, it seems reasonable to use the lumped parameter model to provide the correct interactions with the remainder of the cardiovascular system. The selection of parameter values for the lumped parameter models will be discussed in further detail in Chapter 3.

2.5 Baroreceptor Reflex

When the model was in its initial stages of construction, we decided that a baroreceptor reflex system would be required to adequately model the human response to mechanical or pharmacological interventions. As stated in the introduction, however, the focus of the research has since moved away from predicting the response to interventions to that of attempting to estimate the hemodynamic parameters for a given patient at the time of measurement. Thus, it is no longer necessary to consider the transient response, since a group of measurements taken at one specific time corresponds to a single set of hemodynamic parameters that define the patient's condition. This is of course provided that this condition does not change appreciably during the time it takes to collect all of the necessary hemodynamic data. Nonetheless, if one is interested in developing the cardiovascular model for use in other applications where the transient changes in the cardiovascular system are of interest, then a baroreceptor reflex will be essential. Multiple applications of a cardiovascular system model with feedback control will be given in the final chapter.

The baroreceptor reflex is a physiological system by which the autonomic nervous system autoregulates systemic arterial blood pressure. Under normal conditions, mean arterial blood pressure is held nearly constant by two main mechanisms: the renin-angiotensin-aldosterone axis, and the baroreceptor reflex. The former mechanism is primarily under the control of the kidneys, which responds to changes in perfusion of the glomerular apparatus that form the core of the renal filtration system. A decrease in glomerular perfusion, presumably as a result of decreased blood pressure, results in the release of renin into the circulation by specialized cells in the kidney. The circulating

renin travels to the lung where it participates in the transformation of a precursor, angiotensin I, into its active form, angiotensin II. Angiotensin II is a potent vascular smooth muscle cell constrictor, and liberation of the hormone causes global vasoconstriction, which increases systemic vascular resistance and raises arterial mean pressure. Angiotensin II has additional effects on the secretion of aldosterone, which acts on the kidneys to reduce salt excretion, and hence water loss, thus maintaining fluid volumes.

The latter mechanism, the baroreflex, is a nervous system control loop which acts much more quickly than the renin-angiotensin-aldosterone system. Immediately distal to each carotid bifurcation in the neck is an outpouching of the artery wall called the carotid sinuses. Imbedded in the walls of the sinuses are sensory nerve cells that respond to stretch, and hence the internal pressure of the carotid. Signals from the bundles of stretch receptors (known as the carotid bodies) are sent to the central nervous system and compared against a set point. Signals are sent out from the central nervous system via the autonomic nervous system, which have two branches: the sympathetic and the parasympathetic autonomic nervous systems. Both branches have far reaching effects in the control of bodily function, particularly in the control of the cardiovascular system, and counter each other's effects in a "yin-yang" fashion. Branches of the sympathetic autonomic act to increase heart rate, increase ventricular contractility, increase peripheral resistance, and promote venous return. The sympathetics are sometimes referred to as the "fight or flight" system, which prepares the body for physical exertion in the face of danger. The parasympathetic autonomic, on the other hand, acts to decrease heart rate, decrease ventricular contractility, while changing peripheral resistance very little. Thus, it is readily apparent that if systemic blood pressure is lowered, the primary response of the baroreflex system is to increase sympathetic tone; if blood pressure rises above normal, parasympathetic tone is alternatively increased.

The baroreceptor model used here is relatively simple, and was originally developed by DeBoer (DeBoer et al., 1987) . A schematic control loop diagram is shown in Figure 2.16. Note that the two branches of the nervous system are included, where the sympathetic system acts via two separate types of nerve fibers, the α and β fibers. Furthermore, the response to a difference between the systemic arterial blood pressure and the "setpoint" pressure can be modeled as a convolution. Thus, the response is dependent on the history of the error, and is weighted according two specified functions associated with the two autonomic branches. The response from the autonomic nervous system (ANS) is directed towards modulation of various hemodynamic parameters. One

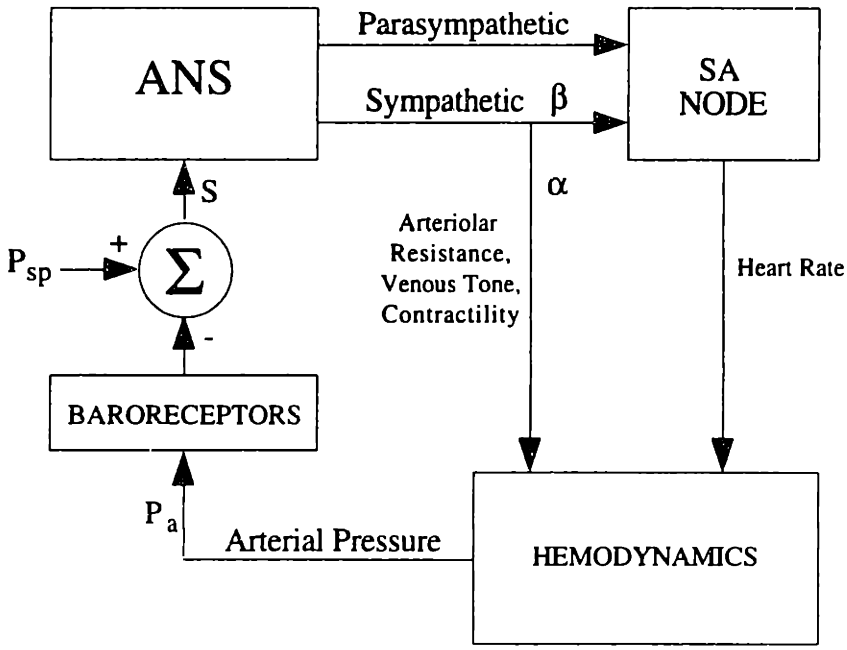

Figure 2.16. The baroreflex loop. Adapted from Davis , 1991.

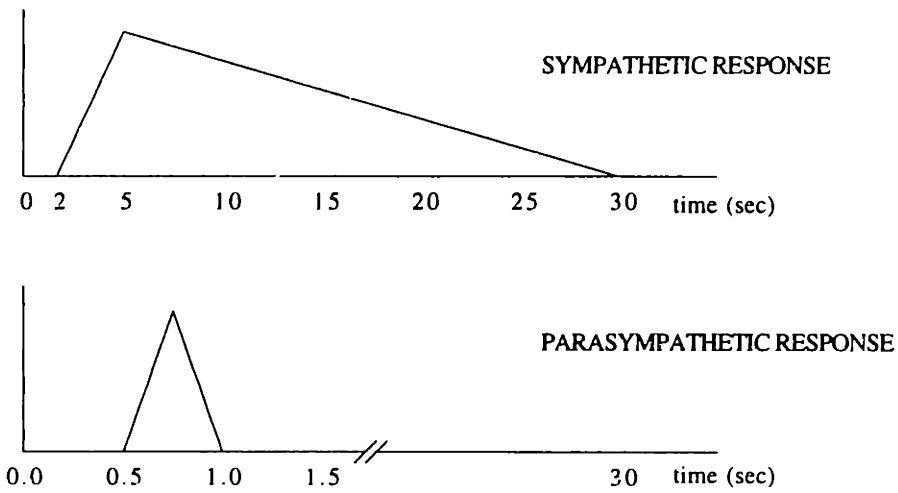

Figure 2.17. Sympathetic and Parasympathetic response. Adapted from Davis, 1991.

Table 2.1. The reflex gain values used for baroreflex control. From Davis, 1991.

Reflex Limb	Gain	Nerve Timing
heart rate	18.0 ms/mm Hg	β– & parasympathetic
left ventricle elastance, $C_{l,sys}$	0.007 ml/mm Hg^2	β-sympathetic
right ventricle elastance, $C_{r,sys}$	0.021 ml/mm Hg^2	β-sympathetic
peripheral resistance	0.011 PRU/mm Hg	α-sympathetic
volume, $V_{v,o}$	26.5 ml/mm Hg	α-sympathetic

can define the error $\bar{p}'[n]$ between the pressure measured at the carotid and the setpoint at one cycle (heartbeat) n by the function:

$$\bar{p}'[n] = 18\tan^{-1}\frac{\bar{p}[n]-\bar{p}_o}{18} \tag{2.5.1}$$

where $\bar{p}[n]$ represents the measured mean pressure during cycle n, and $\bar{p}_o$ is the desired setpoint mean pressure. This function is derived from experimental data and reflects the high sensitivity of the carotid bodies to a stimulus (i.e. stretch) near the setpoint pressure. As diagrammed in Figure 2.16, the error signal is transmitted to the autonomic system, where efferent pathways carry signals to the heart and peripheral vasculature. The afferent signals may be modeled as convolutions between the history of the setpoint error over time, and a weighting function specific to each limb of the autonomic nervous system. The autonomics can be assumed to have clearly defined effects on five reflex limbs of the cardiovascular system: peak elastance of the left and right ventricles (inotropy), heart rate (chronotropy), systemic vascular resistance (or vascular smooth muscle tone), and total blood volume. Hence, the following convolution integrals may be written:

$$I[n] = I_o + \int_0^T a(\tau)s'(t-\tau)d\tau \tag{2.5.2}$$

$$T'[n] = T_o + \int_0^T b(\tau)s'(t-\tau)d\tau \tag{2.5.3}$$

$$C_{l.r.sys}(t) = C_{l.r.sys.o} + \int_0^T c(\tau)s'(t-\tau)d\tau \tag{2.5.4}$$

$$V_{v.o}(t) = V_o + \int_0^T d(\tau)s'(t-\tau)d\tau \tag{2.5.5}$$

where $I[n]$ is the interbeat time interval, $T[n]$ is the arterial time constant (assuming the entire arterial system may be modeled as a single windkessel with an associated resistance and compliance), $C_{l.r.sys}$ is the minimum left and right ventricle compliances during systole, and $V_{v.o}$ is the total blood volume. Addtionally, these expressions include the constants I_o, T_o, $C_{l.r.sys.o}$, and V_o, which are the interbeat time interval, systemic arterial time contant, left and right heart systolic compliances, and total blood volume, respectively, of the standard nominal case. These equations were also described by DeBoer, and subsequently used by Davis in CVSIM. Note that in each integral the error s' is convolved with the weighting functions $a(\tau)$ through $d(\tau)$, respectively. These weighting functions are formed by linear combinations of the response curves for the two separate limbs, the sympathetic and the parasympathetic autonomics. The response

curves for each limb are shown in Figure 2.17 over a thirty second period, where the maximal response in each case corresponds to gain values specific to each reflex limb. These gain values are summarized in Table 2.1. The shape of the response curves were obtained by Berger (Berger et al., 1989), and used by Davis. Each appropriate curve is made dimensional by multiplying its y-axis value by the specified gain, thus giving the weighting function for each reflex limb. Note that the interbeat interval weighting function $a(\tau)$ is a sum of both the sympathetic and the parasympathetic response curves scaled by the appropriate gain. Computationally, values for mean pressure measured at the carotids are stored for each beat, and stored in an array so that the history of mean pressures may be convolved with their weighting functions, in a similar fashion to the summation convolution approximation performed in the transient wall shear calculation.

Additionally, the implementation of the blood volume regulation is incorporated into the lumped parameter model of the venous circulation. The storage of venous volume can be represented as a virtual "piston" which withdraws or adds fluid to the entire system as needed: this is represented by the circle-shaped unit labeled V_a in the diagram of the lumped parameter model in Figure 2.15. Thus, since the total blood volume in the entire model can be easily calculated at any given instant in time, additional volume may be added or removed using the volume control specified by equation (2.5.5).

As mentioned previously, the baroreceptor reflex is in place in the present model, but is deactivated for the purposes of system identification. It is important to note that the long time constant of the sympathetic autonomic nervous system makes it impractical for multiple calculations, where computational times can be extended by a factor of 10 or more. Validation of the reflex loop will not be included in this thesis, although it has been worthwhile to point out the interaction between the cardiovascular and the reflex model. This demonstrates the great flexibility of the numerical model to integrate many new and different aspects of the circulatory system easily into the code.

2.6 Program Architecture

The core simulation program (*networks.c*) was developed over a two year period, and was written using the UNIX C programming code. As mentioned before, the architecture of the code is designed so that any given network, with its own geometry and other parameters, may be created by altering only the input data file. Thus, separate cases may be defined and executed without recompilation of the main code. The data can be read in from a text file created by the Microsoft spreadsheet package Excel, which allows for easy entry and clear display of all relevant parameters. The code was written in C so that

the program could be easily incorporated into a number of commercial software packages, which generally accept user-defined functions programmed in C.

The input files are first read into the program, and all parameters and lumped parameter model values initialized. A lumped parameter model of the whole cardiovascular system, identical to Sah's model, is used to determine the steady state pressures at end diastole for all of the compartments. The derived steady-state pressure is used as the initial pressure for the distributed arterial model, and all velocities are initially set to a small value close to zero, since a value equal to zero will cause problems during initialization of certain variables that are functions of the inverse of velocity. Once the initial conditions are specified, the code marches forward in time, updating the state variables of pressure, velocity, and area at each nodal position using the MacCormack scheme. Simultaneously, routines update the boundary conditions at the bifurcations, terminal distal boundaries, and at the aortic root (left ventricle). The variables for the lumped parameter model of the venous and pulmonary circulations are updated at intervals which are multiples of the MacCormack scheme timestep, as mentioned in Section 2.2.3. Iteration continues until the solution reaches a steady state, where the values of pressure measured at the root of the aorta over one cycle deviates less than 5% from the previous cycle. When this condition is satisfied, the calculation is terminated. If a good intial guess for mean arterial pressure is provided, the calculation generally reaches convergence after 2 to 3 cycles, at approximately 10 to 15 minutes per cycle on the fastest available machines in our laboratory (DEC Alpha workstations).

The addition of the viscoelastic arterial wall mechanism creates a destabilizing condition that prevents use of the timestep as specified by the Courant condition equation (2.2.13). The cfl number is multiplied by a coefficient equal to 0.3, which was determined by trial and error to be the largest coefficient possible to maintain numerical stability. The use of the reduced cfl number, however, results in longer computational times. Additional factors that affect computation time are the total number of nodes in the model, as well as wall stiffness which affects wavespeed. Additionally, the number of timesteps stored for the viscoelastic and transient wall friction calculations are also proportional to the computational time, and are a significant factor in determining total run times. Times can be shortened to a certain extent by storing values for the convolution from every 2 or 3 timesteps, thus reducing the number of times the convolution calculation has to be carried out. As will be shown in Chapter 4, the total run time for the code is an important consideration in developing a feasible parameter estimation scheme.

Chapter 3

Standard Case

3.1 Definition of the Standard Case

A wealth of information on cardiovascular system parameters exists, although the data are highly variable and extremely dependent on the state of the individual or animal at the time when measurements are taken. Nonetheless, a standard case that produces a reasonable model output for a given set of parameters is needed in order to define a starting point from which certain parameters may vary. This becomes highly important when system identification is applied, and the parameters are adjusted around the standard case to achieve a model output identical to *in-vivo* measurements.

In the previous chapter the mathematical theory behind the cardiovascular model was discussed. In this chapter, the selection of parameters and the initial conditions are presented. Previous models of the cardiovascular system have generally drawn from a few papers in order to specify their parameters. In general, it is difficult to obtain complete information regarding the length, diameter, and stiffness of the major arteries in the human circulatory system. Thus if one study yields reasonable results, the study tends to stand as the definitive in the literature since the effort to repeat it by an independent researcher seems excessive. In the present study, some attempt was made to obtain literature values from as many sources as possible, and to compare and contrast the stated properties in order to determine which ones were suitable for use in the numerical model. We will begin this chapter by a discussion of the layout of the arterial system and its physical properties. We will then discuss the distribution of cardiac output in the normal state, the influence of bifurcations on flow, left ventricular parameters, and finally parameters for the lumped parameter approximation of the venous and pulmonary circulations. Parameters associated with the baroreflex control will not be discussed, as its inclusion into the model is not essential for parameter estimation.

3.1.1 Properties of Blood

The literature on the rheology of blood is substantial, and it has been shown that the density and viscosity of blood depends heavily on the composition of blood, as well as

the vessel diameter and shear rate for the latter. The principles of shear thinning and the formation of rouleaux, which are agglomerations of red blood cells, are well documented and have well-defined effects on blood viscosity. Additionally, the hematocrit (the percentage by volume of blood composed of cells) affects both viscosity and blood density. These effects, however, only become important for very small vessels, and are insiginificant in the main arterial tree. Additionally, the blood density varies over a small range and remains close to the density of water over all physiological conditions. Since in developing our model we are more concerned with the gross behavior of blood in large arteries, we are well justified in using fixed values for blood viscosity and density. From literature, blood has a density ρ of approximately 1.04 g/cm^3, slightly more dense than water due to the high protein, ion, and cell content of blood. Additionally, since blood is in fact a suspension of small particles that comprise about 40% of total blood volume, one would expect the viscosity to be higher than that of water. An approximate literature value for μ is 0.04 cp for blood flow in large arteries (Fung, 1981). One can assume that neither viscosity nor density changes significantly physiologically, except in extreme cases of dehydration where the hematocrit may increase drastically, or in the case of certain hematological abnormalities, such as sickle cell anemia. Although sickle cell anemia is not accompanied by an increase in the blood viscosity *per se*, its effects mimic that of an increase in peripheral resistance due to blockage of the microvasculature by stiffer than normal erythrocytes. In the larger vessels, however, the increased stiffness has a negligible effect. As will be shown in Chapter 4, small deviations in both ρ and μ have insignificant effects on the overall behavior of the large arteries.

3.1.2 Arterial Tree Layout and Arterial Segments

As mentioned in Chapter 2, much of the basic design of the model was based upon the work of Stettler et al., who for the most part based their model geometry on the measurements provided by Avolio (Avolio, 1980). Avolio's paper contains an extensive list of arterial lengths, diameters, wall thicknesses, and Young's moduli for most of the major human arteries (a sum total of 128). Thus, due to the elemental nature of the numerical model, the data may be adapted for use easily. Although the model is certainly capable of handling an unlimited number of artery segments, a larger number of elements corresponds to longer calculation times. Thus, 28 elements were selected to represent the behavior of the most major artery segments. This network is shown schematically in Figure 3.1. Each element is assigned a number, as is each bifurcation. The numbered elements correspond to specific major arteries, as outlined in the first two columns of Table 3.1. Due to the symmetry of arteries between the two leg segments and the renal

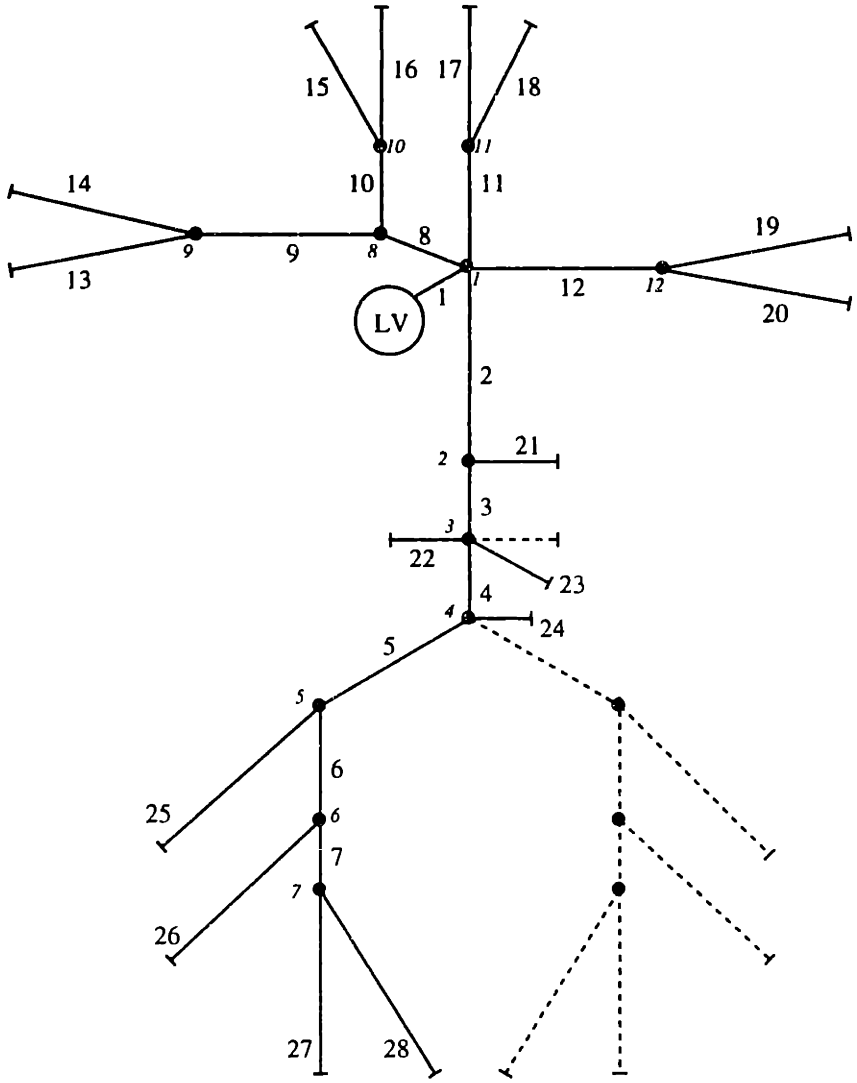

Figure 3.1. The 28 element distributed model of the arterial system. Dashed elements represent those that are reflected by symmetry.

Table 3.1. Specifications for the 28 element model: arterial properties.

element #	artery name	element type	length (cm)	proximal area (cm^2)	distal area (cm^2)	E x 10^6 (dyn/cm)	K (sec^{-1})
1	ascending aorta	1	5.5	6.605	3.941	4.0	0
2	thoracic aorta	0	18.5	3.597	2.835	4.0	0
3	abdominal aorta	0	4.3	2.378	2.378	4.0	0
4	abdominal aorta	0	9.6	1.021	1.021	4.0	0
5	common iliac	0	19.2	0.849	0.229	4.0	0
6	femoral artery	0	43.2	0.181	0.126	8.0	294
7	anterior tibial artery	0	1.5	0.053	0.053	16.0	294
8	brachiocephalic	0	2.4	1.208	1.208	4.0	0
9	r brachial	0	41	0.503	0.181	4.0	196
10	r common carotid	0	16.8	0.503	0.503	4.0	0
11	l common carotid	0	11	0.503	0.503	4.0	0
12	l brachial	0	44.4	0.554	0.181	4.0	196
13	r radial	2	23.2	0.08	0.08	8.0	294
14	r ulnar	2	22.9	0.139	0.113	8.0	294
15	r external carotid	2	11.3	0.196	0.071	8.0	294
16	r internal carotid	2	17.2	0.283	0.053	8.0	196
17	l internal carotid	2	17.2	0.283	0.053	8.0	196
18	l external carotid	2	11.3	0.196	0.071	8.0	294
19	r radial	2	23.2	0.139	0.113	8.0	294
20	r ulnar	2	22.9	0.08	0.08	8.0	294
21	coeliac	2	1	0.478	0.478	4.0	196
22	renal	2	2.7	0.212	0.212	4.0	294
23	sup mesenteric	2	5.4	0.581	0.581	4.0	196
24	inf mesenteric	2	4.5	0.08	0.08	4.0	294
25	profundis	2	12.1	0.166	0.166	16.0	294
26	post tibial	2	30.6	0.102	0.102	16.0	294
27	ant tibial	2	29.5	0.031	0.031	16.0	294
28	peroneal	2	31.3	0.053	0.053	16.0	294

arteries, many artery segments can be reflected over, thus reducing the number of nodes needed and also reducing calculation times. These reflected elements are indicated by the dotted lines in Figure 3.1.

Arterial segments were specified in the model by a proximal and distal internal radius, from which the cross-sectional areas were calculated. Although no specific internal arterial pressure was specified by Avolio at which the measurements were taken, it was assumed that the standard or resting state corresponded to an internal pressure of 100 mm Hg. Area was assumed to be a linear function of length between the two specified boundary areas. In addition to specifying the length of each element, the spatial increment used in the calculation, Δx, is also specified for each element. The increment nominally took on a value close to 1.0 cm, where the total artery length was divided by the nearest integer value. It must be noted, however, that the numerical calculation using the predictor-corrector scheme requires at least 3 nodes per element. Thus, for several elements that were shorter than 2.0 cm, Δx took on a value of less than 1.0 cm, dividing their shorter lengths by two to obtain a value for the spatial increment. This has implications towards decreasing the calculated Δt using equation (2.2.13) (and hence increasing the length of calculation), compared to the case where all of the elements have the identical Δx close to 1.0 cm. The branching pattern of the arteries, and the specification of which particular elements join at any given bifurcation, was also taken from the arterial tree layout given by Avolio. Bifurcation branching angles were not specified by Avolio, and indeed it is a difficult task to locate any published values for branching angles for the entire circulatory system. Perhaps the best resource for such values is an atlas of human anatomy and a protractor, from which the angles can be estimated from the images. This will be discussed in more detail later in the Section 3.1.3.

A minor deviation to the specified arterial data from Avolio was made in order to accommodate the inaccuracies seen in calculating mean flowrates in the carotid arteries using Murray's cost function. Use of the internal, external, and common carotid dimensions provided by Avolio lead to unrealistically high values for carotid artery flowrates, as calculated in Section 3.1.4. Indeed, the blind application of the cost function leads in many cases to inaccuracies that must be adjusted for, either by altering the geometry or the coefficients associated with the cost function, within reasonable limits. Thus, the common, internal, and external carotid artery dimensions obtained from the studies of Bharadvaj (Bharadvaj et al., 1982) were used to provide more reasonable measurements, thus allowing for more correct calculated mean flowrates in elements 10,

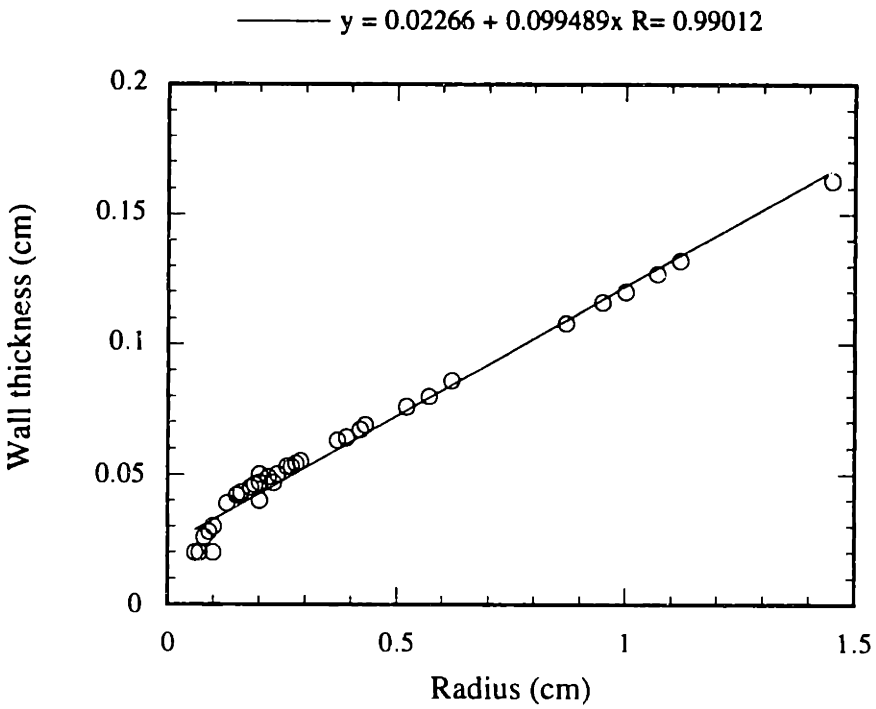

Figure 3.2. Relationship between artery radius and wall thickness. Data taken from Avolio, 1980. The linear fit is given by the equation at the top of the graph.

11, 15, 16, 17, and 18. These new values are given in Table 3.1 for the specified elements.

In addition to geometrical measurements, the material properties of each artery segment were specified in order to calculate the nominal reference wavespeed c_o for each element, which is taken to correspond to the reference internal pressure of 100 mm Hg. The wavespeed can be calculated using the Moens-Korteweg equation. The equation has the form:

$$c = \sqrt{\frac{E \cdot h}{2 \cdot \rho \cdot R}} \tag{3.1.1}$$

where the wavespeed c is a function of Young's modulus E, inner radius R, fluid density ρ, and wall thickness h. Avolio specifies wall thickness individually for each artery, but an alternative way in which to specify thickness becomes apparent if one plots thickness versus radius data from Avolio. This relationship is shown in Figure 3.2, and as can be easily seen there exists a well-defined linear function which can be taken advantage of. Thus, the numerical model calculates the radius at each node, given the imposed linear relationship between distance and area, and from radius calculates wall thickness based on the linear regression function. Since the Young's modulus E for each segment is specified, the reference wavespeed can be calculated using equation (3.1.1), assuming a value for the density of blood. Young's modulus is specified for each element in the seventh column of Table 3.1, and was obtained from Avolio's original data as well.

In addition to geometry and wall properties, each artery is "classified" in terms of element type: an element bounded on both ends by other elements is denoted as element type "0". An element that ends in a terminal windkessel is labeled as element type "2". The single element bounded on its proximal end by the left ventricle is labeled as element type "1", and is always given the element number 1 as well. Additionally, note that the element numbering system requires that all elements of type "0" precede numerically all those of type "2". Hence, as seen in the third column of Table 3.1, all terminal elements are those labeled 13 through 28; this group of elements is preceded by the group of "internal" elements 2 through 12. It is important to retain this numbering scheme so that all terminal elements are the highest in numbers, since *networks.c* uses this order to determine the distribution of cardiac output, where the flow from each element is summed in order of decreasing element numbers until the aortic root (element 1) is reached. From this, the program then calculates the appropriate values of transmural wall leakage and peripheral resistance. The selection of parameters contained in the final

column of Table 3.1 is associated with the distribution of cardiac output, and is discussed in more detail in Section 3.1.4.

The entire contents of Table 3.1 are stored in identical format in a file *element_data*, which is read by the program *networks.c* prior to execution. Since we are dealing with a network of these 28 elastic tubes connected into an arterial tree, connectivity of the elements must also be specified. Thus we now turn our attention to the selection of the parameters associated with the bifurcation boundary conditions.

3.1.3 Selection of Bifurcation Parameters

In the previous chapter the physical equations used to describe the bifurcation boundary conditions were discussed in detail. To fully describe the bifurcations, however, several parameters need to be specified. Firstly, connectivity is specified by identifying the parent branch and the daughter branches: currently, the model is capable of handling up to 4 daughter branches, although the code may be easily modified to accommodate additional branches. Each participating branch is assigned an entry/exit length x_1 ... x_N for the branches n=1 ... N, as shown in Figure 2.6, where only x_1 and x_2 are indicated. For each of the branches, a nominal entry/exit length of 0.5 cm was selected. Thus, the length of each element in Table 3.1 is adjusted to accomodate the added lengths: 0.5 cm are subtracted for elements of type "1" and "2" (those bounded by one bifurcation), while 1.0 cm is subtracted from elements of type "0" (those bounded by two bifurcations). The cross-sectional area of each participating branch is taken from the distal area specification (for the parent branch) and the proximal area specifications (for the daughter branches).

The contraction coefficients K_c for each daughter branch are specified as follows. The contraction coefficient is assumed to be a function of the angle between the departing daughter branch and its parent branch. Since the largest angle of departure in the human body is close to 90° (at the renal artery bifurcations), and the smallest angle is nearly 0°, a linear fit between the values for K_c between these two extremes should suffice. From studies of renal bifurcations (Yamaguchi et al., 1994), a value of K_c equal to approximately 0.5 can be estimated. At the other extreme, a departure angle of 0° would be expected to give a K_c close to 1.0. Using daughter branch departure angles estimated from anatomy atlases, the K_c for each daughter branch at each bifurcation can be estimated. These results are summarized in Table 3.2. Although this method is rather crude, it will be shown later in the next chapter that the accuracy of estimating the contraction coefficient has little effect on the quality of the data generated by the model.

Table 3.2. Branching angles for the bifurcations in the 28 element model.

bifurcation #	parent branch	daughter branch	branch angle (deg.)
1	ascending aorta	descending aorta	0
1	ascending aorta	brachiocephalic	45
1	ascending aorta	l carotid	45
1	ascending aorta	l subclavian	45
2	descending aorta	coeliac	66
3	descending aorta	sup. mesenteric	66
3	descending aorta	l renal	66
3	descending aorta	r renal	66
4	descending aorta	inf. mesenteric	66
4	descending aorta	l, r common iliac	38
4	descending aorta	l, r common iliac	38
5	l, r common iliac	l, r femoral	14
5	l, r common iliac	l, r profundus	14
6	l, r femoral	l, r ant. tibial	13
6	l, r femoral	l, r post. tibial	13
7	l, r ant. tibial	l, r peroneal	3
7	l, r ant. tibial	l, r ant. tibial	3
8	brachiocephalic	r brachial	8
8	brachiocephalic	r carotid	8
9	r brachial	r radial	6
9	r brachial	r ulnar	6
10	r common carotid	r ext. carotid	13
10	r common carotid	r int. carotid	13
11	l common carotid	l ext. carotid	13
11	l common carotid	l int. carotid	13
12	l brachial	l radial	6
12	l brachial	l ulnar	6

Table 3.3. Specifications for the bifurcations in the 28 element model.

bifurcation #	N-1	n=1	n=2	n=3	n=4	n=5	x1	x2	x3	x4	x5
1	4	1	2	8	11	12	0.5	0.5	0.5	0.5	0.5
2	2	2	3	21	21	-	0.5	0.5	0.5	0.5	-
3	4	3	22	22	23	4	0.5	0.5	0.5	0.5	0.5
4	3	4	5	5	24	-	0.5	0.5	0.5	0.5	-
5	2	5	6	25	-	-	0.5	0.5	0.5	-	-
6	2	6	7	26	-	-	0.5	0.5	0.5	-	-
7	2	7	27	28	-	-	0.5	0.5	0.5	-	-
8	2	8	9	10	-	-	0.5	0.5	0.5	-	-
9	2	9	13	14	-	-	0.5	0.5	0.5	-	-
10	2	10	15	16	-	-	0.5	0.5	0.5	-	-
11	2	11	17	18	-	-	0.5	0.5	0.5	-	-
12	2	12	19	20	-	-	0.5	0.5	0.5	-	-

bifurcation #	Kc, n=2	Kc, n=3	Kc, n=4	Kc, n=5	C, n=2	C, n=3	C, n=4	C, n=5
1	1	0.85	0.85	0.85	1.85	1.85	1.85	1.85
2	1	0.7	0.7	-	1.85	1.85	1.85	-
3	1	0.7	0.7	0.7	1.85	1.85	1.85	1.85
4	1	0.7	0.7	-	1.85	1.85	1.85	-
5	1	1	-	-	1.85	1.85	-	-
6	1	1	-	-	1.85	1.85	-	-
7	1	1	-	-	1.85	1.85	-	-
8	1	1	-	-	1.85	1.85	-	-
9	1	1	-	-	1.85	1.85	-	-
10	1	1	-	-	1.85	1.85	-	-
11	1	1	-	-	1.85	1.85	-	-
12	1	1	-	-	1.85	1.85	-	-

The entire data set used to specify the bifurcations for the 28 element model is given in Table 3.3 in the same format as the input file *bifurc_data*, which like *element_data* is read by *networks.c* for initialization of the necessary variables. Thus, the entire geometrical and material specifications of an individual arterial network can be specified using only these two input files, and without any alteration to *networks.c* itself. This will become important when one considers that multiple runs of the code must be accomplished with differing arterial properties for the parameter estimation library described in Chapter 4.

3.1.4 Distribution of Cardiac Output

Considerable difficulty was experienced in determining the distribution of blood flow to the various organ beds throughout the body. Local regulation of flow is extremely transient and dependent on a variety of factors, making it nearly impossible to accurately define a "standard" distribution of flow. Descriptions of the distribution of cardiac output can be found in the literature, and the results reported vary widely. For instance, Wade reports that under resting conditions in a "normal" subject, blood flow to the renal arteries is approximately 1100 ml/min, cerebral blood flow approximately 750 ml/min, and splanchnic blood flow approximately 1400 ml/min (Wade and Bishop, 1962). Another author reports a renal artery blood flow of 1250 ml/min, a cerebral blood flow also of 750 ml/min, and a splanchnic blood flow of 1250 ml/min (R. Kamm, personal communication). Due to this variability, combined with the transient nature of the distribution, many investigators have chosen to approximate the distribution of cardiac output in their cardiovascular models by using the flow rates listed above.

An alternative approach to estimating the distribution of cardiac output is based on the observation that the caliber of vessels is related to the flow rate they convey. As an evolutionary mechanism, blood vessels appear to adapt to their flow conditions and loads towards the minimization of some type of "cost function", which may be described as the energy cost to an organism of building and maintaining a system of vessels. This observation was formalized by Murray in 1926. Derivation of the so-called "Murray's Law" begins with the observation that in an optimally designed system of vessels transporting bulk flow of a Newtonian fluid, at bifurcations the radius of the parent branch r_1 to the nth power will equal the sum of the radii of all of the daughter branches ($r_2 \ldots r_N$), also to the nth power:

$$r_1^n = r_2^n + r_3^n + \ldots + r_N^n \qquad (3.1.2)$$

Estimates from experimental data show n to be approximately equal to 2.7 for the renal, mesenteric, and other human arterial trees, 3.2 for the coronary artery, and 2.33 for turbulent flow regimes (Kamiya et al., 1984).

Murray's Law can be derived formally if one defines a cost function based on the mechanical energy loss E_m for flow in a laminar tube (assuming a Poiseuille-like distribution) and the chemical energy cost E_c, proportional to its content volume. If the cost function is a sum of the two energy costs, then the total cost function CF may be written as:

$$CF = E_m + E_c = \frac{8\mu Q^2 L}{\pi r^4} + c\pi r^2 L \tag{3.1.3}$$

where the first term represents the Poiseuille losses for flow Q through a tube of length L, viscosity μ, and radius r, and the second term containing the coefficient c, which is the chemical energy cost per unit volume. To find the minimum of the cost function as a function of radius r, we solve for the case of $\partial CF/\partial r = 0$. Rearrangement of the terms yields:

$$Q/r^3 = (\pi/4)(c/\mu)^{1/2} = K = \text{constant} \tag{3.1.4}$$

which is a restatement of Murray's Law. If one also considers that the definition of the shear rate of blood on the wall surface for laminar flow is given by the expression:

$$\tau = \mu\dot{\gamma} = 4\mu Q/(\pi r^3) \tag{3.1.5}$$

then solving for Q/r^3 demonstrates that the term $\tau\pi/4\mu$ is also a constant by definition from equation (3.1.4). This implies that an extension of Murray's Law is that arterial wall shear is conserved regardless of artery caliber or flow. Indeed, several investigators have concluded from measurements that the shear at various locations throughout the arterial tree is preserved at a value close to 15 dyn/cm^2 (Giddens et al., 1993; Kamiya et al., 1984; Kassab and Fung, 1995; LaBarbera, 1990). It is worthy of note that a great deal of literature on the estimation of mean wall shear stress exists due to the strong correlation between wall shear and the development of atherosclerosis. Thus, Murray's Law has been suggested as a mechanism for minimizing endothelial cell layer damage, by closely maintaining wall shear to a tight, physiologic range. The local shear stress has also been measured in the dog, where the data are found to be surprisingly consistent with that of humans. Whitmore (Whitmore, 1968) reported values of shear in the dog aorta (1.0 cm dia.) of about 12 dyn/cm^2, 10.4 dyn/cm^2 for smaller arteries (0.3 cm dia.), and 18.6 dyn/cm^2 for the smallest arteries (about 0.1 cm in diameter). The values of mean wall

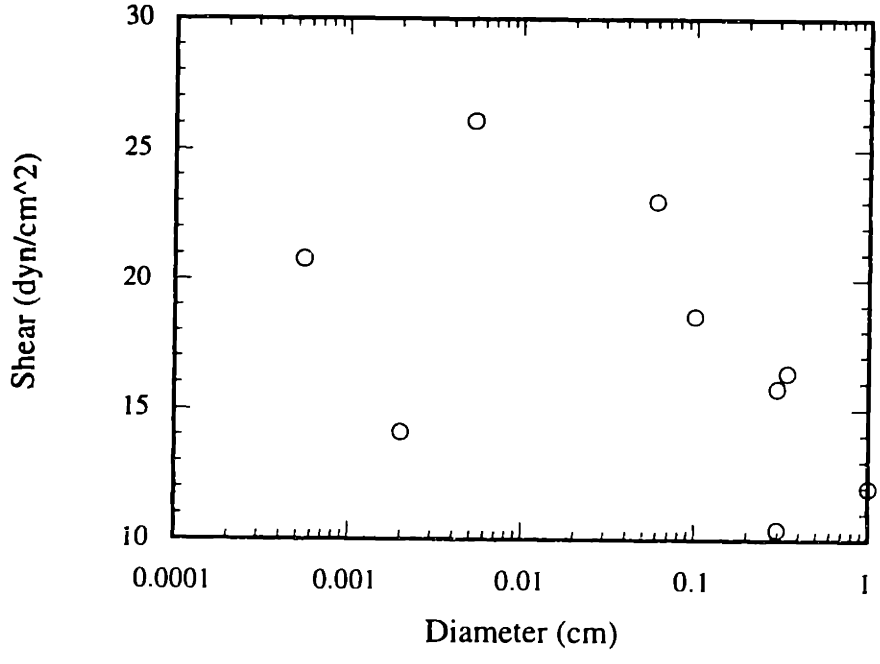

Figure 3.3. Scatter plot of mean wall shear stress versus arterial diameter measured by several investigators. Data compiled by Kamiya et al., 1984.

shear may also be expressed in terms of the cost function coefficient K by combining equations (3.1.4) and (3.1.5) to yield the new expression:

$$K = \frac{\pi\tau}{4\mu} = \frac{Q}{r^3} \tag{3.1.6}$$

Thus, assuming a blood viscosity of 0.04 cp, a mean wall shear τ of 15 dyn/cm^2 results in a nominal K value of 294.

It may be possible to draw some conclusions about the relationship between vessel caliber and mean wall shear stress. A plot of the available data on mean shear versus diameter is shown in Figure 3.3, that suggests a rather loose correlation between flowrate and artery diameter. For the purposes of this model we have lumped the mean wall shear stress into three categories that allow for realistic flowrates in various arteries to be calculated. For arteries of diameter 0.5 cm or larger no transmural wall leakage was allowed. This is justified by the observation that using values of K near the nominal value of 294 yields mean flowrates that are excessively high. Thus, the flowrates in these artery segments are obtained by summing the calculated flow in the tubes downstream from these larger arteries. For arteries from 0.3 cm to 0.5 cm in size, the nominal K value of 294 was used. For the smallest arteries of diameter less than 0.3 cm, K was set to 196, corresponding to a mean wall shear value of 10.0 dyn/cm^2. An exception to the rule was made in the case of the common carotid arteries, where transmural leakage was eliminated, as it yielded more realistic results than the case of K = 196. The resulting calculated mean flowrates for each of the elemental arteries are shown in Table 3.4, compared against corresponding available values from Wade for the major organ beds. The approximations obtained appear to be reasonable, and for the purposes of this model allow enough accuracy within the available known relationships between mean flow (and wall shear) and artery diameter. There exists a large discrepancy, however, between the calculated superior mesenteric flow and literature values. A correction may be made with a better estimation of the geometry, which may yield a diameter giving the correct flowrate from Murray's law.

Assuming that the specified K values correspond to *mean* wall shear values, which can be restated as the shear obtained by steady flow at a constant mean arterial pressure of 100 mm Hg,, the required flow can be calculated for each node within the network using equation (3.1.6). Hence, from the calculated required flow at all of the distal boundary nodes, the appropriate value of the terminal windkessel resistance R_s can be determined for each individual terminal element, assuming again a driving pressure of 100 mm Hg at the terminus. Likewise, within elements, any disparity in flowrates while moving

Table 3.4. A comparison of the distribution of cardiac output for the standard case with literature.

element #	artery name	calculated Q (ml/sec)	measured Q (ml/sec)	reference
1	ascending aorta	100.82	100	normal cardiac output
2	thoracic aorta	54.00		
3	abdominal aorta	42.36		
4	abdominal aorta	16.47	13	Pederson, 1992
5	common iliac	7.64	6.7	Moore, 1991
6	femoral artery	4.07		
7	anterior tibial artery	0.93		
8	brachiocephalic	22.43		
9	r brachial	12.56		
10	r common carotid	9.88	8.3	Bharadvaj, 1982
11	l common carotid	9.88	8.3	Bharadvaj, 1982
12	l brachial	14.51		
13	r radial	1.19		
14	r ulnar	2.74		
15	r external carotid	4.58	5.8	Perktold, 1990; Bharadvaj, 1982
16	r internal carotid	5.30	2.5	Perktold, 1990; Bharadvaj, 1982
17	l internal carotid	5.30	2.5	Perktold, 1990; Bharadvaj, 1982
18	l external carotid	4.58	5.8	Perktold, 1990; Bharadvaj, 1982
19	r radial	2.74		
20	r ulnar	1.19		
21	coeliac	11.63	9.8	Moore, 1991
22	renal	5.15	6.7	Moore, 1991
23	sup mesenteric	15.59	6.7	Moore, 1991
24	inf mesenteric	1.19	2.1	Moore, 1991
25	profundis	3.57		
26	post tibial	1.72		
27	ant tibial	0.29		
28	peroneal	0.64		

upstream resulting in a *positive* difference (i.e. when the inflow to a segment exceeds the outflow) is reflected in the leakage function coefficient, using equation (2.2.3). A *negative* difference is generally not possible, because of the geometric taper that is imposed resulting in an increasing inner radius as one moves upstream along each element.

We have outlined a method for determining the peripheral resistance, reflected by calculation of the individual values of R_s for each terminal windkessel. However, two additional parameters associated with the terminal windkessel are not yet accounted for. These include the entrance impedance Z_o and the windkessel compliance C_o. The entrance impedance can be regarded as an extension of its parent element, and thus a sharp discontinuity should not exist between the two; one can calculate the Z_o using the definition of impedance:

$$Z_o = \frac{\rho c}{A} \tag{3.1.7}$$

where c is the wavespeed and A is the cross-sectional area at the most distal node of the parent branch. This ensures that the major source of reflection at the terminal windkessel is derived from the outflow resistance R_s and compliance C_s as governed by equation (2.3.25) for the reflection coefficient Γ. A nominal value of 0.35 cm^5/dyn was used for C_s in every terminal windkessel, as it gave realistic pulse pressures for the nominal values of R_s specified for the standard case. It may appear that fixing the value of C_s in some ways constrains the dependence of Γ solely on R_s. However, one can make the assumption that C_s changes in proportion to the systemic arterial compliance, which is a function of the specified Young's modulus in equation (3.1.1). Thus, the relative change in E should always be accompanied by an inversely proportional change in C_s, where R_s is allowed to change independently.

3.1.5 The Lumped Parameter Model / Ventricular Elastances

The lumped parameter model of the cardiovascular system uses values previously specified by Davis and Sah in CVSIM, which in turn is drawn from many other sources. Thus, rather than repeat in detail the sources from which the parameters were obtained, the information is presented in Table 3.5, which is reproduced from Davis' thesis. For the most part, exact values for the lumped parameter element are not required, since we are primarily interested in the behavior of the arterial system, and thus the parameters that are directly coupled to it are those that should be chosen with care. As will be demonstrated in Chapter 4, there is enough reason to exclude the venous and pulmonary circulations completely, and thus the parameters that are of sole interest to the system identification

Table 3.5. Parameters for the lumped parameter model of the venous and pulmonary circulations.

Parameter	Symbol	Value
systemic venous compliance	C_v	0.075 cm^5/dyn
systemic venous resistance	R_v	13.3 dyn-sec/cm^5
right heart outflow resistance	R_{ro}	4.0 dyn-sec/cm^5
pulmonary artery compliance	C_{pa}	0.0032 cm^5/dyn
pulmonary artery resistance	R_{pa}	106.66 dyn-sec/cm^5
pulmonary venous compliance	C_{pv}	0.0063 cm^5/dyn
pulmonary venous resistance	R_{pv}	13.33 dyn-sec/cm^5

scheme are left ventricular parameters, peripheral resistance, and arterial compliance. Nonetheless, all of the parameter values are shown for future reference, since implementation of the baroreceptor reflex to study the transient behavior of the circulation requires the inclusion of the venous and pulmonary circulations.

For the standard case, the compliance of the arterial system can be calculated by pressurizing the entire system numerically to 90 mm Hg and 100 mm Hg, and measuring the volume difference in both the arterial segments and the terminal windkessels. For the standard case, a compliance of 0.002 cm^5/dyn was obtained. Comparison of this number with that stated in Table 3.5 shows that the arterial network is hypercompliant for the given set of geometry and material properties. However, it is unclear how the values of compliance in the table were obtained, and it is known that the compliance of the arterial system can change as the smooth muscle tone in the artery walls contracts or relaxes. The exact value of compliance will become less of an issue when parameter estimation is applied, since it is desirable for the model to be able to alter the systemic compliance for a given set of hemodynamic parameters which may still be within the "normal" range, yet approach those values measured in-vivo.

The ventricular elastances are equally important to the quality of the waves produced in the arterial tree, and the literature value that one can obtain for "normals" varies widely. Grossman et al. states a value for left ventricular peak elastance E_{max} of 4.0 mm Hg/ml in patients deemed to have normal left ventricular function (Yang, 1988); this yields a value of E_{max} of 5.3×10^3 dyn/cm^5. In contrast, Sah uses a value of 2.5 mm Hg/ml or 3.3×10^3 dyn/cm^5 for normal left ventricular E_{max}, which is acknowledged to be smaller than the normal measured value but gives realistic ranges of pressures in the lumped parameter model. We chose to use a value of 1.0×10^4 dyn/cm^5 for the peak left ventricular *isovolumic* elastance in the standard case, which gives a value of the apparent peak elastance equal to 7.9×10^3 dyn/cm^5, which is somewhat close to the value given by Grossman. This value was based on the need to generate reasonable values for peak arterial pressure. Note that it is difficult with the modified left ventricular equation (2.3.21) to precisely specify the actual peak elastance, since what is specified is the peak isovolumetric elastance for the function $E^*(t)$, rather than the elastances $E(t)$ that are measured in-vivo. As such, the specified peak value of E^* can be as much as double that of the apparent elastance calculated using equation (2.3.14). Thus, the isovolumic $E^*(t)$, approximated by a half sinusoid occupying a specified percentage of the total cycle (nominally 50% for the standard case) is scaled directly between the E_{min} and E_{max} for each respective ventricle.

The minimum elastance E_{min} for the left ventricle was taken to be 0.1 mm Hg/ml from Sah's model, who obtained the number from the range of left ventricle end-diastolic compliances complied by Mirsky (Mirsky, 1979). Additionally, Sah uses a value of diastolic elastance for the right ventricle equal to 0.05 mm Hg/ml, based on the observation that the left ventricular diastolic elastance is approximately double that of the left. Sah also chooses a peak right ventricle elastance equal to 0.833 mm Hg/ml, or 1.1×10^3 dyn/cm^5. The elastance values for the right heart are included in this thesis and in the numerical code of *networks.c* in order to provide a complete description of the lumped parameter model of the venous and pulmonary circulations. However, it will be shown later that the peak elastance for the left ventricle is of the most importance with respect to parameter estimation.

3.2 Validation of the Standard Case

Modeling of biological systems often puts one at a disadvantage in terms of validation compared to other systems in engineering that can be possibly modeled. The human body is a complex system, and therefore the definition of any one "normal" individual based on a single set of data is impossible. I am reminded of a recent article in Time magazine, in which 100 photographs of people of all races were digitally combined to create an image of the "average" human being, the resulting female looking rather like a tanned, possibly South American person with a hint of Asian mixed in somewhere. The "individual" in the picture in no way resembles me or any other people that I know, but I acquiesce that the person represents a prototypical human with two eyes, a nose, a mouth, ears, hair, a chin, and so forth The number of parameters required to describe something as seemingly basic as the human face is enormous, as any police artist who makes a living creating composite sketches of criminals can say. The diversity of the "normal" human circulatory system is just as extensive, and the definition of a "standard case" just as futile. However, we require this diversity in the sense that seemingly random combinations of parameter values are required to describe an individual, which makes the problem of parameter estimation of a biological system a more interesting and challenging pursuit.

Medicine, contrary to our discussion above, relies upon the definition of an "average" to make meaningful sense of data as applied to diagnosis. Statistics can identify a range of values for any given hemodynamic parameter or index within which the majority of the human population will fall: this can be defined as the range of "normal" or "healthy" values surrounding the mean obtained from a large enough

sampling. Individuals whose characteristics fall far from the mean in the tails of the bell curve are statistical anomalies, and thus belong to the realm of the "abnormal" or "sick". Thus, a wealth of data on mean values and expected deviations have been generated through the years by extracting measurements from a sample of many individuals representing the entire human population.

Thus, in defining the standard case and comparing the results to measured data, one must realize that exact matches are impossible to obtain, although close approximations can exist. Most cardiovascular measurements can only be obtained in a small number of individuals who are ill and therefore ethically can be subjected to the invasive measurement techniques (such as catheterization) required to obtain numbers of interest. Thus, "normal" data are not normal at all in most cases, but obtained in sick individuals who may be exhibiting "normal-like" behavior at the time of measurement. An even greater wealth of measurements have been taken in animals, particularly canines, but the data are really only useful for understanding the basic principles of the cardiovascular system and understandably cannot be applied directly to a model of the human circulation. Nonetheless, we refer to the salient features of the numerical model and how well it captures the *general* behavior of the cardiovascular system. The model validation may be divided up into specific phenomena that are of interest and have been well characterized in-vivo.

3.2.1 General Morphology of Pulse Waves

A wealth of data exist on the qualitative shapes of pressure and velocity in both the human and canine arterial trees. Validation of models of the circulation historically include comparison of waveforms at various locations generated by the model with the corresponding in-vivo tracings. An advantage of the distributed model is that at specific anatomical locations the distinctive pressure and velocity tracings can be compared against the literature for the identical corresponding locations. Data in-vivo have primarily been obtained using catheterization in humans, as well as through electromagnetic flowmetry in canines where surgical isolation of the arteries of interest allow for a large degree of accuracy in characterizing velocity waves. Information regarding velocity and flow are difficult to obtain in humans, as one is limited by the use of non-invasive and minimally invasive techniques to obtain hemodynamic data.

One particular study performed by is particularly valuable in that the qualitative change in the waveform as a function of distance from the aortic root can be easily observed (Mills et al., 1970). From the plot in Figure 1.4, one may note that the aortic root pressure and flow waves are a complex integration of the forward generated wave

derived from the left ventricle, and the reflected waves returning from the periphery which have been modified by the presence of taper and discrete reflection sites at bifurcations and the terminal arterioles. The reflected waves arrive at a delayed time which is a function of the finite wave speed in the arterial system. A more detailed discussion of wave reflection mechanics will be saved for Section 3.2.2. Nonetheless, it is worth noting that as one proceeds toward the periphery from the aortic root, the forward wave becomes modified by the effects of taper and damping, and also becomes less separated from the returning reflected waves as the distance from the sites of reflection diminish. The overall effect is, qualitatively speaking, an increase in the peak amplitude of the leading pressure wave, concomitant with a decrease in the forward peak of the velocity (or flow) wave. Additionally, there is a widening of the period of flow reversal in the flow tracing accompanied by a narrowing of the forward peak of the velocity wave, which is a combined effect of both the reflected waves (which return inverted in the velocity component) and a compliance effect, where overdistended arteries empty their volume toward the path of least resistance. In general this path is upstream toward the heart, especially when peripheral resistance is high. The equivalent computed data from the model corresponding to that of Mills are shown in Figure 3.5. Qualitatively, the tracings agree very well in shape and magnitude, although much of the detail in the in-vivo measurements are masked with high frequency noise which may result from the measurement technique.

The behavior of the pressure and flowrate waves as a function of distance from the heart is more clearly demonstrated in Figure 3.6, which shows this effect. Figure 3.7 consists of similar data obtained at the corresponding locations in the numerical distributed model. One notes a generally good agreement between the measured human data and the calculated waves from the standard case. Thus, it appears that the model contains enough of the physics to allow for the gradual changes in the arterial waves as they propagate downstream from the aortic root.

Many explanations can be given, however, for the possible disparities that may exist between the computed and measured data. First, it is difficult to assess the contribution of the impedance mismatching at the bifurcations which may tend to generate reflected waves that are either inverted or upright, and thus would be expected to increase or diminish the measured peak pressure amplitude upstream of the bifurcation. Furthermore, it is also difficult to account for the contribution of numerous small side branches that are neglected in the model, but exist in-vivo and hence may contribute to the steepening of the wave front as it moves peripherally. Nonetheless, it may be expected that the waveforms will differ somewhat from those measured in a specific

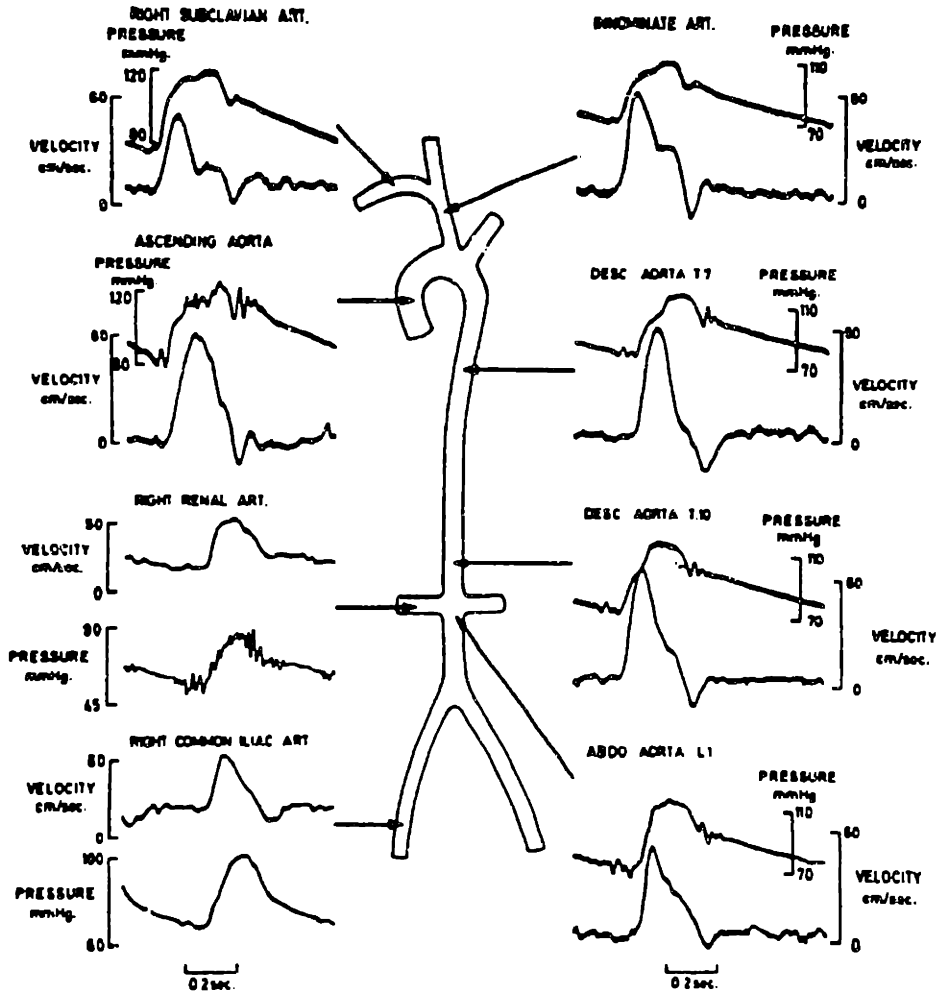

Figure 3.4. Simultaneous pressure and blood velocity patterns recorded at points in the systemic circulation. From Mills et al., 1970.

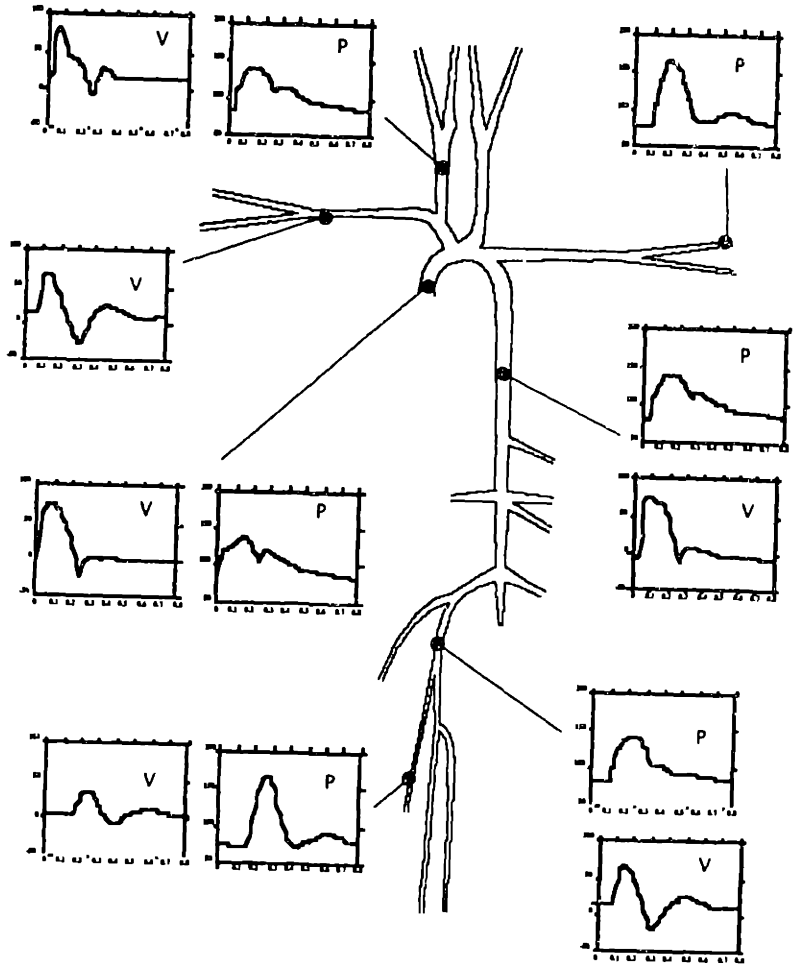

Figure 3.5. Simultaneous pressure and blood velocity patterns at points in the systemic circulation from the standard case.

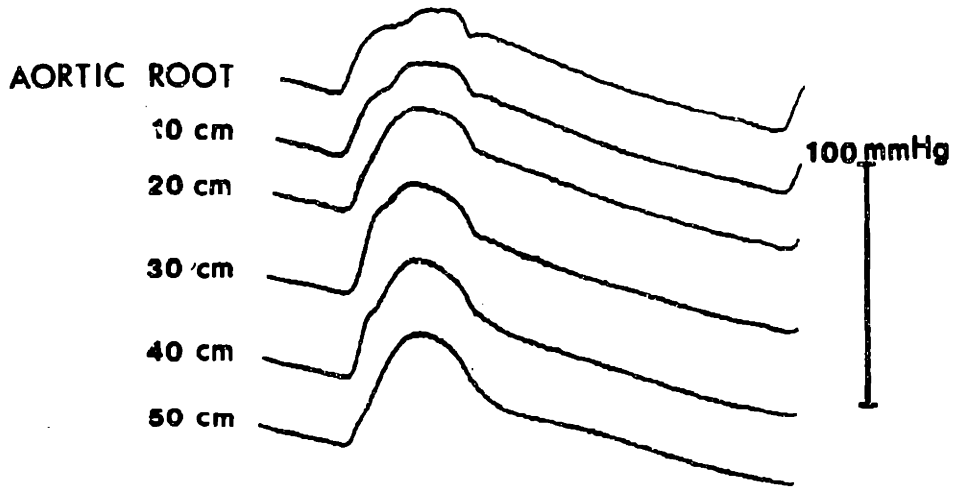

Figure 3.6. Pressure recordings along the aorta in man, proceeding from proximal to distal transducers. From Latham, 1987.

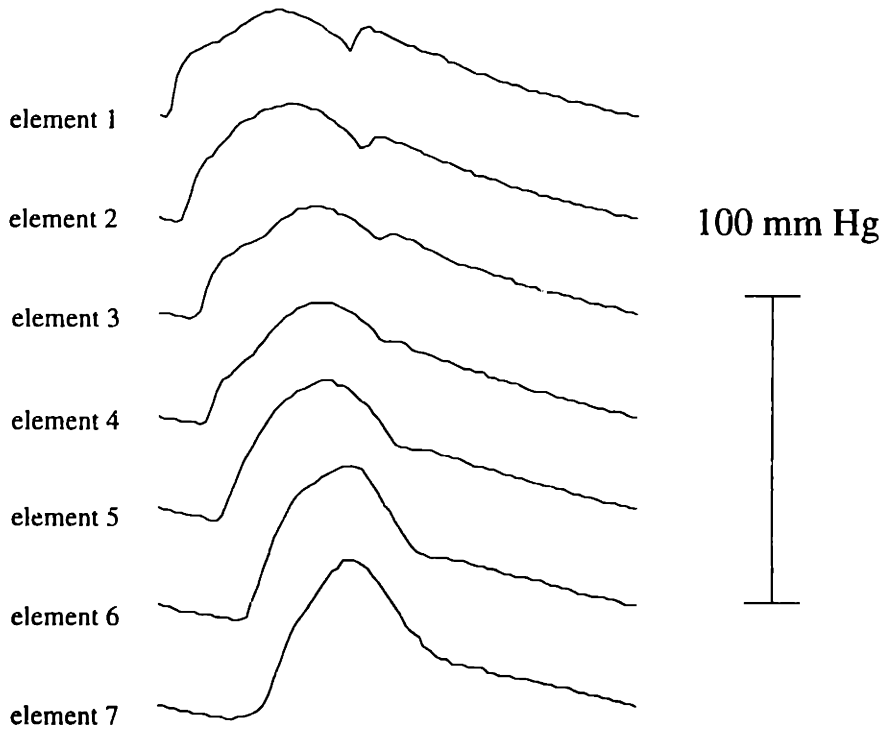

Figure 3.7. Computed pressure tracings along the aorta obtained from the standard case, proceeding from proximal to distal elements 1-7.

individual due to the large amount of variability seen between individuals within the subset of "normal".

The waveforms generated by the model may also be compared against normal data obtained by the author during the clinical study, which is described in more detail in Chapter 5. Velocity and pressure waves were recorded at many locations throughout the body in both normals and heart failure patients, and the corresponding traces generated by the model may be compared with the measured in-vivo tracings in order to further qualitatively validate the numerical model. This demonstrates the ability of the model to capture the main qualitative features of the velocity and pressure waves. Figures 3.8 through 3.12 show the model outputs for carotid artery velocity, carotid pressure, brachial velocity, radial pressure, and tibial artery velocity as a function of time, respectively. Several plots of the corresponding normal in-vivo measurements are placed adjacent to the numerical estimation in each plot for comparison. It is readily apparent from the figures that the model is capable of generating very realistic waveforms.

The carotid artery velocity is of note, since the secondary peak late in systole is a well-known feature in-vivo, and can be clearly seen in the provided normal measurements. This second peak may be accounted for by the returning inverted velocity wave from the terminal arterioles in the cerebral circulation, which essentially "gouges" out the downward side of the forward velocity wave. An additional carotid flowrate tracing from literature is shown in Figure 3.13, which also demonstrates the distinctive shape of the carotid velocity curve. Additionally, the calculated brachial velocity wave is also fairly accurate in its ability to capture the region of flow reversal in late systole/early diastole. The comparison, however, is somewhat less robust when one looks closely at the radial pressure pulse, where the normal in-vivo pressure wave is frequently triphasic in nature. The numerical simulation for the standard case appears to have difficulty in reproducing the well-defined secondary peak or inflection, which is attributed to the reflected wave returning upright from reflection sites remote from the arms. A numerical model developed by Karamanoglu and O'Rourke (Karamanoglu et al., 1995) manages to capture the secondary peak, and significant differences exist between the components of their model and those contained within this thesis. It is worthwhile to reflect that the present numerical model with its defined standard case may have significant shortcomings when it attempts to accurately represent the radial pulse pressure. This may become problematic when attempting to perform parameter estimation using the measured radial pressure pulse from patients.

Simultaneously, one may again note from Figures 3.8 through 3.12 the large amount of qualitative variability between individual in-vivo tracings representative of the range

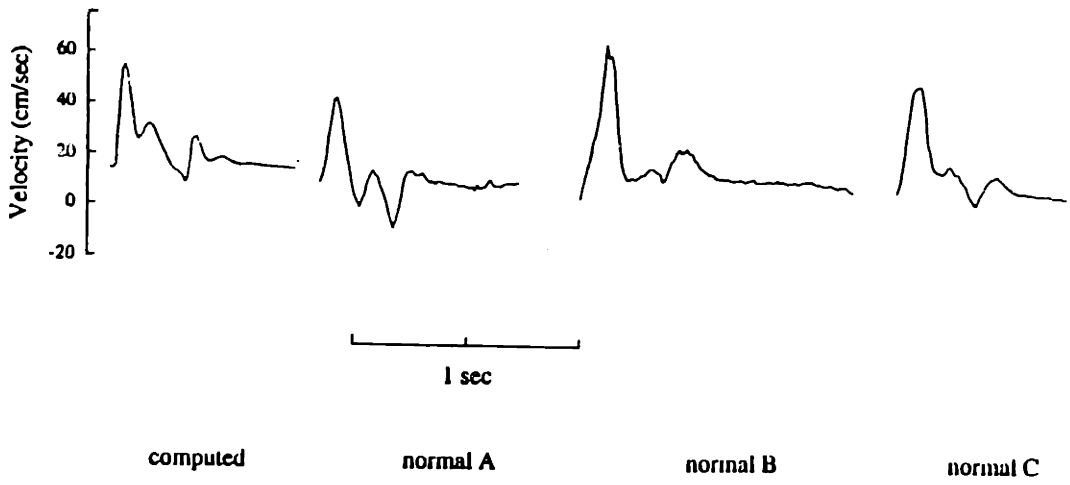

Figure 3.8. Computed carotid velocity tracing from the standard case (leftmost tracing) compared against four normal in-vivo measurements.

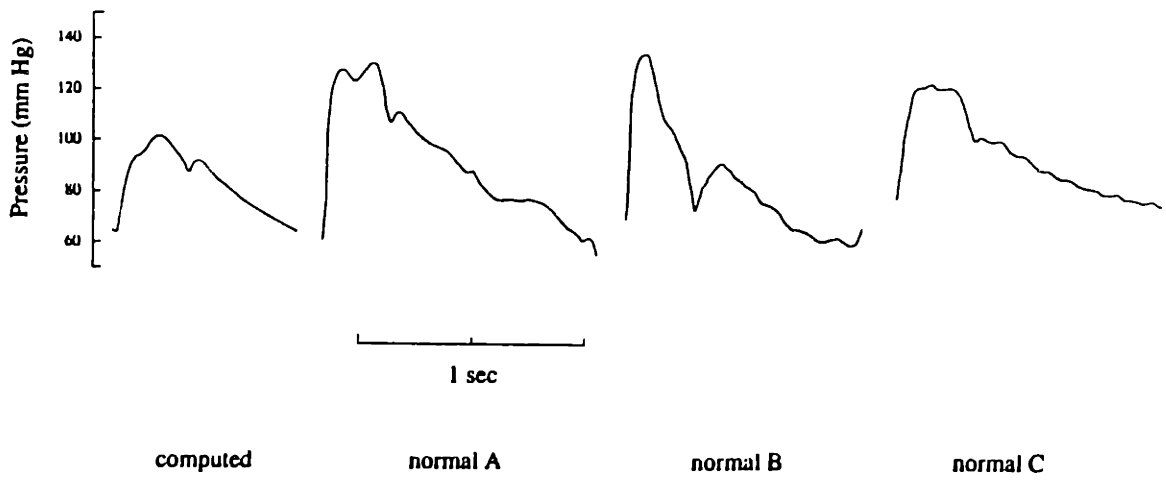

Figure 3.9. Computed carotid pressure tracing from the standard case (leftmost tracing) compared against normal in-vivo measurements.

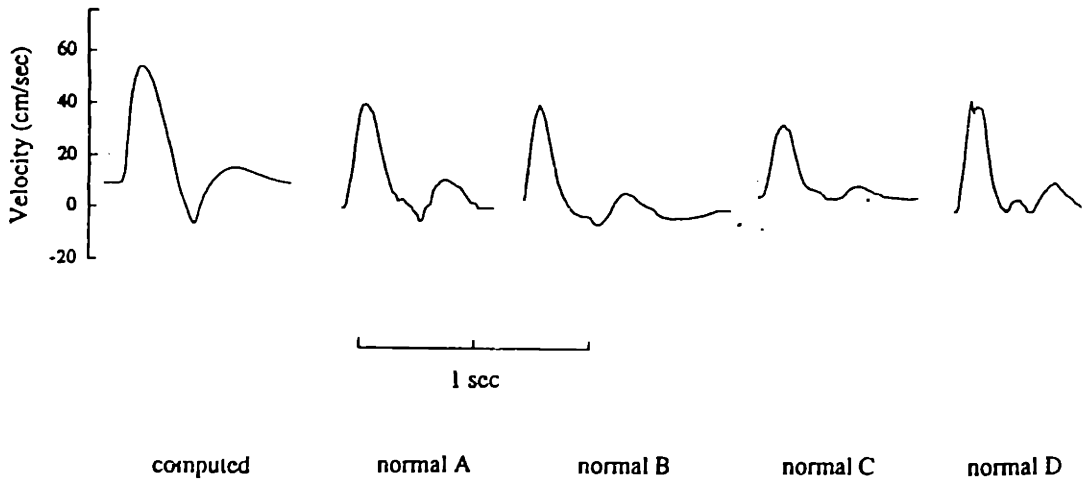

Figure 3.10. Computed brachial velocity tracing from the standard case (leftmost tracing) compared against five normal in-vivo measurements.

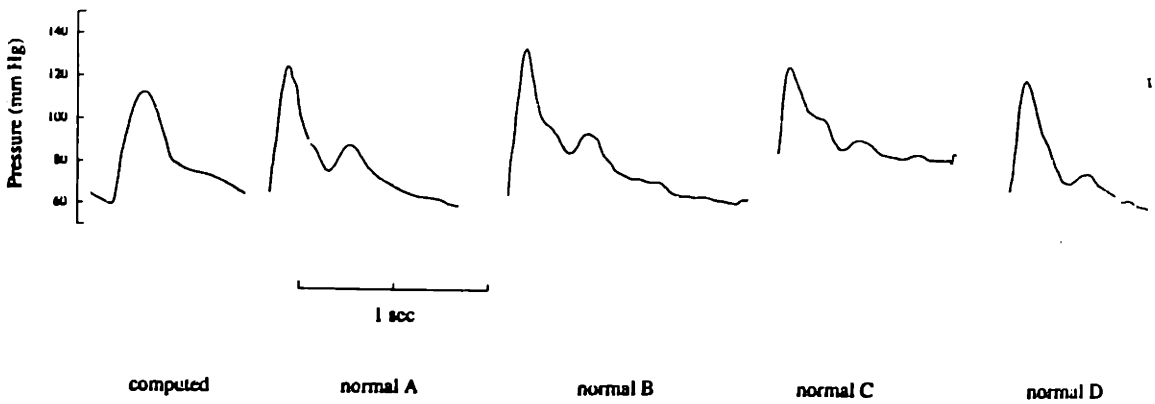

Figure 3.11. Computed radial pressure tracing from the standard case (leftmost tracing) compared against normal in-vivo measurements.

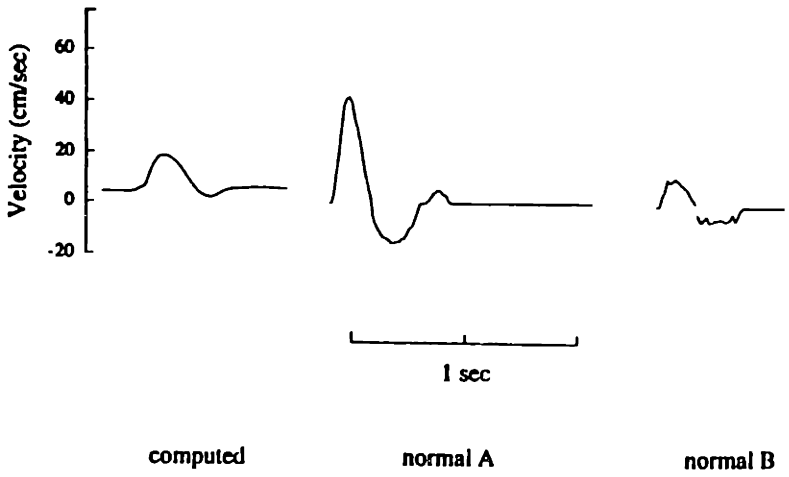

Figure 3.12. Computed tibial velocity tracing from the standard case (leftmost tracing) compared against four normal in-vivo measurements.

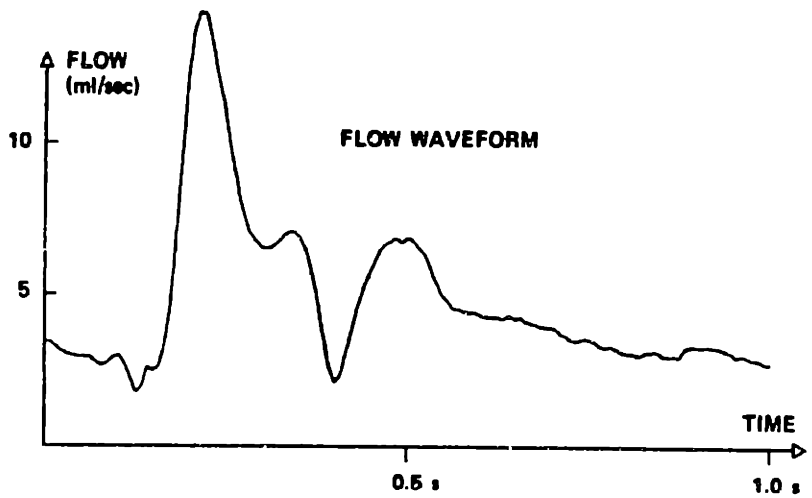

Figure 3.13. Carotid flow tracing measured in a normal individual. From Bharadvaj et al., 1982.

of waves that may be obtained from "normal" individuals. As we shall see in the next chapter, alterations in the set of parameters that define the standard case result in waveforms that are significantly different than those shown here, thus mimicking this variability seen where individuals may be expected to posses different measurable hemodynamic parameters. This large variability is necessary in order for the model to produce the wide range of outputs corresponding to the many different states (diseased or otherwise) of the human cardiovascular system.

3.2.2 Wave Transmission and Reflection

The effect of gradual taper is to create a steepening of the wave front, and is a similar effect to that obtained in wave propagation down a narrowing channel. In the case of arterial taper, the effect is a function of both the decrease in cross-sectional area and the increase in wavespeed with increasing distance from the heart. An analogy that is often used to describe this behavior is that of a water wave approaching a beach, where the depth of the water decreases as the wave moves shorewards. This creates the well-known peaking and cresting of the approaching wave that is generated by the interaction of the wave's energy with the ocean bottom. Lighthill presents a simple analysis of pressure waves traveling down a tube with gradually changing impedance (Lighthill, 1978). The impedance of an Y artery is defined as the ratio:

$$Y = \frac{A}{\rho c} \tag{3.2.1}$$

where the inverse of impedance is the admittance Z. A discrete change in the impedance of a tube results in the generation of a reflected wave, whose energy is described by the ratio between the impedance immediately upstream and downstream of the continuity:

$$\Gamma = \frac{Y_1 - Y_2}{Y_1 + Y_2} \tag{3.2.2}$$

This is shown in Figure 3.14 for the case of a tube with a discrete increase in impedance in the downstream direction. A tapered tube can be regarded as a series of these finite changes in the impedance each over a small stepsize, and is close to the actual behavior of the numerical model since each nodal position is separated by a finite distance dx, with abrupt changes in cross-sectional area and wavespeed as one proceeds downstream from node to node. However, for an actual tube, the reflection coefficient Γ and hence the ratio of amplitudes of the incident and reflected pressure waves can be calculated by summing the contribution of the individual steps as calculated in expression (3.2.2) by taking the limit of the stepsizes to zero. This approximation by taking the limit is shown

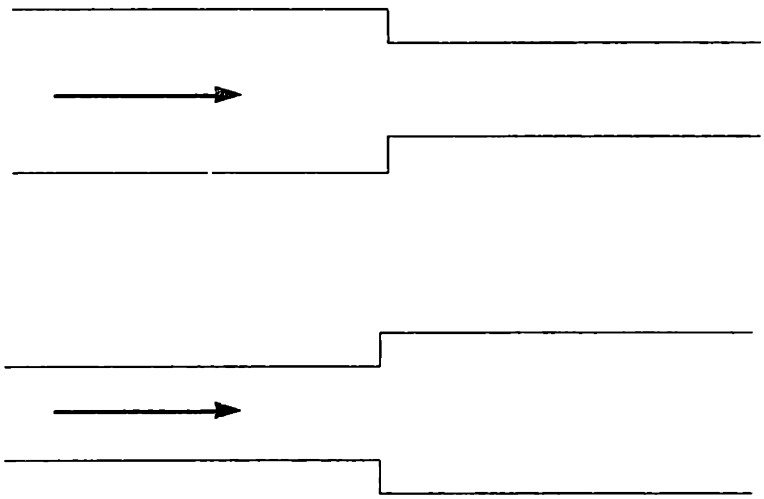

Figure 3.14. An approaching wave, indicated by the arrow, reaching a discontinuity in increasing (top) or decreasing (bottom) impedance.

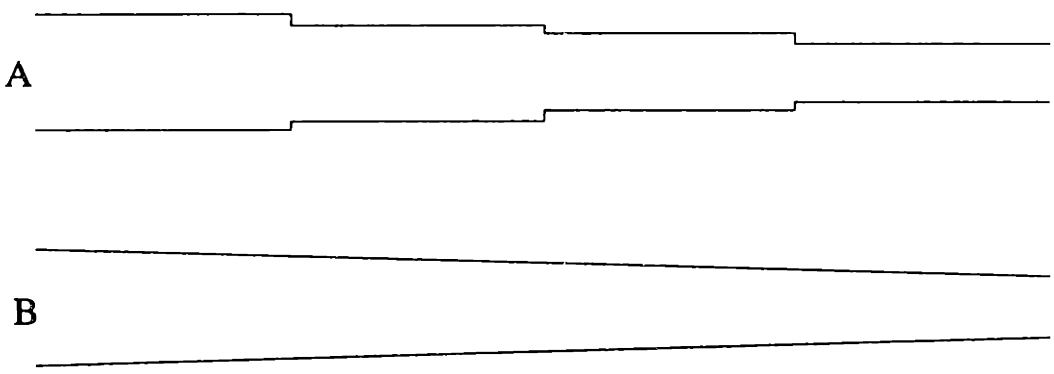

Figure 3.15. The approximation of a tapered tube B by a discrete equivalent A.

graphically in Figure 3.15. Thus, for a wave traveling down a tapered tube, the resulting increase in pressure wave amplitude with increasing length x moving downstream is given by:

$$P_e = [Y(x) / Y(0)]^{-\frac{1}{4}} f\left(t - \int_0^x c^{-1} dx\right) \tag{3.2.3}$$

and for a wave traveling in the opposite direction (negative x direction):

$$P_e = [Y(x) / Y(0)]^{-\frac{1}{4}} f\left(t + \int_0^x c^{-1} dx\right) \tag{3.2.4}$$

These equations were derived by Lighthill as an approximation to the increase in the pressure amplitude over a distance from $x = 0$ to a given position at some location x downstream of the wave source.

A simple test can be performed on the model by producing a small amplitude wave in a single tube with properties similar to that of the human aorta *without* any sources of damping. One may calculate the peak pressure at a distance $x = 9$ cm distally from the tube entrance using equation (3.2.3). Given that the wavespeed $c_o = 466.3$ cm/sec and area $A = 6.04$ cm^2 at $x = 0$ cm, and that the wavespeed $c_o = 468.0$ cm/sec and area $A = 5.56$ cm^2 at $x = 9$ cm, a value for the change in amplitude may be determined. Refer to Figure 3.16. The test wave introduced into the system (at a steady state pressure of 100 mm Hg) was a small step function of amplitude 1 mm Hg imposed at time zero. The resulting wave measured at the station x = 9 cm is larger in amplitude following the cessation of numerical ringing that accompanies the shock front. The calculated amplitude is 101.049 mm Hg, which agrees with the calculated amplitude of 100 mm Hg + 1 mm Hg x 1.44 = 101.44 mm Hg obtained using the analysis above. Thus, the numerical model appears to correctly capture the effects of gradual changes in the tube properties as a function of distance.

Additionally, one may note from Figure 3.16 that the pressure wave at station x = 9 cm is delayed from the imposed wave at station $x = 0$ cm by 0.02 seconds. Evaluation of the integral term of equation (3.2.3), representing the finite delay in time required for transmission of the wave, yields a value of 0.019 seconds which is also in good agreement with the delay obtained from the simulation. This demonstrates that the model is capturing the effects of finite wave propagation speeds which affects the timing of both the forward and reflected waves in the arterial system. The morphology of both the pressure and flow waves at any arbitrary point in the arterial system will be a function of the intersection between forward and reverse wave components, and is therefore also a function of finite wave velocities. Additionally, from Figure 3.6 of the pressure waves as

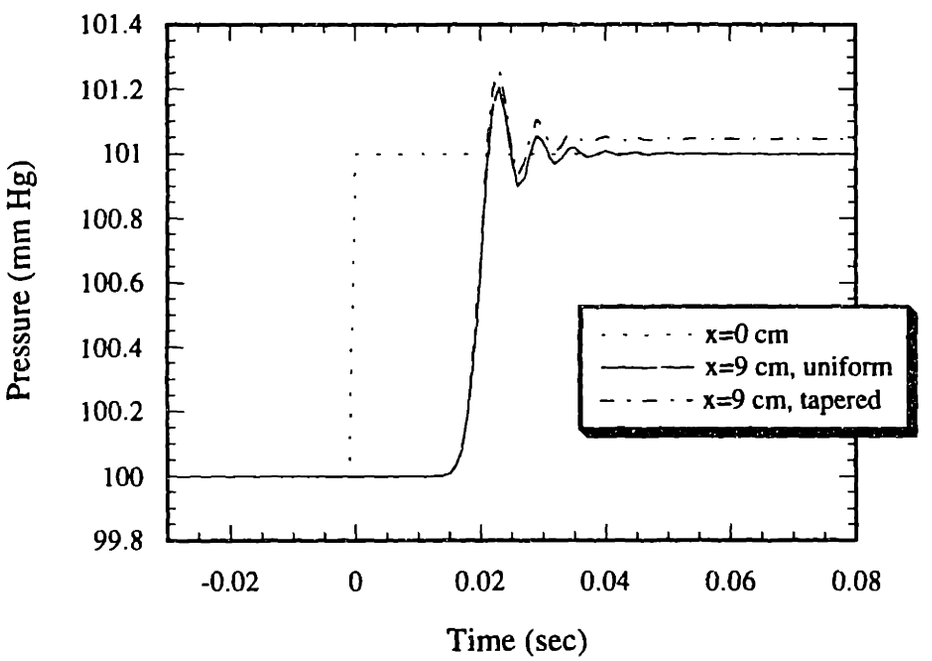

Figure 3.16. The effect of taper on the propagation of a step function down a single elastic-walled tube.

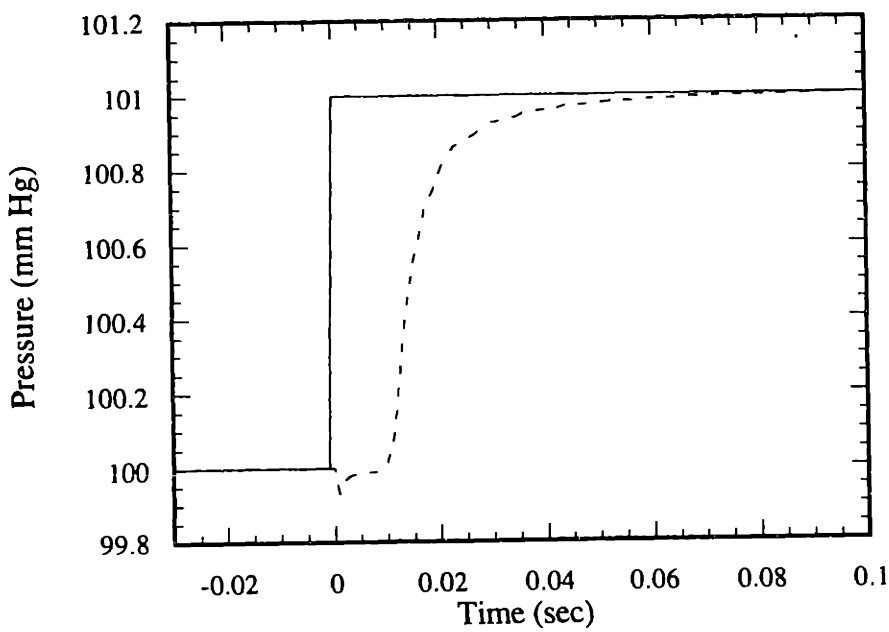

Figure 3.17. The effect of damping on the propagation of a step wave.

a function of distance from the heart one may note that at each successive element, the foot of the rising pressure peak is delayed as the increasing element number is related to increasing distance from the heart.

An additional benefit of this small-amplitude wave study is the opportunity to observe the effect of damping by adding back the two sources of energy loss and repeating the experiment. The results are shown in Figure 3.17, and as can be easily seen both transient wall shear and wall viscoelasticity act to dampen the forward edge of the shock wave. Additionally, the numerical ringing observed on the leading edge of the undamped wave is not present in the damped case, which aids in the prevention of forming shock-like transitions both physiologically and numerically.

As mentioned above, the pressure and flow waves measured at any arbitrary location in the arterial tree is a complex milieu of the forward wave and the many reflected waves returning from numerous reflection sites in the arterial tree. Virtually any alteration in structure may be considered a potential source of wave reflection. Impedance mismatching at bifurcations, for one, constitutes a major source of reflection. If one considers the case of a parent branch bifurcating into several daughter branches, then the reflection coefficient for the bifurcation may be given by the expression:

$$\Gamma = \frac{P_r}{P_i} = \frac{Y_1 - Y_2 - \ldots - Y_N}{Y_1 + Y_2 + \ldots + Y_N} \tag{3.2.6}$$

where the admittances Y_1 through Y_N for the branches $1..N$ are calculated using equation (3.2.1).

An additional and more important source of reflection is due to the high impedance of the arteriolar bed. Indeed, it is the general consensus that this region constitutes the largest source of reflections seen physiologically. Arterioles, as mentioned in Section 2.3.3, are responsible for regulation of blood flow into capillary beds, and therefore the presence of large amounts of active smooth muscle accounts for the comparatively larger stiffness and smaller cross-sectional areas than found in the smaller arteries immediately upstream. Under pathological conditions such as aortic stenosis, however, these peripheral reflection sites may be overshadowed by the effects of the discrete reflection site which represents a large discontinuity in input impedance. For the purposes of this model, however, we ignore the effects of local sudden changes in impedance and focus more on global changes in reflections as a result of altering peripheral resistance.

The summation of the many discrete sources of reflection are responsible for the characteristic shape of the reflected waves observed in-vivo. In general, as the wave travels from the heart outwards to the periphery, it encounters an overall increase in the

impedance with increasing distance, which results in the production of reflected pressure waves which return in phase (upright) from the periphery back towards the heart (Figure 3.18). Velocity waves, on the other hand, are reflected 180° out of phase (inverted) when they encounter an increase in impedance. In both cases of pressure and velocity, the forward wave leaving the heart is identical in shape but scaled appropriately in amplitude for the linear case, but may be somewhat modified by the nonlinearities that actually exist. Likewise, the total reflected wave that returns to the heart, after a delay representing the time required to make the round trip journey from the periphery, is also identical in shape for both pressure and velocity. As expected the pressure wave returns scaled with a positive phase and thus adds to the amplitude of the forward wave. The velocity wave, meanwhile, returns inverted and scaled, thus subtracting from the amplitude of the forward wave in the final result (Figure 3.19).

Numerous studies have been performed to obtain accurate measurements of the pressure and flowrate in the aortic root in order to study the conditions which alter the shape and amplitude of the reflected pressure wave. For instance, a decrease in the reflected wave amplitude for both pressure and flow is observed with vasodilation (O'Rourke, 1992). This result is consistent with the notion that peripheral arterioles relax during vasodilation, thus reducing the impedance mismatch between the small arteries and the terminal arterioles. Similarly, in congestive heart failure where the peripheral resistance is inappropriately raised, the reflected wave is larger in amplitude than normal, thus reflecting the opposite effect of constricting arterioles. Figure 3.20 shows a measured human aortic root pressure and flow wave decomposed into forward and reverse waves obtained from Laskey and Kussmaul in 1987. One notes that the behavior exhibited by this in-vivo example is consistent with the explanation of wave reflection from the periphery given above. For comparison purposes, the corresponding calculated pressure and flow waves from the model are decomposed similarly into its forward and reverse components using the time-domain decomposition developed by Li (Li, 1986). Li begins with the definition of impedance for the arterial tree:

$$Z_o = \frac{P_f}{Q_f} \tag{3.2.7}$$

where P_f and Q_f are the forward traveling components of the wave. The measured pressure itself is the linear addition of the forward and reflected waves given by the expression:

$$P = P_f + P_r \tag{3.2.8}$$

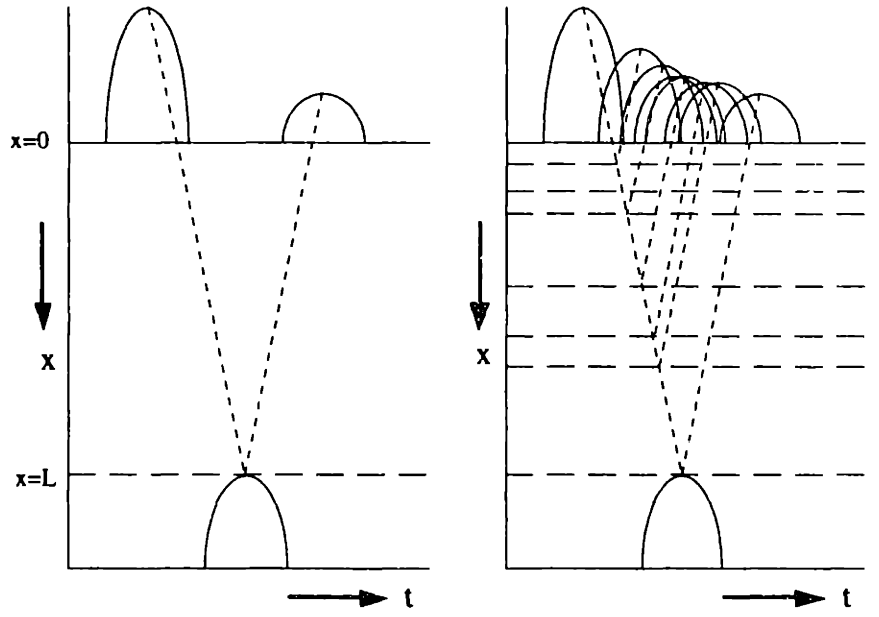

Figure 3.18. The behavior of pressure wave reflections. The wave originates at x=0 and travels downstream with finite speed, reflected in a characteristic line whose slope is equal to the wavespeed. Upon reflection from a low admittance boundary, the wave returns in phase at x=0 after a delay. Multiple reflection sites lead to multiple waves overlapping at x=0.

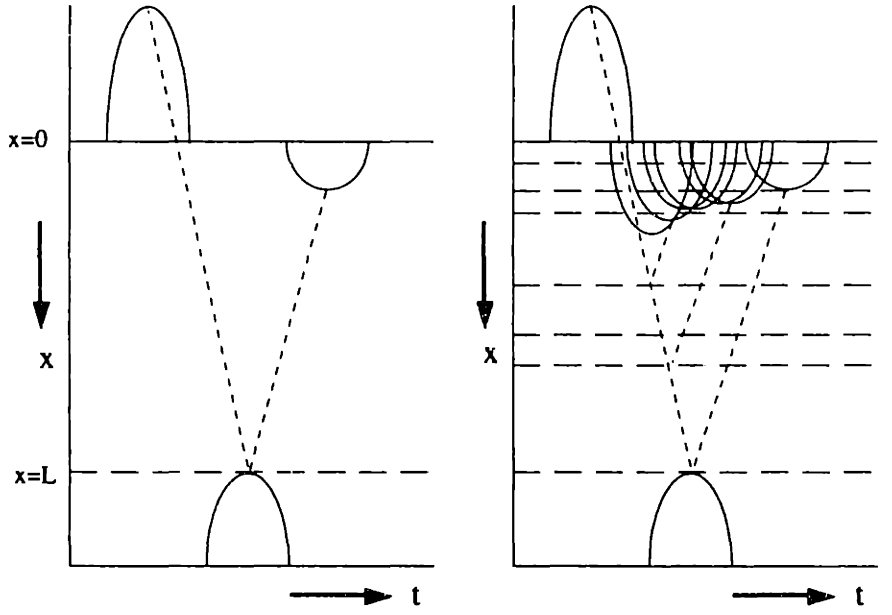

Figure 3.19. The behavior of velocity wave reflections. The behavior of velocity waves is similar to pressure waves: note that the reflected waves arriving at x=0 are 180° out of phase from the incident wave.

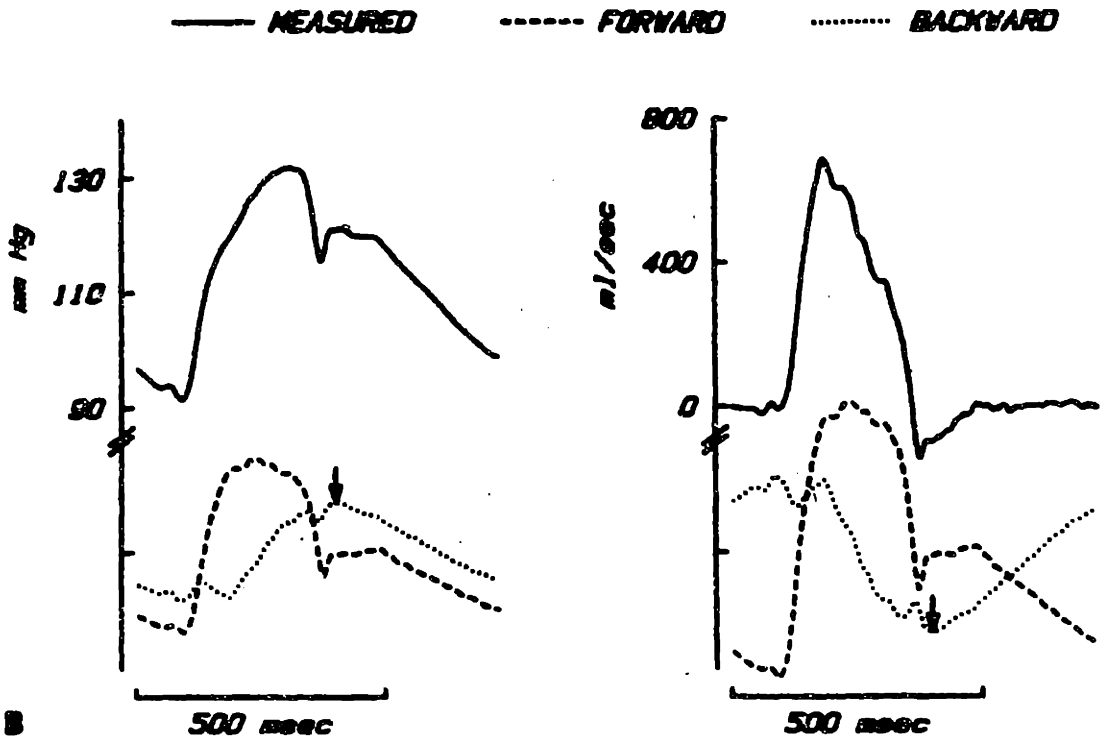

Figure 3.20. Aortic root pressure and flow waves measured in the human, decomposed in the time domain into the forward and reflected (backward) waves. From Laskey and Kussmaul, 1987.

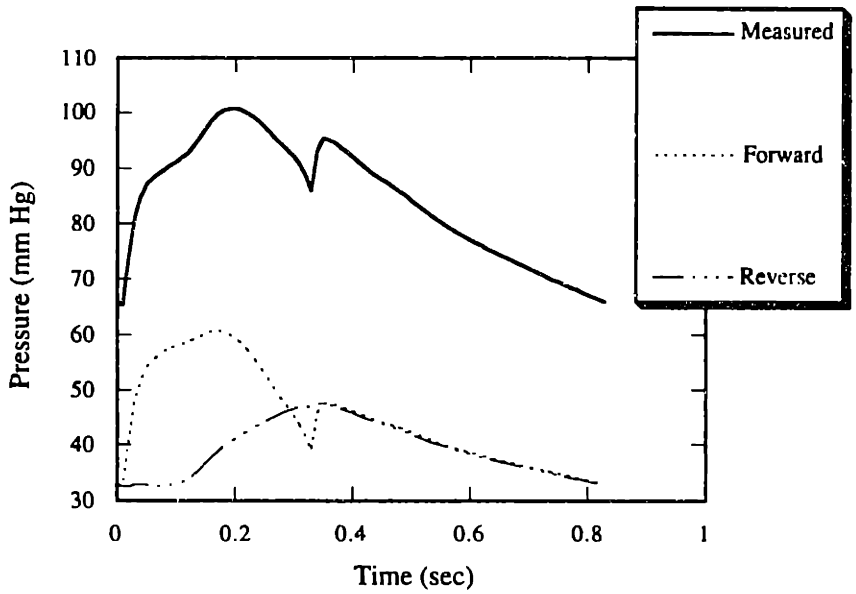

Figure 3.21. Calculated aortic root pressure decomposed in the time domain into forward and reverse components.

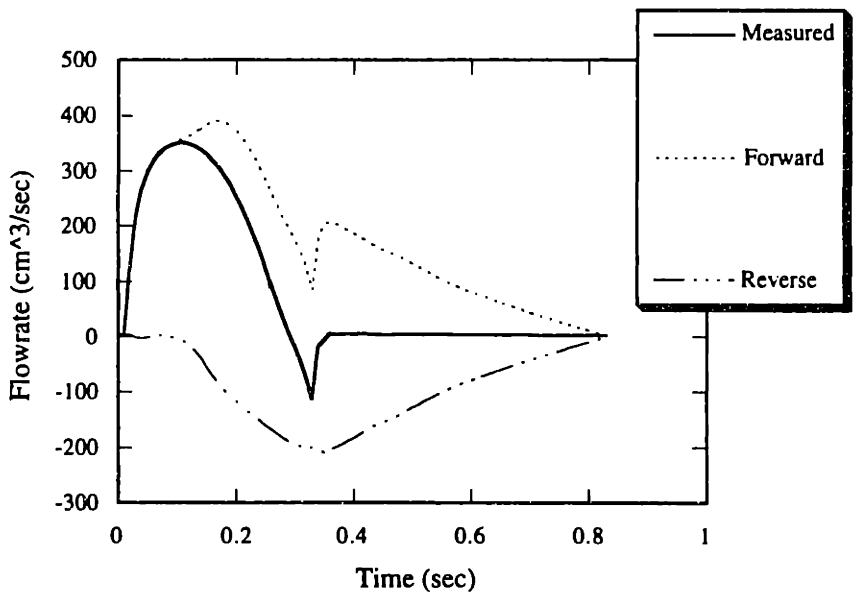

Figure 3.22. Calculated aortic root flowrate decomposed in the time domain into forward and reverse components.

Likewise the measured flowrate is also the linear addition of its forward and reverse components:

$$Q = Q_f + Q_r \tag{3.2.9}$$

By definition, the reflection coefficient is the ratio between the amplitude of the reflected and the forward wave:

$$\Gamma = \frac{P_r}{P_f} \tag{3.2.10}$$

After manipulation of the above expressions, Li arrives at the following relationship for the forward pressure wave:

$$P_f = \frac{1}{2}(P + QZ_o) \tag{3.2.11}$$

Li then assumes that expression (3.2.7) can be approximated by using the change in pressure ΔP and the change in flowrate ΔQ from the upstroke during early systole, since the reflected waves have not yet returned from the periphery:

$$Z_o = \frac{\Delta P}{\Delta Q} \tag{3.2.12}$$

Thus, this approximation for Z_o is inserted into expression (3.2.11) to solve for P_f, and (3.2.8) can be used to solve for P_r. Using the remaining equations, Q_f and Q_r can also be computed algebraically.

The calculated forward and reverse waves are qualitatively identical to those obtained from the human data, indicating that the model is indeed capturing the effect of wave propagation and reflection from the peripheral reflection sites, which are predominantly the terminal windkessels. These results are shown in Figure 3.21 and 3.22, and were obtained by applying equations (3.2.7) through (3.2.12) to the computed aortic root pressure and flowrate for the standard case.

3.2.3 Characterization of the Input Impedance

Historically, characterization of the mechanical properties of the arterial system has involved treating the entire system as a black box for which a frequency analysis may be applied. This method evokes a parallel to control theory in which a transfer function of a black box system may be derived by performing a Bode analysis based on the frequency response of the system. Likewise, if the arterial system is treated as a hydraulic system for which simple differential equations may be written (i.e. the windkessel

approximation), then the frequency response of the arterial system may be expected to give insight into the parameters associated with impedance and capacitance. The arterial system is normally dynamically driven by a complex periodic waveform in-vivo, and thus measurement of the pressure and flow waves at any location in the arterial tree will provide information regarding the input impedance for that particular region downstream from the point of measurement. The input impedance may be defined as the amplitude modulus, which is simply the ratio between the pressure amplitude and the flowrate amplitude $Z = |P|/|Q|$, as a function of frequency, where the amplitudes are determined from a Fourier frequency decomposition of the measure pressure and flowrate signals recorded in the same location (generally the ascending aorta). The impedance modulus is accompanied by the impedance phase, which is the phase difference between the pressure and flow amplitudes $\phi_{lag} = \phi(P) - \phi(Q)$ also as a function of frequency. Hence, a positive value of impedance phase corresponds to pressure leading flow.

Numerous studies have been performed to characterize the input impedance of various vessels in both humans and canines. Of particular note is the study of Nichols, who recorded aortic blood flow using electromagnetic catheter-tip velocimeters in patients undergoing cardiac catheterization (Nichols et al., 1977). Pressure was simultaneously recorded through fluid-filled center of the velocimetry catheter. The input impedance profile for 5 normal subjects are shown in Figure 3.23. The top panel of the plot shows how the modulus falls from its initial value, equal to the mean aortic pressure divided by the mean arterial flow (or the peripheral resistance) to a minimum at 4 Hz and rises again thereafter. The impedance phase shown in the lower plot reaches a minimum negative value, indicating that flow is leading pressure, and then crosses over to become positive at approximately 3 Hz.

Additional data from O'Rourke has been provided in Figure 3.24 as a contrast to that of Nichols. The impedance profiles shown here are qualitatively similar to those measured by Nichols, and included in the plots are the result of the multi-branched model of the arterial system developed by Avolio, which was previously discussed in the beginning of Chapter 2.. The same identical behavior at lower frequencies can seen, where the modulus drops initially from the value for peripheral resistance at 0 Hz to a minimum value near 4 Hz, and the phase lag is also initially negative until it crosses the axis somewhere near 6 Hz. At higher frequencies, however, there appears to be a greater amount of variability such that any mean impedance profile calculated from the individual tracing would be expected to carry relatively large error bars.

Using the definition of input impedance and phase lag, the calculated aortic pressure and flow waves from the standard case can be decomposed to give an impedance profile

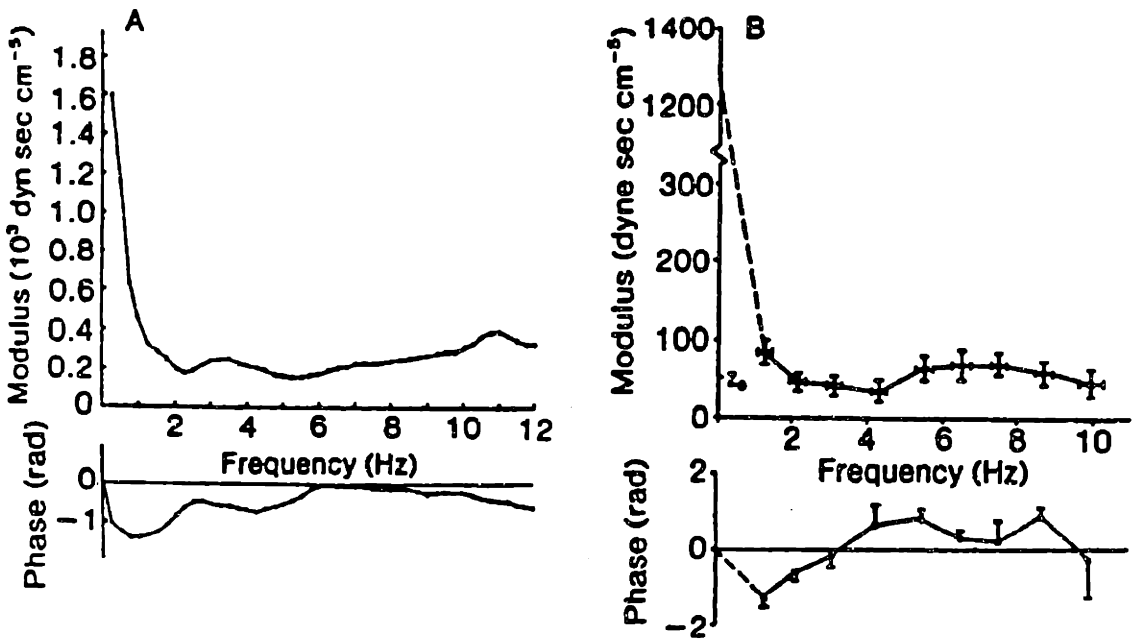

Figure 3.23. The input impedance of the human arterial system measured by Nichols et al., 1977.

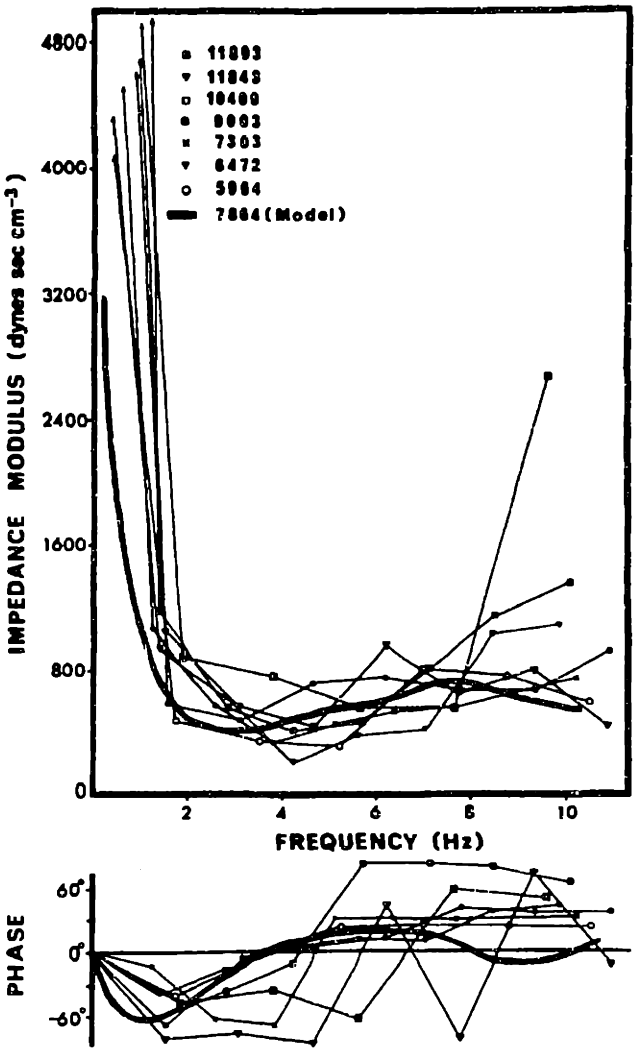

Figure 3.24. Ascending aortic impedance in seven adult humans. The dark line shows impedance calculated in a model of the human systemic arterial tree. From O'Rourke, 1992.

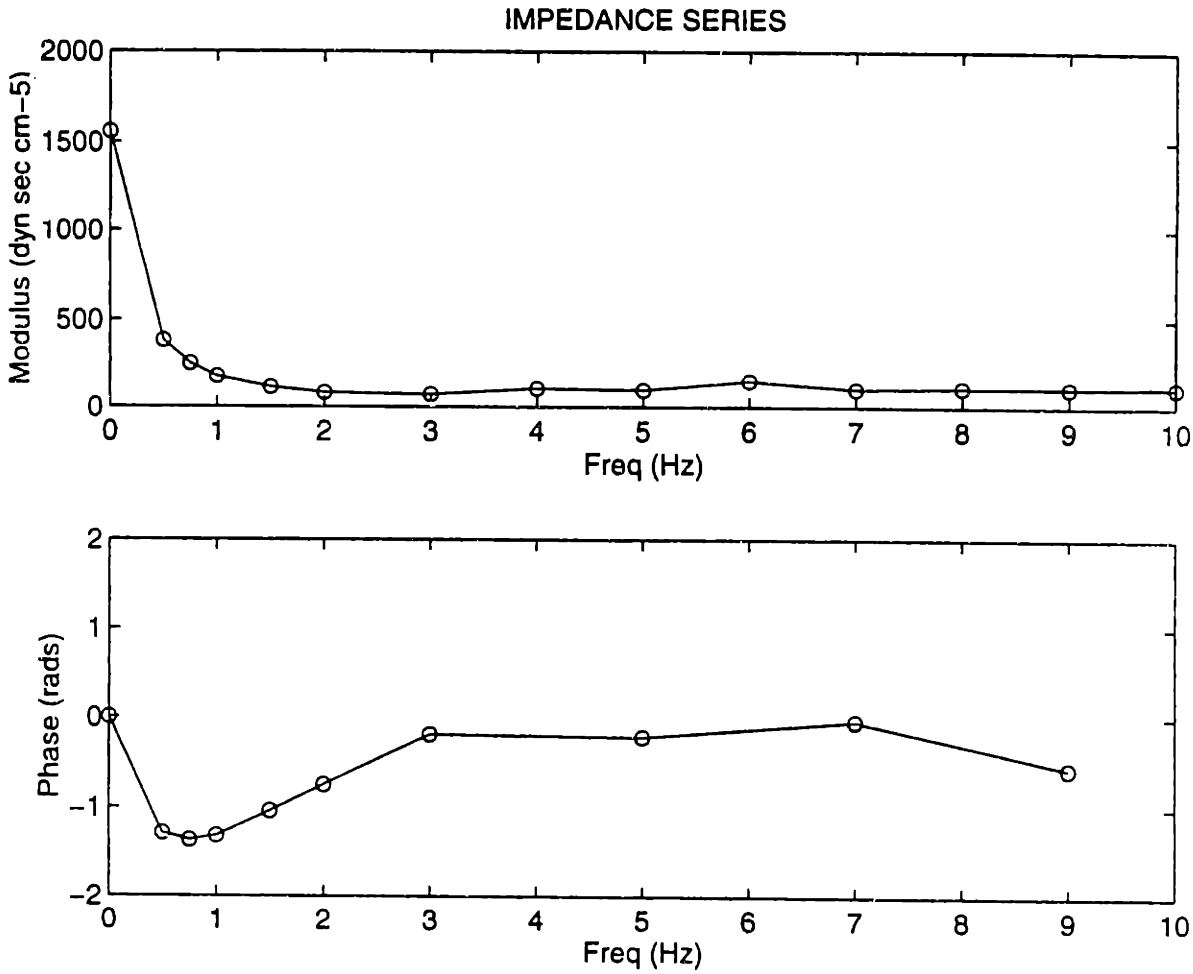

Figure 3.25. Calculated aortic root input impedance for the 28 element distributed model.

for comparison with literature. This is shown in Figure 3.25. The calculated input impedance exerts qualitatively a very similar shape to that shown in Figures 3.23 and 3.24. Additionally, the calculated phase lag shows the same reversal to approximately -1 radians at a frequency of 1 Hz as in the literature, after which it oscillates about the zero phase line at higher frequencies. Note again that a quantitative validation must be made in this case as well, since as can be seen from Figure 3.24 there exists a significant amount of variability in the impedance profiles between normal individuals. Additionally, although we have not demonstrated it here, the impedance is strongly a function of the peripheral resistance and the smooth muscle tone of the systemic arteries, which is constantly changing throughout time. Thus, one individual may be expected to give a number of different impedance profiles, depending on the conditions under which the measurements were taken (usually during surgical procedures!)

3.2.4 Lumped Parameter Model of the Venous and Pulmonary Circulation

The lumped parameter model is somewhat more difficult to verify, since the generated pressure and flow waves are rather non-physiologic and unrealistic when compared to actual measured *in-vivo* traces. Since the lumped parameter model closely followed the theory of CVSIM, described in the previous chapter, a comparison may be made to demonstrate that the theoretical modeling of a lumped parameter system is accurately solved for here. Representative plots for pressure and flow from a variety of locations throughout the CVSIM model are shown in Figure 3.26. The corresponding plots from the standard case for the lumped parameter model of the venous and pulmonary circulation are shown in Figures 3.27 and 3.28. Comparison between the CVSIM data and those generated by the standard case are in good agreement.

It is important to note that the quality of the curves obtained using the lumped parameter model are unrealistic when compared to actual physiological tracings. For instance, the flow curves shown in Figure 3.29 show an instantaneous increase in the value of flow to its peak value at the onset of systole, followed by an exponential decay. Thus, one of the most important characteristics of arterial blood flow that the lumped parameter model fails to capture is the effect of inertance, which prohibits fluid from accelerating instantaneously. This deficiency is also apparent from the tracings of right ventricular volume versus time in Figure 3.29, which shows an instantaneous change in the slope of the curve once fluid begins leaving the ventricle. This is easily contrasted with the left ventricle volume curve, where the peak dV/dt occurs later during early systole. Thus, it is clear that although the lumped parameter model is good at capturing

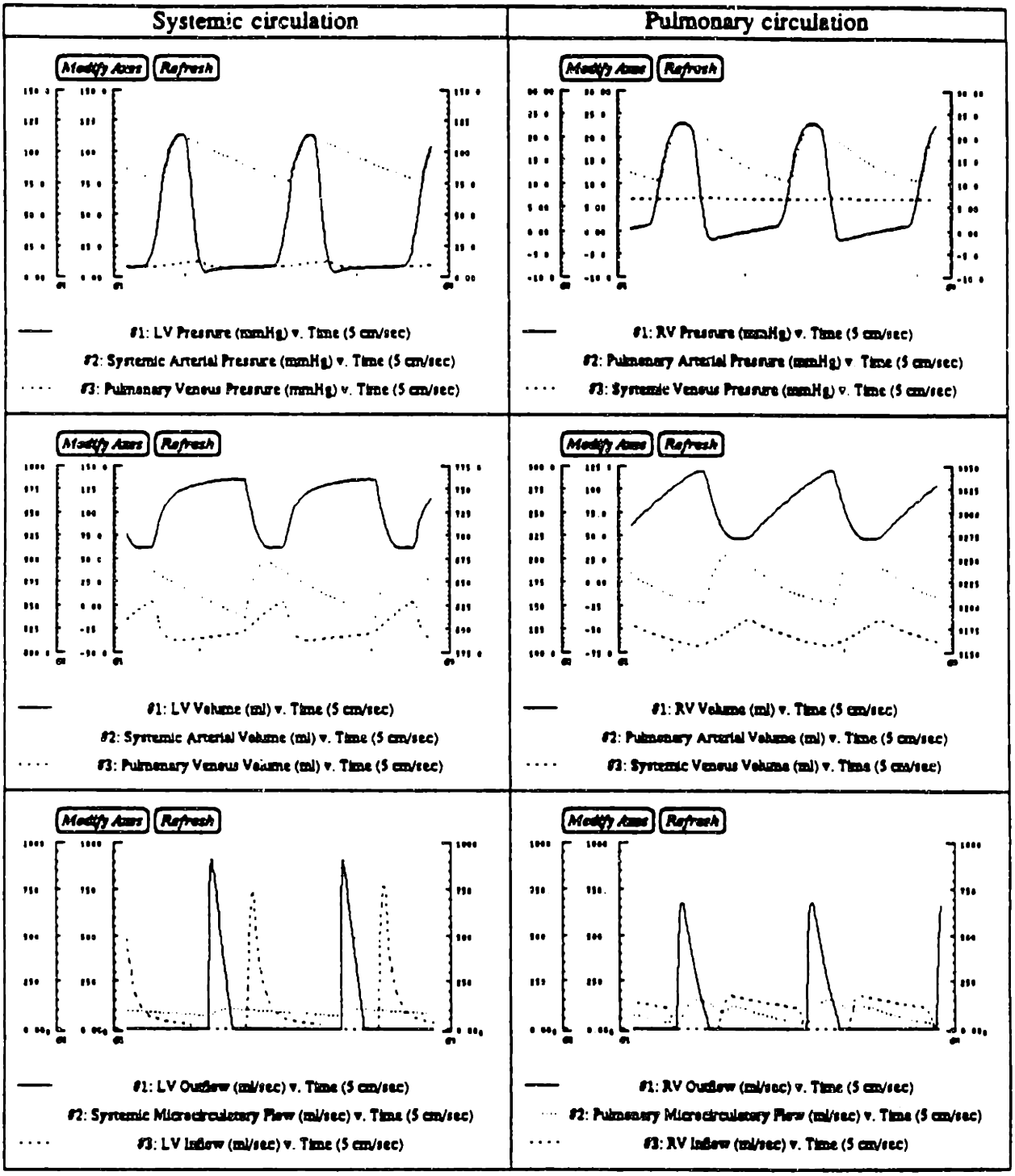

Figure 3.26. Pressure and flow tracings from CVSIM at various locations.

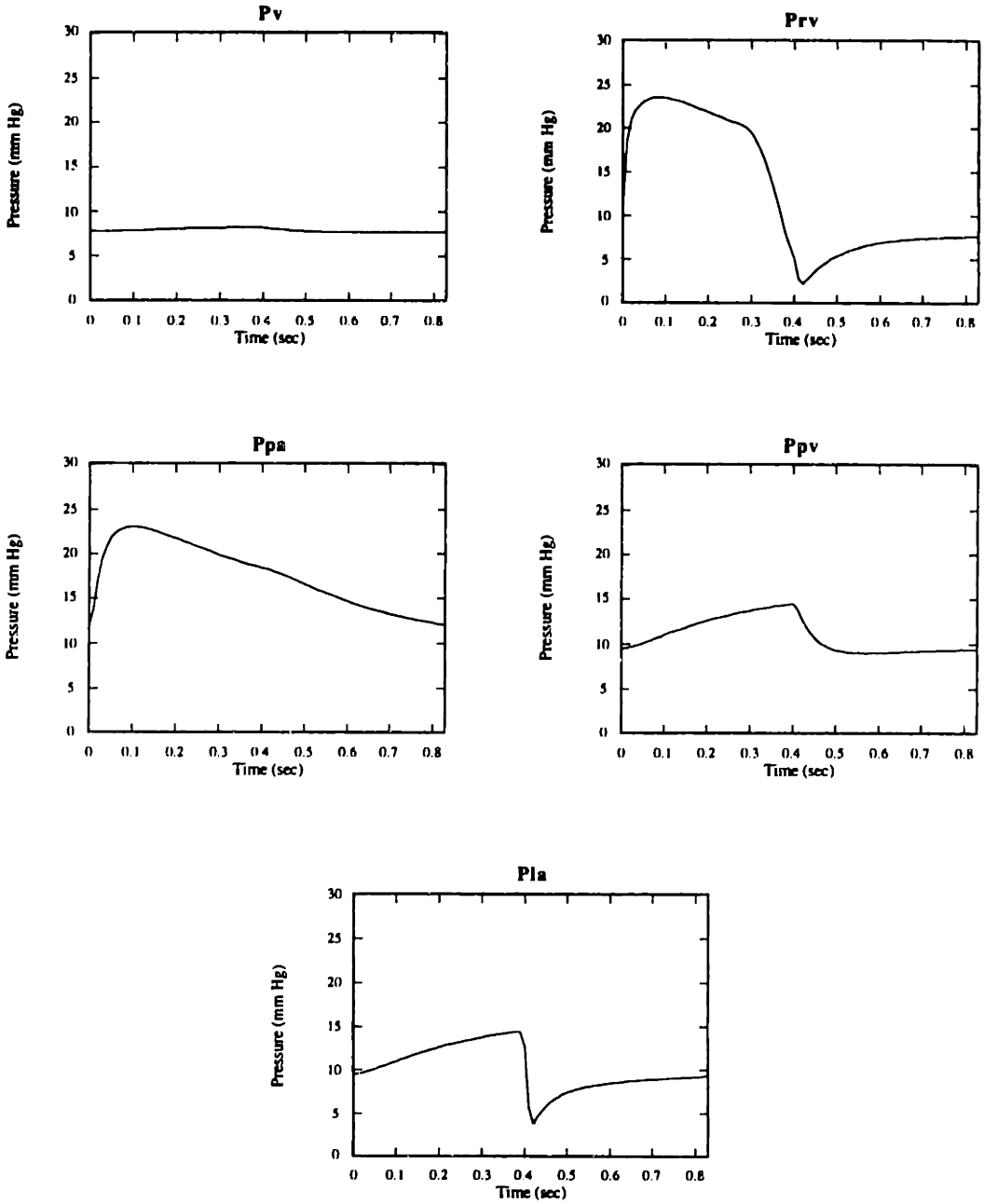

Figure 3.27. Pressure tracings from the standard case, lumped parameter model of the venous and pulmonary circulation.

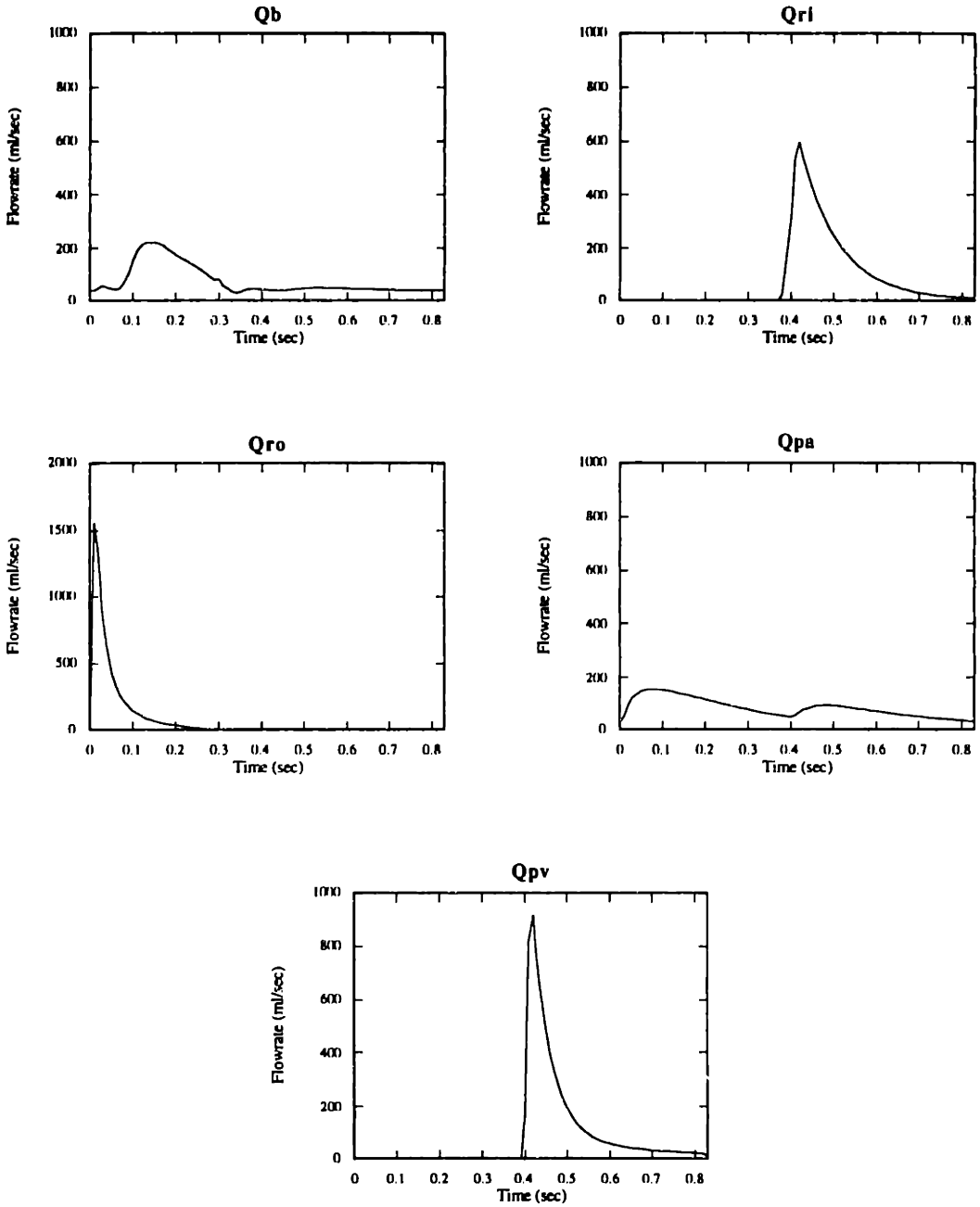

Figure 3.28. Flowrate tracings from the standard case, lumped parameter model of the venous and pulmonary circulation.

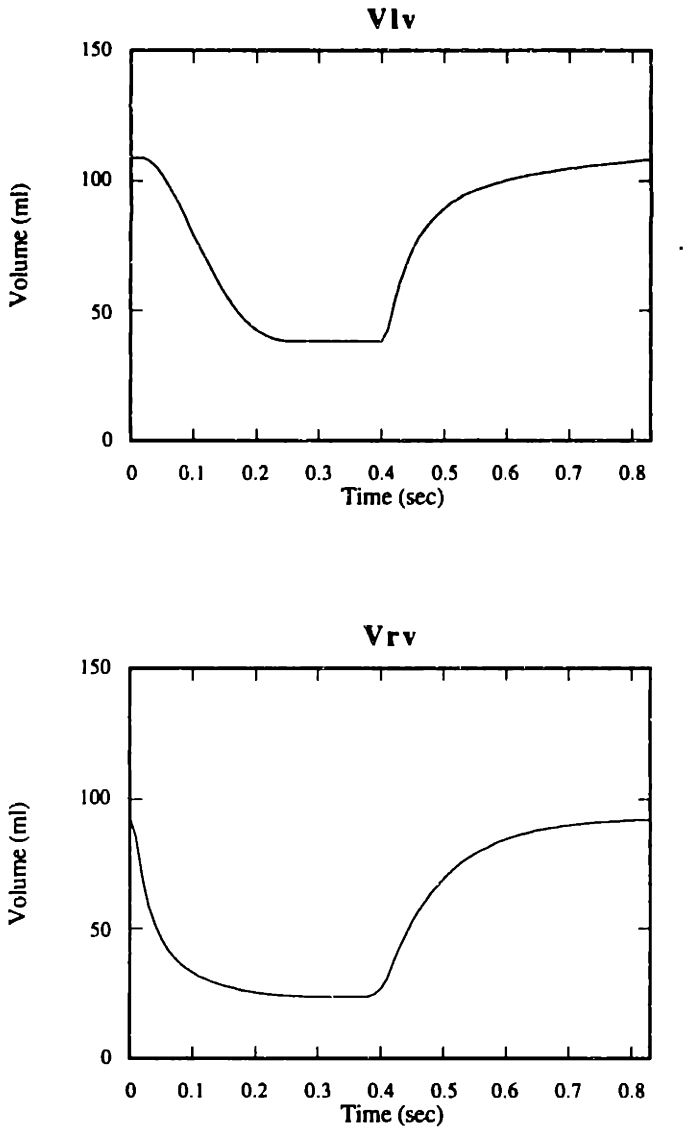

Figure 3.29. Left (top) and right (bottom) ventricle volume tracings from the standard case, incorporating the lumped parameter model of the venous and pulmonary circulation.

the overall behavior with respect to mean pressures and flowrates, the actual morphological quality of the curves is completely unphysiological. This provides further justification for the use of the distributed model in applications where accurate modeling of the physiological behavior is required, such as for parameter estimation.

3.3 Summary of the Numerical Model

The thesis to this point has concentrated heavily on the construction of a multi-purpose model of the cardiovascular system. As has been shown in this chapter, the model does a very reasonable job at reproducing the behavior of the cardiovascular system, and duplicates many of the features that have been incorporated into other previous models. The model by itself, then, cannot really be considered a significant contribution to the field, since much of the existing theory and ideas was used and incorporated, although several novel features contained in the model make it worthy of note. In its development, we attempted to contain as much of the physics as possible while keeping the complexity to a minimum, thus allowing for easy modifications when necessary.

This point marks the end of the first half of the thesis work. The novel application of the model to the problem of parameter estimation is a difficult one, and depends heavily on the quality and accuracy of the simulated waves provided by the model. The next two chapters address the theory behind the estimation scheme, and how the numerical model provides the raw data with which the scheme is implemented. From this point on the model code may be considered frozen, although in the next chapter a major modification to the model in terms of the components included will be made. This is done in order to simplify the system to the point where parameter estimation is feasible.

Chapter 4

Parameter Estimation

4.1 Introduction

In this chapter the method of parameter estimation, or the estimation of patient hemodynamic parameters from non-invasive measurements, is described. In order to follow the logic of the contents of this chapter, it is necessary to describe the method in which we propose to derive hemodynamic parameters from patient data using the numerical model. Extensive work in parameter estimation has been done in the field of engineering, and the application of "surrogates" to describe the behavior of a system, as a function of its parameters, is well established. A paper published by Yesilyurt and Patera from the Fluid Mechanics Laboratory at M.I.T. describes a system in which an eddy promoter system may be optimized in terms of minimum pump power (Yesilyurt and Patera, 1995). The system consists of a flow channel in which a cylindrical object of radius R (the promoter) is placed a distance a from the walls. Thus, the problem is to determine the set of values for R and a that result in minimum pump power requirements. This "inverse problem" can be solved by constructing a "surrogate" which describes the behavior of pump power as a function of the input parameters. Combinations of R and a within their respective range of values can be selected, and corresponding values of pump power calculated from each using a 2-dimensional CFL solver. However, since the calculation is computationally expensive, it is impossible to generate enough points to completely fill the parameter space. Instead, a small number of points is calculated, and a quadratic interpolation routine is applied to "fill in the blanks" and provide a model for the behavior of the objective function (pump power) as a function of the input parameters. From this surrogate, the desired value of minimum power can be located, and the corresponding values of R and a extracted.

A more general description of Bayesian-validated surrogate optimization and design is given by members of Yesilyurt's group (Otto et al., in publication). Here, the surrogate methodology for the use of expensive simulations to generate a more simplified input-output model is outlined. Additionally, other investigators have used stochastic methods

to describe the output of computational code for optimization purposes. Welch at al. describes such a method for screening active factors and predicting their subsequent behavior by constructing a computationally cheap surrogate predictor (Welch, 1992). In their publication, a function is defined over a 20-dimensional input space, and approximately 30-50 computed test points are generated using this function. Using these points the most important parameters are identified, and curvature and interactions are studied, and a predictor is all created using the same test points. Considering that system identification techniques are well established in the engineering literature, it is surprising that the identification of cardiovascular parameters using numerical models is in a relatively primitive state. A recent publication applies system identification to a three element windkessel model of the arterial system using pressure-dependent compliance (Capello et al., 1995). This is done by separating out mathematically the effects of the resistances from the compliances and then solving for each individually from measured canine arterial pulse data. Additional studies have been performed to estimate arterial compliance, also based on a windkessel approximation of the arterial tree (Laskey et al., 1990; Shim et al., 1994).

We propose here to perform estimation of the hemodynamic parameters using techniques similar to those outlined above by Yesilyurt and Patera. If a parameter space can be defined for a number N influential model parameters which affect the behavior of the arterial system, then an objective function which gives an indication of the error between the output of the model for a given parameter set and the actual patient data can be defined. The terms "model output" and "patient data" refer to the *pressure and velocity tracings versus time* as measured at various anatomical locations throughout the body for the numerical model and the *in-vivo* case, respectively. If a random sampling of the N-parameter space is performed, surrogates which help to describe the "error" as a function of the parameters can be constructed using the N-dimensional interpolation scheme. From the polynomial fit, the "best fit" can be located and the corresponding parameters associated with the point of minimum "error" extracted. This procedure depends on the ability to generate enough points to obtain a representative sampling of the entire parameter space from which physiological behavior is expected to result. Additionally, it depends on the fact that a unique solution can be obtained, when in fact several solutions may in fact exist. Another implication of sampling the parameter space is that as the number of parameters N increases, the number of required sample points increases exponentially (as does the time needed to accomplish all of the necessary computational runs). These issues will be addressed later in this chapter. For the

moment, it is necessary to first define the entire set of parameters that are specified for any given simulation.

4.2 Identification of the Parameter Set

In Chapter 3, a description of the literature values used to describe the standard case were outlined in detail. These numbers represent the source of variablilty in the model, and it is through the selection of parameters that one is able to create a "unique" set of inputs to the numerical model, which acts upon the physical equations through the guidance of the governing parameters. These hemodynamic parameters may be used to reflect the uniquesness of state associated with a given patient. In this section, a description of the selection process for the parameters is outlined in detail.

4.2.1 The Universal Parameter Set

Technically it is possible to identify thousands of parameters associated with the numerical model. At each nodal position is specified a cross-sectional area, wave speed, and leakage function associated with a reference pressure. This constitutes the total set of numbers required to fully describe an individual node. Since there are roughly 3000 nodes associated with a typical N-element model, this comes to rougly 10,000 parameters. One expects that between individuals these numbers vary independently of each other. Additional parameters that define the circulation include the value of the parameters associated with the terminal boundary conditions, or the windkessel approximation for arteriolar beds. Within an individual, the activity and amount of blood flow from organ to organ is in constant flux, and thus each windkessel may act independently of each other: for 21 terminal windkessels with their three associated parameters, this gives an additional 63 degrees of freedom. The prospect of attempting to determine exact behavior for a system with thousands of degrees of freedom is an impossible task. Thus, in order to accomplish what this thesis has set out to do, it is necessary to make certain simplifying assumptions.

The first and most important assumption is that of self-similarity. Human beings are generally identical in shape from person to person. We all possess two arms, two legs, a head, and so on. Likewise, the branching pattern of the arterial system, mainly of the larger vessels, is self similar. If we can account for the different sizes and shapes of people using a simple scaling of the dimensions of the basic human form (such as height), then the same argument can be made regarding the vessel branching patterns. Thus, the thousands of parameters that may be used to describe the geometry (i.e. lengths, cross-sectional areas at a reference pressure, artery wall thickness, and branching angles) can be

reduced to a single length scale, and hence a single parameter. With respect to branching angle, no modifications need to be made, as relative angles do not alter with the geometrical scaling of the entire system. Given acceptance of this assumption, one may proceed further and assume that material properties of arterial walls are also self-similar. Thus, if given a description of the variation in wall Young's modulus as a function of location and vessel type, then a single parameter may be used to scale the value to accomodate for the variations in vessel stiffness seen between indivuals. The notion of a global scaling factor is probably appropriate, since most mechanisms which act to alter vessel stiffness (such as aging or hyperlipidemia leading to atherosclerosis) are generally of a systemic, rather than a local, nature. It should be noted that the sepcification of wall stiffness using E is interchangeable with the specification of wavespeed c, since from equation (3.1.1) if one specifies the geometrical components of the equation, then only one additional parameter needs to be specified.

If one is having difficulty accepting this argument, imagine the human arterial system as a 2-D drawing on a sheet of paper drawn to scale. To obtain the correct geometrical parameters for a person 50% larger than the one presented on the sheet, one only needs to punch up a photocopy enlargement factor of "150%" and hit the "copy" button. What comes out is an image of the original, identical in shape, but scaled larger in length and diameter. Thus, we have successfully transformed the thousands of degrees of freedom for the *geometry* and *material properties* of the arterial tree into 2 mere degrees of freedom; a length scale and a reference Young's modulus. Two additional parameters B and χ_o can be obtained from the relationship between wavespeed and intra-arterial pressure, equation (2.2.9). An additional three parameters a, τ_1, and τ_2 are required for description of the wall viscoelasticity behavior, given in equation (2.2.28). Thus, a total of 7 parameters specify the material and geometrical properties of the elastic artery segments.

Distribution of cardiac output hasd been discussed in detail in the previous chapter. The notion of self-similarity also applies somewhat in this case. The cardiac output measured at the aortic root varies regularly and widely, and is essentially a function of the oxygen demands of the individual. This is in turn a function of the level of physical exertion at the time that cardiac output is measured, as well as the size of the individual (or body surface area, which is used to define the normalized cardiac output, or the cardiac index). However, one can assume that the distribution of cardiac output to each organ, normalized against the total cardiac output, remains fairly constant. Thus, a larger individual will be expected to achieve a higher cardiac output, and therefore a higher splanchnic flow, for instance, than in a smaller individual. However, in both individuals

the fraction of total cardiac output delivered to the splanchnic organs during the same basal state can be expected to be similar.

Such an assumption obviously breaks down as the basal state changes within a person: splanchnic circulation increases following a meal, and decreases during exercise. Likewise, the peripheral resistance to flow changes dramatically depending on the state of the patient. During exercise, resistance to flow in the limbs decreases while flow to the cenrtral organs reduces to almost zero, accompanied by an overall decrease in the systemic vascular resistance. Conversely, immediately following a meal peripheral blood flow decreases while splanchnic flow increases, accompanied by a general decrease in cardiac output and an increase in the total systemic resistance. Hence, we may use two parameters to describe the alterations in resistance. One parameter can be used to scale the total systemic resistance by multiplying the value of all of the resistive elements by the *same* factor: hence, this parameter is proportional to the cardiac output expected at a mean arterial reference pressure (100 mm Hg). This parameter can be thought of as a scaling proportionality for the outflow resistance at each windkessel, defined from the standard case at a reference arterial pressure. Additionally, the transmural wall leakage coefficient Φ can be assumed to scale also with the systemic resistance parameter.

Another factor can be used to describe the distribution of flow between the peripheral and central organ beds. This parameter can be described as the fraction of flow to the splanchnic vessels compared to nominal flow values (at the reference pressure), and can be applied to the outflow resistance values of these related vessels only. Thus, if one sets the splanchnic flow parameter to a small number, but uses also a large value to describe a generalized systemic decrease in arterial resistance elsewhere, then the distribution of cardiac output during exercise conditions may be modeled. Admittedly, this two-parameter approximation of the regulation of blood flow is somewhat simplistic. However, the results that we obtain in the next section justify the simplification, which is appropriate for the level of approximation that the 28 element model provides. To summarize, 9 parameters are required to characterize the arterial tree geometry, material properties, and flow distribution.

There are eleven parameters associated with both the left and right ventricles. From equation (2.3.20) we see that they include maximum and minimum ventricle wall elastances $E_{lv,rv,max}$ and $E_{lv,rv,min}$ for each ventricle contained within $E^*(t)$, the zero pressure filling volume $V_{lv,rv,o}$, ventricle viscosity σ, and transthoracic pressure P_{th}. Additional parameters include heart rate f, and the systolic/period time ratio which we denote as Ω, equal to the fraction of time out of each cycle that the ventricle is actively changing its elastance (also referred to as the ejection period). It is a poor assumption make that

Table 4.1-a List of model parameters. The equation from which the parameters were taken, and the nominal value of each parameter are also listed.

#	Name	Equation Source	Nominal Value
1	HEART RATE	(2.3.21)	72 BPM
2	LEFT VENTRICLE Emax	(2.3.21)	6000 dyn/cm^5
3	LEFT VENTRICLE Emin	(2.3.21)	133 dyn/cm^5
4	LEFT VENTRICLE 0-PRESS VOL	(2.3.21)	15 ml
5	LEFT VENTRICLE VISCOSITY	(2.3.21)	0.001 sec/ml
6	RIGHT VENTRICLE Emax	(2.4.2)	3000 dyn/cr .^5
7	RIGHT VENTRICLE Emin	(2.4.2)	133 dyn/cm^5
8	RIGHT VENTRICLE 0-PRESS VOL		15 ml
9	SYSTOLIC/DIASTOLIC TIME RATIO	(2.3.21)	50%
10	TRANSTHORACIC PRESSURE	(2.3.21)	(-)5 mm Hg
11	SINUS OF VALSALVA Csinus	(2.3.18)	0.00005 cm^5/dyn
12	VISCOELASTIC WALL CREEP f(a)	(2.2.30)	0.30
13	VENOUS PRESSURE	(2.4.1)	8 mm Hg
14	VENOUS Cv	(2.4.1)	0.075 cm^5/dyn
15	VENOUS Rv (Rri)	(2.3.22) (2.4.5)	13.33 dyn-sec/cm^5
16	PULMONARY Rro	(2.4.6)	4 dyn-sec/cm^5
17	PULMONARY Cpa	(2.4.3)	0.0032 cm^5/dyn
18	PULMONARY Rpa	(2.4.7)	107 dyn-sec/cm^5
19	PULMONARY Cpv	(2.4.4)	6.30E-03
20	PULMONARY Rpv	(2.4.8)	13.3 dyn-sec/cm^5
21	BLOOD VISCOSITY	(2.2.25)	0.04 cp
22	LENGTH SCALE		1.00
23	ARTERY WALL STIFFNESS E		1.00
24	WINDKESSEL Rs	(2.3.22)	1.00
25	WINDKESSEL TIME CONSTANT Cs	(2.3.22)	0.70
26	AUTONOMIC AXIS/C.O. DIST		1.00
27	BIFURCATION Kc	(2.3.10) (2.3.11)	0.75

Table 4.1-b List of model parameters, maximum and minimum values, and the dimensionless value.

#	Nominal Value	Minimum Value	Maximum Value	Dimensionless Value
1	72 BPM	20	200	0.29
2	6000 dyn/cm^5	1000	15000	0.36
3	133 dyn/cm^5	50	500	0.18
4	15 ml	0	100	0.15
5	0.001 sec/ml	0	0.005	0.20
6	3000 dyn/cm^5	500	7500	0.36
7	133 dyn/cm^5	50	500	0.18
8	15 ml	0	100	0.15
9	50%	20%	80%	0.50
10	(-)5 mm Hg	-20	0	0.75
11	0.00005 cm^5/dyn	1.00E-05	3.00E-04	0.14
12	0.30	0.00	1.00	0.30
13	8 mm Hg	0	50	0.16
14	0.075 cm^5/dyn	0.01	0.1	0.72
15	13.33 dyn-sec/cm^5	1.00	100.00	0.12
16	4 dyn-sec/cm^5	1.00	10.00	0.33
17	0.0032 cm^5/dyn	1.00E-03	1.00E-02	0.25
18	107 dyn-sec/cm^5	10	500	0.20
19	6.30E-03	1.00E-03	1.00E-02	0.59
20	13.3 dyn-sec/cm^5	1	100	0.12
21	0.04 cp	0.01	0.10	0.33
22	1.00	0.50	1.50	0.50
23	1.00	0.50	2.00	0.33
24	1.00	0.25	4.00	0.20
25	0.70	0.30	1.00	0.57
26	1.00	0.00	2.00	0.50
27	0.75	0.40	1.00	0.58

alterations in the elastance of one ventricle is mirrored by a corresponding change in the other since disease processes such as ischemic cardiomyopathy are inherently asymmetric due to, for instance, the individual coronary artery branches that feed the left and right hearts independently. An assumption of non-symmetry with respect to ventricle viscosity, however, is less stringent since σ is only expected to modify the shape of the forward ejection wave, which is of no concern in the right heart and the lumped parameter model. Finally, transthoracic pressure is a parameter that has symmetric effects, as the pressure exerted on the pericardium by the thorax is uniform.

The parameters used to describe the venous and pulmonary circulations are fairly straighforward, since the parameter set for this portion of the model corresponds simply to the values for resistances and compliances that are specified in Section 3.1.5. This contributes an additional seven parameters, bringing the total to 27. There are also two additional properties associated with blood itself: viscosity and density. As mentioned previously, neither of these values deviate significantly in the physiological condition, even in states of extreme fluid overload (edema) or dehydration. However, these parameters nonetheless are useful as will be seen later. Thus, we have arrived at a total of 29 parameters that describe the specific state of an individual patient. A summary of all of the model parameters described above is given in Table 4.1. The table also lists the theory equations that each parameter is associated with.

Nominal values for all parameters from the standard case are given in the first column of Table 4.1. In the actual physiological system, however, most of these parameters are not fixed, but vary in order to give rise to the changes in arterial system behavior specific to an individual's state of health or physical activity. Therefore, associated with each parameter is a minimum and maximum value, defining the range over which each parameter might be expected to vary over. For the most part, the selection of the upper and lower bounds is somewhat arbitrary, although resonable in value. However, some attempt has been made to identify the physiological operating range of each parameter. References for those ranges obtained by literature are labeled as such in the table. However, as we will see, a conservative estimate of the range is sufficient to obtain the wide range of effects seen in the human physiological system, normal or otherwise. Additionally, one can specify a dimensionless linear scale (denoted by the carat) for each parameter Π over its range from Π_{min} to Π_{max}:

$$\hat{\Pi} = \frac{\Pi - \Pi_{min}}{\Pi_{max} - \Pi_{min}} \tag{4.2.1}$$

The dimensionless value corresponding to the nominal value (defined as the standard case) over its range is given in the final column of Table 4.1. The definition of a dimensionless range becomes particularly important if one wishes to weigh the relative contributions of each to the entire behavior of the circulatory system. The next section outlines a method in which the activity of each parameter may be assessed.

4.2.2 Parameter Screening

The range of values for each parameter in Table 4.1 allows for a method of estimating the relative contribution of each parameter in terms of its morphological and quantitative effects on the model output, the pressure and flow waves measured at different anatomical locations. The model outputs are expected to yield a single unique output for a given set of input parameters, consisting of a set of pressure and velocity tracings. In order to determine the relative effects of each parameter on the objective function, each parameter was varied in turn on its dimensionless scale from the standard case by a value of 0.1 up and 0.1 down (i.e. 10% of the total operating range), while keeping all of the other parameters constant. A total of 58 simulations (2 for each parameter) were then performed for each varied parameter set so that a new output was calculated in each case. An error function was then defined so that the deviation of each new run with its single adjusted parameter could be compared with the standard case. Although the error function may be defined in many ways, the simplest to implement is the root mean square error function. If one wishes to compare a set of data $\boldsymbol{p}_m$ of length n taken from the aortic root pressure with a set of calculated data $\boldsymbol{p}_c$ taken from the same location, where both share the same time axis, then the root mean square error may be written as:

$$\varepsilon_{rms} = \frac{1}{n\bar{p}_m}\sum_{j=1}^{n}(p_c^j - p_m^j)^2 \qquad (4.2.2)$$

where

$$p_m = \{p_m^1, p_m^2, \ldots, p_m^n\} \ldots\ldots \text{and} \quad p_c = \{p_c^1, p_c^2, \ldots, p_c^n\} \qquad (4.2.3), (4.2.4)$$

and the mean of the measured set is indicated by the over bar. Thus, when calculating the deviation of a run with an altered parameter from that of the nominal, standard case, the calculated aortic root pressure as a function of time from both cases can be fitted to a spline approximation, so that a one-to-one correspondence of pressure at one particular time can be made (since the two runs would be expected to contain values sampled at

different times, due to the variability of the timestep during calculation using the finite difference scheme). The time axis for the spline approximation in both was discretized into 100 timesteps and made dimensionless, ranging from 0.0 to 1.0. Additionally, both curves were made dimensionless so that the pressure values were normalized in *both* curves by the minimum and maximum values from the *standard* case (where the minimum is set equal to 0.0, and the maximum to 1.0, with all values linearly scaled in between). In equation form, the dimensionless P_m for the standard case and the dimensionless P_c for the test case can be solved as:

$$P_m = \frac{P'_m - \min(P'_m)}{\max(P'_m) - \min(P'_m)} \tag{4.2.5}$$

$$P_c = \frac{P'_c - \min(P'_m)}{\max(P'_m) - \min(P'_m)} \tag{4.2.6}$$

where P'_m is the dimensional standard case, and P'_c is the dimensional test case to be compared against. Note that this definition of error will always yield a positive value. This non-dimensionalization is performed in order to compare the relative changes in not only pressure, but also velocity; since the dimensional velocity is closer to zero in value than the dimensional pressure, if non-dimensionalization were not performed the relative values of error computed using equation (4.2.2) would not be comparable.

Athough we have mentioned the aortic pressure as one location for which an error function can be defined, additional values for error can also be calculating by repeating the analysis at other locations, and also by comparing velocities. These locations are determined by taking into consideration the methods available to the clinician to non-invasively measure both pressure (using a tonometer) and velocity (using Doppler ultrasound) waves in a patient. Measurement techniques will be covered in further detail in Chapter 5. These locations include the carotid arteries (both pressure and velocity), the brachial artery (velocity), the radial artery (pressure), the femoral artery (velocity), and the tibial artery (velocity). Note that we have included in the screening process the pressure and velocity at the aortic root as a location to define the error, although in practice it is extremely difficult to measure both in the clinical setting.

By taking the average deviation from all of the measurement locations, a single composite ranking of the error as a function of parameter deviation taken at the 8 locations listed above can be constructed and summarized in a single table (Table 4.2). The deviation at specific measurement locations are given in Appendix A. The corresponding plots of pressure and velocity that graphically show the deviations as a

Table 4.2. Results of the parameter screening.

Parameter #	Parameter Name	Mean RMS Error
13	VENOUS PRESSURE	1.70
22	LENGTH SCALE	1.19
1	HEART RATE	1.10
24	WINDKESSEL Rs	1.05
3	LEFT VENTRICLE Emin	0.91
7	RIGHT VENTRICLE Emin	0.84
5	LEFT VENTRICLE VISCOSITY	0.55
23	ARTERY WALL STIFFNESS E	0.40
2	LEFT VENTRICLE Emax	0.36
26	AUTONOMIC AXIS/C.O. DIST	0.33
9	SYSTOLIC/DIASTOLIC TIME RATIO	0.25
6	RIGHT VENTRICLE Emax	0.21
27	BIFURCATION Kc	0.20
15	VENOUS Rv	0.20
25	WINDKESSEL TIME CONSTANT Cs	0.18
18	PULMONARY Rpa	0.18
11	SINUS OF VALSALVA Csinus	0.18
20	PULMONARY Rpv	0.18
17	PULMONARY Cpa	0.17
19	PULMONARY Cpv	0.17
12	VISCOELASTIC WALL CREEP f(a)	0.17
10	TRANSTHORACIC PRESSURE	0.17
4	LEFT VENTRICLE 0-PRESS VOL	0.17
16	PULMONARY Rro	0.17
8	RIGHT VENTRICLE 0-PRESS VOL	0.17
14	VENOUS Cv	0.17
21	BLOOD VISCOSITY	0.15

function of the parameters are summarized in Appendix B. Note that the rank order of each parameter changes as a function of measurement location. One would expect this result based on the assumption that parameters that affect left ventricular function would be expected to exert effects proximally, while parameters affecting the terminal boundary conditions would have stronger effects in the more distal measurement locations.

Looking more closely at Table 4.2, we note that there exists a gradient of deviation, where parameters associated with the arterial system exert stronger effects on its behavior than do the parameters associated with the lumped parameter model. Furthermore, parameters such as blood viscosity, density, and the bifurcation contraction coefficient K_c exert little influence. Thus the argument can be made to fix these parameters constant, as they would be expected to contriubute little to the overall morphological quality of the arterial pressure and velocity waves. One also notes that the right ventricular minimum elastance has a large effect on the arterial pressure, due to its ability to regulate right ventricular stroke volume, which in turn affects pulmonary pressures and hence filling of the left ventricle during diastole.

To perform parameter estimation effectively, it is necessary to isolate only a handful of parameters from the many which fully describe the behavior of the arterial system. However, from the results of the parameter screening it is obvious that more than just a handful of parameters are important. The screening technique does not provide ample justification to fix 20 parameters constant, while allowing only 9 or so to vary. As we have briefly mentioned before, it is computationally too expensive at the present time, given the current speed of computational platforms, to perform parameter estimation using more than 6 parameters. For the construction of the parameter space library, assuming that each parameter axis may be discretized into 4 points, to fully screen the entire space would require 4^6 runs, which on the fastest machine available in the Fluid Mechanics Laboratory would require weeks of computational time to perform. Clearly, certain modifications will have to be made to the parameter set in order for parameter estimation to become feasible. Hence, in the next section we describe a series of simplifications to the model, and the application of dimensinal analysis, to help reduce the size of the parameter set.

4.3 Reduction of the Number of Parameters

An approach to reducing the number of parameters is to take advantage of non-dimensionalization and use a subset of the total parameters to define dimensionless parameters from the remaining subset. Three parameters are required in order to describe

a dimensionless time, length, and mass. Thus, the total number of parameters required to describe the system can be reduced by three. Careful evaluation of the parameters leads us to select the heart rate as a reference wavespeed c_o (the wavespeed at the root of the aorta as an indicator of arterial stiffness), a reference length L (the height of the individual), and the density of blood ρ. This yields:

$$\tilde{t} = \frac{tc_o}{L} \qquad \tilde{x} = \frac{x}{L} \qquad \text{(4.3.1), (4.3.2)}$$

for the dimensionless time and length. We can also define:

$$\tilde{u} = \frac{u}{c_o} \qquad \tilde{P} = \frac{P}{\rho c_o^2} \qquad \tilde{A} = \frac{A}{L^2} \qquad \text{(4.3.3), (4.3.4), (4.3.5)}$$

for the dimensionless state variables of velocity, pressure, and area, where the tilda superscript represents non-dimensionality. All of the equations associated with the cardiovascular model may be non-dimensionalized with the above definitions. This yields numerous dimensionless parameters which are summarized in Table 4.3. We arbitrarily define a set of "variable" dimensionless parameters by taking the corresponding top ten most influential dimensional parameters determined from the results of the parameter screening in Table 4.2. The rest of the dimensionless parameters in Table 4.3 are said to be "fixed" (constant), since their dimensional forms were shown to have little effect on the behavior of the model. One should note that two of our dimensionalizing terms L and f are also found to strongly influence model behavior, and thus the terms in the dimensionless variable parameters are allowed to vary independently of each other. The same assumptions cannot be made, however, for many of the fixed dimensionless parameters. For instance, in the dimensionless term C_v^* (dimensionless venous compliance) if the term C_v is to be held fixed using the results of the screening, then one cannot expect its non-dimensionalized form to also be fixed, since c_o and L are allowed to vary. Thus, the reduced subset of model parameters that was identified by the screening process is lost with the non-dimensionalization procedure. What results then is an increase in the number of necessary dimensionless parameters to describe model behavior, and not a decrease as we had hoped. Another approach must be taken if we are to reduce the total number of parameters to a manageable handful.

Since the scope of the thesis is primarily directed at assessing hemodynamics using pulse information obtained from the arterial tree, one can reassess the set of equations needed to define the model outputs. If one is only interested in the arterial waveforms generated by the model for purposes of parameter estimation, then one needs only worry about the equations (and therefore parameters) that have *direct* effects on the arterial tree

Table 4.3. Left and right ventricle parameters.

#	Dimensionless Form	Description
1	$\tilde{f} = \frac{fc_o}{L}$	Heart rate $f = HR/60.0$
2	$\tilde{\sigma} = L^2 c_o \sigma$	Ventricular viscosity coefficient σ
3	$\tilde{\tau}_s = \frac{\tau_s c_o}{L}, \quad \Omega = \tau_s \cdot f$	Ejection period
4	$\tilde{C}_{sinus} = \frac{\rho C_{sinus} c_o^2}{L^3}$	Sinus of valsalva compliance
5	$\tilde{P}_{th} = \frac{P_{th}}{\rho c_o^2}$	Transthoracic pressure
6	$\tilde{V}_{lv,o} = \frac{V_{lv,o}}{L^3}$	Left ventricle zero-pressure filling volume
7	$\tilde{V}_{rv,o} = \frac{V_{rv,o}}{L^3}$	Right ventricle zero-pressure filling volume
8	$\tilde{E}_{lv,max} = \frac{L^3 E_{lv,max}}{\rho c_o^2}$	Left ventricle maximum elastance
9	$\tilde{E}_{lv,min} = \frac{L^3 E_{lv,min}}{\rho c_o^2}$	Left ventricle minimum elastance
10	$\tilde{E}_{rv,max} = \frac{L^3 E_{rv,max}}{\rho c_o^2}$	Right ventricle maximum elastance
11	$\tilde{E}_{rv,min} = \frac{L^3 E_{rv,min}}{\rho c_o^2}$	Right ventricle minimum elastance

Table 4.4. Arterial element parameters.

#	Dimensionless Form	Description
12	$\tilde{\mu} = \frac{\mu}{\rho c_o L}$	Blood viscosity
13	$\tilde{\Phi} = \frac{\rho c_o \Phi}{L}$	Transmural leakage
14	$\tilde{A}_o^e = \frac{A_o^e}{L^2}$	Reference cross-sectional area
15	$\tilde{\chi}_o = \frac{\chi_o}{c_o}$	Wavespeed coefficient, equation (2.2.9)
16	$\tilde{B} = \rho B c_o$	Wavespeed coefficient, equation (2.2.9)
17	$\tilde{P}_e = \frac{P_e}{\rho c_o^2}$	External wall pressure, equation (2.2.9)
18	$\tilde{g} = g$	Wavespeed coefficient, equation (2.2.9)
19	$\tilde{a} = a$	Viscoelasticity coefficient, equation (2.2.30)
20	$\tilde{\tau}_1 = \frac{\tau_1 c_o}{L}$	Viscoelasticity time constant, equation (2.2.30)
21	$\tilde{\tau}_2 = \frac{\tau_2 c_o}{L}$	Viscoelasticity time constant, equation (2.2.30)

Table 4.5. Additional and venous and pulmonary parameters.

#	Dimensionless Form	Description
22	$\tilde{x}_1 = \frac{x_1}{L} \quad \ldots \quad \tilde{x}_N = \frac{x_N}{L}$	Bifurcation entrance/exit lenghts
23	$\tilde{C} = C$	Bifurcation loss coefficient, equation (2.3.4)
24	$\tilde{K}_c = K_c$	Bifurcation contraction coefficient
25	$\tilde{Z}_o = \frac{Z_o L^2}{\rho c_o}$	Windkessel input impedance
26	$\tilde{R}_s = \frac{R_s L^2}{\rho c_o}$	Windkessel resistance
27	$\tilde{C}_s = \frac{\rho C_s c_o^2}{L^3}$	Wndkessel compliance
28	$\tilde{R}_v = \frac{R_v L^2}{\rho c_o}$	Venous resistance
29	$\tilde{R}_{ro} = \frac{R_{ro} L^2}{\rho c_o}$	Right heart outflow tract resistance
30	$\tilde{R}_{pa} = \frac{R_{pa} L^2}{\rho c_o}$	Pulmonary artery resistance
31	$\tilde{R}_{pv} = \frac{R_{pv} L^2}{\rho c_o}$	Pulmonary venous resistance
32	$\tilde{C}_v = \frac{\rho C_v c_o^2}{L^3}$	Venous compliance
33	$\tilde{C}_{pa} = \frac{\rho C_{pa} c_o^2}{L^3}$	Pulmonary artery compliance
34	$\tilde{C}_{pv} = \frac{\rho C_{pv} c_o^2}{L^3}$	Pulmonary venous compliance

behavior. These include equations associated with the left ventricle: the diastolic pulmonary venous pressure $P_{pv}(t)$, transthoracic pressure P_{th}, left ventricle minimum elastance $E_{min,lv}$, peak left ventricular elastance $E_{max,lv}$, ventricular viscoelasticity coefficient σ, and left ventricular zero-pressure filling volume $V_{lv,o}$. There are also parameters associated with the arterial tree: the arterial reference length L, arterial reference wavespeed c_o, systemic vascular resistance R_s, windkessel compliance C_s, and venous pressure $P_v(t)$. There are also parameters associated with the behavior of arterial elements, such as the coefficients B, χ_o (pressure-wavespeed coupling), a, τ_1, τ_2 (viscoelasticity coefficients), $W(\tau)$ (transient wallshear) and P_e (external transmural pressure). The windkessel parameters are also included in this list. Finally, there are the parameters μ and ρ associated with the fluid medium. We have therefore neglected the equations associated with the lumped parameter approximation of the venous and pulmonary circulations, since the arterial system is only affected by those variables which directly enter into the equations that describe the arterial system behavior (i.e. $P_v(t)$ and $P_{pv}(t)$). Thus, we can effectively throw out parameters 28-34 in Table 4.5.

The parameter set can be simplified even further by assuming that venous pressure varies little in comparison to the large amplitude pressure changes seen in the arterial system. Thus, time-dependant changes in $P_v(t)$ can be neglected, and the variable can be transformed into a time-invariant parameter P_v representing the mean central venous pressure. This leaves only one equation (2.3.21) in our reduced parameter set that is a function of this variable turned into a newly defined parameter. Additional simplifications can be made if one assumes that if left ventricular end diastolic volume LVEDV (or simply *EDV*) minus $V_{lv,o}$ volume is a function purely of diastolic pulmonary venous pressure $P_{pv}(t)$, $E_{min,lv}$, and P_{th} through equation (2.3.20). In other words, the only effect that these three parameters have on the arterial system is in determining the final steady state diastolic volume of the left ventricle. One may therefore condense these three controlling parameters (formerly variables) into *one* parameter *EDV*, in conjunction with $V_{lv,o}$. Such a simplification is further validated by the observation that in numerical tests the left ventricular behavior during systole is essentially independent of $E_{lv,min}$ and P_{th} for a given specified *EDV* and $V_{lv,o}$.

Concomitant with a reduction in the overall number of parameters is a decrease in the set of equations now used to describe the system, since we have thrown out those related to the lumped parameter model. This still results in quite a large number of variables, much larger than the five or six that would allow parameter estimation to be carried out. However, one may repeat the non-dimensionalization using the same dimensionless groups (equations (4.3.1) through (4.3.5)) as before, since our reduced

Table 4.6. The six final parameters selected for parameter estimation.

#	Dimensionless Form	Description
1	$\tilde{f} = \frac{fc_o}{L}$	Heart rate
2	$\tilde{E}_{lv,max} = \frac{L^3 E_{lv,max}}{\rho c_o^2}$	Peak left ventricle elastance
3	$EDV = \frac{EDV}{L^3}$	End diastolic volume
4	$\Omega = \tau_s \cdot f$	Ejection period
5	$\tilde{P}_v = \frac{P_v}{\rho c_o^2}$	Central venous pressure
6	Φ and R_s where $\frac{\Phi R_s}{L}$ = constant	Peripheral resistance

parameter set still contains those original three which are used to form the dimensionless state variables. Non-dimensionalization of the reduced equation set from Tables 4.3, 4.4, and 4.5 yields the smaller, new set of dimensionless groups identical to parameters 1 through 27.

Close examination of the reduced dimensionless parameter set reveals that most of the parameters can be assumed to be constant. The dimensionless terms 18, 19, 23, and 24 in Tables 4.4 and 4.5 can be considered fixed, since they are already dimensionless and therefore independent of the other terms. The dimensionless geometrical parameters can also be held constant. For instance, if one recalls the assumption of self-similarity between individuals, then the reference cross-sectional area A scales with the square of the reference length L. Also, parameter 16 that describes the entrance lengths for the bifurcation regions can be held constant, since the lengths x_1 ... x_N also scale directly with the reference length L. A similar argument may be made for fixing $V_{lv,o}$ (term 6 in Table 4.3) if one assumes that a larger individual posesses a larger-than-normal heart, and thus ventricular volume scales with the cube of L. Such an assumption may be invalidated in forms of hypertrophic cardiomyopathy, although parameter screening has shown that changes in $V_{lv,o}$ has little effect on the overall quality of the forward pressure wave, and therefore may be excluded. Additionally, one could go further and simply lump $V_{lv,o}$ with the EDV parameter to describe the total diastolic ventricle volume, in which EDV may be expected to increase as with hypertrophy or decreased ventricle diastolic compliance.

A second category of parameters that can be held fixed are those whose dimensional forms have been shown to exert little effect on the behavior of the arterial system. These are parameters 12 (Reynold's number), and 17 (external arterial wall pressure P_e) in Table 4.4. Remaining dimensionless parameters associated with stiffness of the arterial system may also be made constant. One can assume that the stiffness at any location in the arteries is scaled against stiffness in one location, again from self-similarity arguments. The reference wave speed at the aortic root, c_o, is an indirect measure of wall stiffness and therefore is an appropriate parameter to normalize compliances with. Hence, processes of age or systemic disease would tend to increase the stiffnes of all arteries; the effects of localized changes in stiffness are therefore excluded. This allows us to fix the dimensionless parameters 4 (C_{sinus}) in Table 4.3, and 15 (χ_o), 16 (B), 20, and 21 (the viscoelaticity time constants) in Table 4.4, which all scale with c_o. A similar argument can be used to fix parameters 25 and 27 in Table 4.5, the windkessel entrance impedance Z_o and compliance C_t respectively, both of which can be expected to reflect changes in the stiffness and geometry of their parent branch.

This leaves a total of 7 parameters which can be used as an input parameter set for the parameter estimation. However, one may make a somewhat reasonable argument to fix one additional parameter constant. Since the behavior regarding parameter 2 in Table 4.3 (left ventricle viscosity σ) is not well known, one can assume that the size of an individual may very well be related to the viscosity, as a larger individual may possess a larger heart with a correspondingly larger than normal tissue density. Thus, we are left with non-dimensional parameters 1 through 6 in Table 4.6 with which to carry out parameter estimation This corresponds to a total of 9 dimensional parameters, where ρ and L can be easily measured or estimated, and c_o can be solved for from the first dimensionless group, since the measurement of heart rate is a trivial matter. Using a grid discretized into four points along each axis, this results in a total of 4^6 or 4096 runs, which is still an overwhelming number of computations required to constuct an adequate parameter space. An additional simplification can be applied to reduce the number of runs to a reasonable number, and is outlined in the next section.

4.4 Determination of the Physiologic Operating Space / Construction of the Parameter Space

Although each parameter may be expected to traverse its physiological range, it is not diificult to appreciate that there may exist poins in the volume limited by the maximum and minimum values of each parameter which might be expected to yield unrealistic results. For instance, it is conceivable that heart rates can be found physiologically in the range of 50 - 150 BPM, and that peripheral resistance can also vary from half to double its nominal value. However, a combination of a heart rate of 150 BPM in conjunction with an SVR double of normal sould be expected to yield extremely high systemic blood pressures, well outside of the range of pressures compatible with life. One may take advantage of the simplicity and computational speed of the lumped parameter model of the circulation CVSIM, as described in Section 2.1, in order to study the relationship between the six selected parameters and the mean arterial pressure and cardiac output.

Modification of the lumped parameter model contained within *networks.c* allows us to easily construct runs for values of the parameters. These values are assigned by discretizing the six parameters into four points along each of their axes, bounded top and bottom by their expected *individual* physiologic range. Thus, 4^6 runs are performed at a computational rate of approximately 10 seconds/run to completely screen the parameter space. If one extracts only the runs that results in physiological mean arterial pressures

and cardiac outputs, then a much smaller number of runs is actually needed to describe the data obtained clinically. Assuming a range of mean arterial pressures from 50 mmHg to 90 mmHg, and cardiac outputs between 50 ml/sec and 110 ml/sec, then only 337 runs from the original 4096 runs fall within this category. These parameter values associated with these runs can be used as an input condition for constructing input files for *networks.c*: at 30 minutes a run, this results in approximately 1 week of calculation time, which was entirely more feasible than running 4096 runs over three months. Additionally, the screened runs provide mean arterial pressures which can be used as an initial condition for the systemic arterial pressure of the distributed model.

Thus, unique sets of the six parameters from Table 4.6 on a 4x4x4x4x4x4 grid were identified, where each axis was bounded by the maximum and minimum values selected for each individual parameter. These maximum and minimums are not the same as those used for the parameter screening, but are more limited to reflect the range of values that were seen in the data collected during the clinical study. Thus, heart rate ranged from 40 to 110 beats per minute, $E_{lv,max}$ ranged from 1000 to 15,000 dyn/cm^5, *EDV* ranged from 30 to 120 ml, ejection period ranged from 30% to 60%, *CVP* ranged from 0 to 30 mm Hg, and *SVR* ranged from 0.5 to 2.0 PRU (where 1 PRU = 1333.2 dyn-sec/cm^5. Each axis was discretized into four nodes, such that using the dimensionless scale from equation (4.2.1) each parameter could be assigned a dimensionless scale value of 0.0, 0.33, 0.66, and 1.0. The 337 gridpoints that fell within the physiological space were run and the data for the state variables as a function of time were stored for one steady-state cycle. The specified parameter set for each of the 337 runs were also stored for later processing.

Thus, screening of the physiological space has allowed us, in conjunction with the reduced non-dimensional parameter set, a means of accomplishing parameter estimation with reaonable effort. The data from the 337 runs of *networks.c* can be used to construct the *parameter space library* from which surrogates may be generated. Thus, the models *networks.c* is no longer required following construction of the library, unless in the future additional modifications are required to increase the accuracy of the estimation method, which is in turn a function of the accuracy of the simulations. Given a set of measured data from patients to be processed, one needs a method of computing an objective function for the estimation scheme which describes the goodness of fit between the computed pulse curves from each run and the patient data. This is discussed next in the following section.

4.5 The Parameter Estimation Scheme

4.5.1 Definition of an Objective Function

The use of the root mean square error as a method for characterizing the shape of the curve is useful for a first order study between the relationships between the pulse contours and the six parameters that have been identified as the primary influences on the morphometry of those curves. However, when applied to the estimation of six independent parameters, it is inappropriate for several reasons. Firstly, if the parameter estimation can be regarded as a linear problem where six unknowns are specified by a single number (the root mean square error), then the technique is immediately doomed to failure since one would be attemtpting to solve for 1 equation with 6 unkowns. Furthermore, one can easily envision a situation where two curves might be expected to give identical values of root mean square error when compared to the test curve of interest, and thus the possibility of many multiple solutions of "minimum error" exist. Clearly, minimization of a single parameter for error to solve for the unkown parameters is not appropriate.

A better approach to the problem would be to treat the solution for the unknown parameters as a series of six equations with six unkowns (the six hemodynamic parameters). If one considers the complexity of the pressure pulse, the conceiveably six independent characteristics or *features* of the pulse can be extracted and easily quantified. Such a process may be termed *feature extraction* to distinguish it from parameter estimation. A feature may take the form of any value that can be used to quantify the pulse. One must therefore make the assumption that each pulse is specific for each given set of parameter values, and therefore that six features are adequate to *uniquely* specify one pulse. Thus, the six equations become the dependance of each of the six features on the set of six parameters.

The easiest and most applicable set of features one could use are those indices that physicians may apply to a printout of the aortic pressure pulse using a ruler and a pen. These include mean pressure, peak systolic *dP/dt*, the slope of the pressure usptroke during early systole, and the systolic ejection period, or the time during the cardiac cycle that the left ventricle is actively contracting. One can also envision several more features that would be expected to change as a function of the hemodynamic parameters: the peak pressure, the pressure at end diastole, the *dP/dt* of the pressure during diastole, the time to peak pressure, the time to the dicrotic notch, and so forth. Additional features such as the amplitude and timing of secondary and reflected peaks may also be included, although a systematic measurement these features is difficult and unreliable, as not all pressure

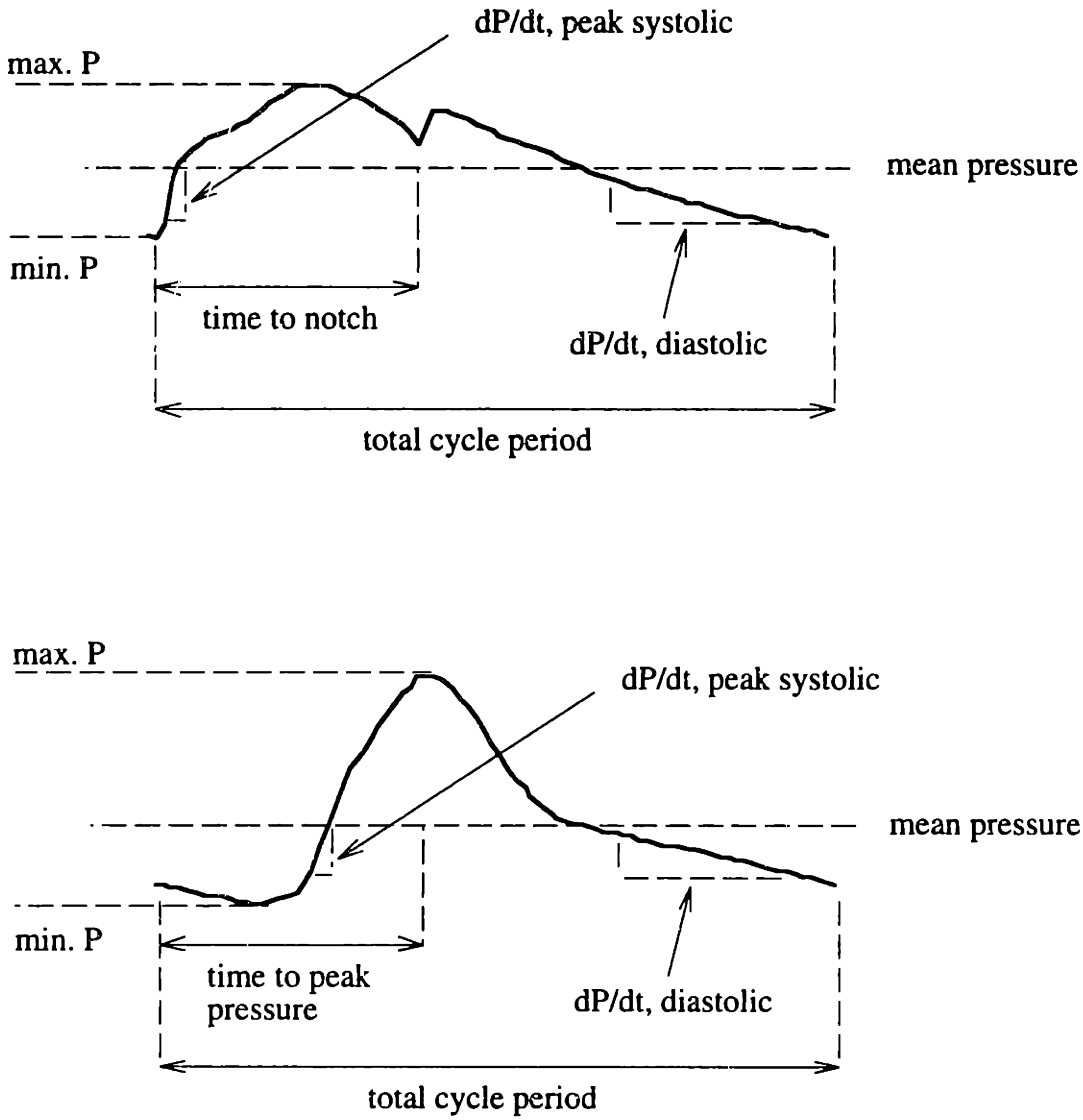

Figure 4.1. Features associated with a computed aortic pressure pulse (top) and a radial pressure pulse (bottom).

pulses measured at different times or different locations may contain such information. The velocity waves at various locations may also be analyzed in a similar manner, atlhough it is less clear what features may follow the alterations in parameter values. These features and the concept of "feature extraction" are summarized graphically in Figure 4.1.

At any rate, the features selected should be functions of the six parameters, and should be as independent from each other as possible. The feature of peak systolic *dP/dt*, for instance, should give more information about the left ventricular elastance than the peripheral resistance. Likewise, mean arterial pressure will yield more information regarding peripheral resistance than ejection period. Nonetheless, obvious pitfalls exist: the peak ventricular elastance may exhibit very similar effects on both the peak *dP/dt* and the peak pressure as does the end diastolic volume. Likewise, an increase in mean arterial pressure may be due to either an increase in peripheral resistance or an increase in central venous pressure. Thus, the concern of non-independent features leading to an ill-defined problem is very real, and will be addressed later when the results of the estimation scheme are reviewed.

As an additional cautionary note, the features extracted from different locations may give yield values that are not representative of the whole, but rather of the local hemodynamic conditions. For instance, the peak systolic *dP/dt* measured in the carotid artery may yield information about the strength of contraction of the heart: indeed, physicians use the peak systolic *dP/dt* as a qualitative index of left ventricular function. The peak systolic *dP/dt* measured in the radial artery, however, may contain less information about the venticular ejection and more about the mismatch of impedance in the periphery. The reason for this is that the rise in pulse pressure in the periphery is a function of not only the forward wave, but of the reflected waves superimposed on it as well.

One is not resistricted, however, to using physical features that are visually obtained. Any six indices used to define a specific curve can be used. For instance, it may be possible to uniquely define a specific curve through the first several coefficients from the Fourier decomposition of a curve. Other mathematical decompositions may be applied to extract similar information. The selection of the perfect set of features is a subject for future research, and will require a great deal of research and trial and error. For the purposes of this thesis, the set of features used are the following those outlined in Figure 4.1, applied to the radial artery and carotid artery pressures.

We choose to ignore the information that may be contained in the velocity waves, because of several reasons. Firstly, inaccuracies may arise from the observed differences

in velocities at various locations, which are more subject to larger variability than is the arterial pressure. Addtitionally, as mentioned previously it is difficult to develop a set of 6 useful features corresponding to one velocity wave. However, other feature definitions such as the frequency decomposition may prove of value when performing feature extraction on velocity data.

4.5.2 Shepard Routine for Construction of the Error Surrogate

We have up to this point demonstrated how to calculate sample "points" throughout the parameter space values of the objective function. However, sparse points in space are not adequate for describing the complete behavior of the objective function. One can, however, make an estimation of a continuous function that describes the relationship between the objective function and the set of parameter values. This continuous function is called a "surrogate", and acts as a model for the functional relationship that we wish to estimate. The surrogate is nothing more than a multi-dimensional quadratic interpolation of a field of sample points. An existing quadratic interpolation routine known as the Shepard quadratic interpolation can be implemented with little modification to the problem at hand. The original formulations were first described in detail by Franke and Nielson and Renka for the two and three dimensional cases (Franke and Nielson, 1990; Renka, 1988). Yesilyurt expanded the routine to arbitrary dimensions, following the formulation of Renka. Given that we have a dataset $\boldsymbol{D}$ which contains N input-output pairs:

$$\boldsymbol{D} = \{(\boldsymbol{p}_1, f_1),\ldots,(\boldsymbol{p}_1, f_N)\} \tag{4.4.1}$$

where f_j is the objective function for a given set of parameters $\boldsymbol{p}_j$, $j = 1...N$:

$$f_j = F(\boldsymbol{p}_j) \quad j = 1...N \tag{4.4.2}$$

and

$$\boldsymbol{p}_j = (p_j^1,\ldots,p_j^n) \tag{4.4.3}$$

where n is the total number of parameters in $\boldsymbol{p}$. Thus, an interpolation function of the following from may be defined:

$$\tilde{F}(\boldsymbol{p}) = \sum_{k=1}^{N} W_k(\boldsymbol{p}) Q_k(\boldsymbol{p}) \tag{4.4.4}$$

where $Q_k(\boldsymbol{p})$ are quadratic nodal functions acting as local approximations to $F(\boldsymbol{p})$ of the form:

$$Q_k(\boldsymbol{p}) = f_k + \left(\sum_{i=1}^{n} c_k^i (p^i - p_k^i) \right) + \sum_{j=1}^{n} \sum_{m=1}^{n} c_k^{\ell(j,m;n)} (p^j - p_k^j)(p^m - p_k^m) \qquad (4.4.5)$$

where:

$$\ell(j,m;n) = m + \sum_{p=1}^{j} (n - j + p) \qquad (4.4.6)$$

$$M \equiv \ell(n,n;n) = n + \frac{(n)(n+1)}{2} \qquad (4.4.7)$$

Equation (4.4.4) also contains the function $W_k(\boldsymbol{p})$ which are normalized inverse-distance weights given by:

$$W_k(\boldsymbol{p}) = \frac{W_k^*(\boldsymbol{p})}{\sum_{k=1}^{N} W_k^*(\boldsymbol{p})} \qquad (4.4.8)$$

where

$$W_k^*(\boldsymbol{p}) = \left[\frac{(R_w(\boldsymbol{p}_k) - d_k(\boldsymbol{p}))_+}{R_w(\boldsymbol{p}_k) d_k(\boldsymbol{p})} \right]^2 \qquad (4.4.9)$$

$$(R_w(\boldsymbol{p}_k) - d_k(\boldsymbol{p}))_+ = \begin{cases} R_w(\boldsymbol{p}_k) - d_k(\boldsymbol{p}) & \text{if} \quad d_k(\boldsymbol{p}) < R_w(\boldsymbol{p}_k) \\ 0 & \text{otherwise} \end{cases} \qquad (4.4.10)$$

In equation (4.4.9) $d_k(\boldsymbol{p})$ is the distance between points $\boldsymbol{p}_k$ and $\boldsymbol{p}$, and $R_w(\boldsymbol{p}_k)$ is the radius of influence about the node $\boldsymbol{p}_k$.

The Shepard routine can be implemented to first determine the coefficicients for the surrogate using the sample runs generated by the cardiovascular model. Thus, a set of parameters may be sent to the code, which then returns a single value based upon the interpolation between points, since any given set of parameters will lie in between grid points. The routine fits well into the context of feature extraction, since we are interested in determining the behavior of each feature as a function of the unkown parameters. Thus, from expression (4.4.2), the variable f_j corresponds to the jth feature, where j = 1...6 for the case of the solution for 6 features with 6 unkown parameters. The feature f is a function of the parameter set $\boldsymbol{p}$, and thus an approximation to the relationship between feature and parameter set can be constructed. Thus, what is done numerically is to extract a value for the desired feature from each individual library run, and to store that value

with the set of parameters that were used as the input for that run. One therefore obtains 337 parameter sets and 337 values for one feature, which is then sent to the Shepard routine for the construction of the surrogate function. This process is repeated for each feature that is defined. From the set of all possible defined features, 6 are then selected as the functions from which a simultaneous solution can be obtained. However, since the series of equations are only interpolations and cannot be solved for explicity, an iterative scheme must be implemented to determine the solution.

4.5.3 Minimization Routine

The commercial software package MATLAB contains a toolbox for optimization; of the available tools, a few proved to be extremely useful for iterative solution finding. Since MATLAB is capable of executing UNIX commands interactively, one may use six surrogates defined by the Shepard routine to act as a function for the minimizer tool. The tool passes a set of parameters to the user defined function containing the surrogate information, and is returned a value corresponding to the "closeness of fit." Since the assumption has been made that a set of features corresponds to one unique set of parameters only, then the best fit will be achieved when a set of parameters yields a set of feature values that is identical to the feature set of the test case (i.e. the patient data). In other words, if the feature set from the patient is a vector $\boldsymbol{F}_p$, and the set from the surrogates is also a vector $\boldsymbol{F}_s$, where $\boldsymbol{F}_s = \boldsymbol{F}_s(\boldsymbol{p})$, then $\boldsymbol{F}_p - \boldsymbol{F}_s$ becomes smaller than some predefined error (less than 5%), corresponding to the solution parameter set $\boldsymbol{p}$. This provides a systematic framework for the parameter estimation scheme which may now be validated using computed test cases.

4.5.4 Self-Test of Parameter Estimation Scheme

The parameter estimation scheme using feature extraction can be tested initially on a set of computed runs to determine the feasibility of the proposed scheme. Using the same modified *networks.c* used to construct the parameter library, an additional 18 test runs not identical to any grid points were performed with parameter sets which were selected at random. Each of the test runs falls under the constraint of the physiological space described above in Section 4.3 so that it is guaranteed to fall within the narrow boundaries of the parameter library space. Table 4.7 shows the values of the six parameters that were used as inputs for the 18 test cases. Included in this table at test case 19 is an actual grid point used to construct the library. This serves as a "standard" for the following validations, since one would expect the highest accuracy in estimation at this point. One may immediately use the test points to verify the accuracy of the

Table 4.7. Parameter values for the test cases. The 19th test case is an actual grid point.

#	HR (BPM)	$E_{lv,max}$ (dyn/cm^5)	EDV (ml)	Eject. Per. (%)	CVP (mm Hg)	SVR ($dyn-sec/cm^5$)
1	98	8755	77	44	13	1669
2	88	8796	73	45	16	1142
3	105	5424	77	31	2	1405
4	86	9234	105	39	20	1077
5	69	8253	93	43	6	966
6	89	7032	82	52	27	1223
7	43	7256	119	58	4	1907
8	92	7663	79	58	14	1351
9	84	4910	107	32	6	1566
10	93	11201	78	41	24	905
11	71	7446	85	52	18	1544
12	94	8240	85	55	0	1498
13	59	9479	116	58	22	1002
14	74	10381	118	46	20	864
15	62	10002	98	38	2	1008
16	109	8646	93	33	23	679
17	49	10740	118	49	0	1476
18	61	11454	97	40	5	1577
19	40	10332	120	30	30	626

Table 4.8. The extracted features from the 19 test cases for the left radial pressure pulse.

#	F1 P_{mean}, mm Hg	F2 DP, mm Hg	F3 dP/dt_{max}, mm Hg/sec	F4 time to max P, sec	F5 period, sec
1	94.00	34.69	620.29	0.23	0.60
2	66.73	32.11	517.68	0.25	0.67
3	57.45	29.50	570.42	0.22	0.56
4	90.39	47.23	713.73	0.25	0.69
5	55.66	40.48	569.88	0.29	0.86
6	84.08	31.67	466.87	0.26	0.66
7	89.53	58.84	527.33	0.35	1.38
8	79.90	31.17	453.94	0.27	0.65
9	77.07	39.28	660.63	0.24	0.70
10	71.54	36.67	618.35	0.24	0.64
11	84.95	41.37	510.93	0.28	0.84
12	85.50	35.83	544.25	0.26	0.63
13	82.81	55.50	560.68	0.33	1.00
14	83.65	53.79	663.72	0.29	0.80
15	55.85	49.11	678.12	0.28	0.95
16	62.53	33.82	657.71	0.22	0.54
17	80.72	66.71	696.60	0.32	1.22
18	87.07	58.94	757.52	0.27	0.97
19	56.58	53.77	644.68	0.33	1.50

Table 4.9. The estimated feature values for the 19 test cases (left radial pressure pulse) using the surrogate approximations.

#	F1 P_{mean}, mm Hg	F2 DP, mm Hg	F3 dP/dt_{max}, mm Hg/sec	F4 time to max P, sec	F5 period, sec
1	92.36	34.95	605.06	0.23	0.59
2	67.19	34.68	541.16	0.25	0.65
3	56.77	28.89	582.59	0.22	0.56
4	88.99	47.99	711.69	0.25	0.68
5	54.43	40.18	565.29	0.29	0.86
6	83.46	32.31	464.93	0.26	0.65
7	87.67	58.57	522.29	0.36	1.40
8	79.62	33.00	464.47	0.27	0.63
9	78.89	40.57	666.57	0.24	0.70
10	71.57	37.82	642.71	0.23	0.62
11	84.81	38.89	487.73	0.29	0.83
12	84.75	37.74	548.36	0.26	0.62
13	81.35	53.66	558.87	0.33	1.04
14	83.05	53.32	673.46	0.29	0.79
15	54.33	47.40	668.98	0.29	0.98
16	61.69	33.14	669.08	0.22	0.55
17	80.83	66.67	698.46	0.33	1.26
18	86.80	59.06	773.52	0.27	0.99
19	56.58	53.77	644.68	0.33	1.50

Table 4.10. Error between the actual and estimated feature values from Tables 4.8 and 4.9. The mean error for each feature surrogate is shown in the bottom row.

#	% Error, F1	% Error, F2	% Error, F3	% Error, F4	% Error, F5
1	1.8	0.8	2.5	1.7	1.8
2	0.7	8.0	4.5	1.2	3.4
3	1.2	2.1	2.1	1.1	0.1
4	1.5	1.6	0.3	1.0	1.4
5	2.2	0.8	0.8	0.4	0.4
6	0.7	2.0	0.4	1.2	1.1
7	2.1	0.5	1.0	1.6	1.7
8	0.3	5.9	2.3	1.0	2.8
9	2.4	3.3	0.9	1.3	0.4
10	0.0	3.2	3.9	3.3	2.5
11	0.2	6.0	4.5	2.2	1.5
12	0.9	5.3	0.8	1.1	1.1
13	1.8	3.3	0.3	0.4	3.6
14	0.7	0.9	1.5	0.1	1.8
15	2.7	3.5	1.3	3.0	2.9
16	1.3	2.0	1.7	0.9	1.0
17	0.1	0.1	0.3	2.2	3.7
18	0.3	0.2	2.1	0.3	2.5
19	0.0	0.0	0.0	0.0	0.0
MEAN	**1.1**	**2.6**	**1.6**	**1.3**	**1.8**

Shepard routine in approximating the behavior of a function, such as a feature, governed by the set of input parameters.

In Table 4.8, the values of five features are shown, which are extracted directly from the radial pressure tracings obtained from the test points. These features include the mean pressure, peak systolic pressure amplitude, maximum left-ventricle systolic *dP/dt*, time to peak pressure, and period of the cycle. Using the library of 337 grid points, surrogates were constructed using the Shepard routine to approximate each of the features as a function of the six input parameters. Thus, one may input the parameter values from Table 4.7 into the surrogates and extract five estimated feature values for each test case. These estimated values are shown in Table 4.9. A cross-comparison of values between Tables 4.8 and 4.9 shows very good agreement, and demonstrates the ability of the Shepard routine to approximate the behavior of multi-dimensional surfaces. Additionally, this validation also shows that a grid spacing of 4 divisions per axis is adequate to accurately model the feature dependance on input parameters. The percentage error between the actual and estimated feature values is shown in Table 4.10. The mean error for each feature is shown at the bottom of each column. Overall, the error is well under 5%, which allows us to assume that any difficulties associated with parameter estimation cannot be wholly attributed to surrogate inaccuracies. Also, it should be noted that the error associated with the gridpoint case 19 is exactly zero, as would be expected since the Shepard interpolation ensures that the approximated surface intersects at these locations precisely.

Parameter estimation may be carried out by specifying the features for the radial pressure pulse for both the parameter space surrogates and the 19 test cases. Since both the test cases and the library grid points were constructed with identical values for reference wavespeed C_o, length scales L, and blood density ρ, it is not required to normalize the parameters and the features for comparison purposes. Later when the estimation scheme is applied to patient data, this assumption cannot be made since it will be expected that each individual patient will have different values for each of these normalization parameters.

Thus, using the minimization scheme outlined above, a set of six parameters that provide the best fit solution that minimizes the difference between the estimated and actual feature values was obtained. The six features that were used were mean pressure P_{mean}, peak systolic dP/dt_{max}, peak systolic minus minimum diastolic pressure dP, peak systolic pressure, time to peak systolic pressure t_{peak}, and cycle period T. The results of the estimation for the radial pressure pulse are shown in Table 4.12, which can be compared with the actual test parameters in Table 4.11. The values in Table 4.11 were

Table 4.11. The 19 test case parameter values, represented in a dimensionless scale from 0.0 to 1.0.

#	P1	P2	P3	P4	P5	P6
1	0.83	0.55	0.52	0.48	0.44	0.55
2	0.69	0.56	0.48	0.52	0.52	0.27
3	0.93	0.32	0.52	0.07	0.07	0.41
4	0.65	0.59	0.83	0.33	0.68	0.24
5	0.42	0.52	0.70	0.45	0.20	0.18
6	0.70	0.43	0.58	0.74	0.92	0.32
7	0.05	0.45	0.99	0.94	0.14	0.68
8	0.74	0.48	0.54	0.96	0.45	0.39
9	0.63	0.28	0.86	0.07	0.22	0.50
10	0.75	0.73	0.54	0.37	0.81	0.15
11	0.44	0.46	0.61	0.76	0.62	0.49
12	0.77	0.52	0.61	0.84	0.00	0.46
13	0.27	0.61	0.95	0.94	0.73	0.20
14	0.49	0.67	0.97	0.54	0.68	0.13
15	0.32	0.64	0.76	0.29	0.08	0.20
16	0.99	0.55	0.69	0.10	0.76	0.03
17	0.13	0.70	0.97	0.66	0.01	0.45
18	0.31	0.75	0.75	0.35	0.16	0.51
19	0.00	0.67	1.00	0.00	1.00	0.00

Table 4.12. Results of 6 parameter estimation using radial artery pressure. The estimated parameters are given as P1 - P6, and the corresponding fractional error from the actual values (Table 4.11) given as E1 - E6. The mean error for each parameter is given at the bottom, in bold italics.

#	P1	P2	P3	P4	P5	P6	E1	E2	E3	E4	E5	E6
1	0.80	0.53	0.53	0.46	0.26	0.66	0.14	0.50	0.52	0.45	0.24	0.48
2	0.64	0.42	0.49	0.35	0.31	0.43	0.21	0.37	0.35	0.34	0.15	0.22
3	0.78	0.52	0.30	0.18	0.02	0.58	0.20	0.37	0.09	0.04	0.09	0.54
4	0.64	0.58	0.78	0.36	0.38	0.35	0.29	0.57	0.77	0.30	0.35	0.05
5	0.42	0.58	0.69	0.61	0.20	0.17	0.25	0.58	0.63	0.60	0.03	0.17
6	0.69	0.30	0.65	0.58	0.29	0.55	0.14	0.29	0.52	0.51	0.12	0.08
7	0.04	0.34	1.00	0.40	0.70	0.59	0.54	0.33	0.89	0.38	0.16	0.02
8	0.71	0.30	0.67	0.62	0.49	0.39	0.32	0.27	0.49	0.49	0.15	0.35
9	0.63	0.45	0.68	0.13	0.56	0.35	0.28	0.44	0.51	0.04	0.50	0.00
10	0.72	0.60	0.52	0.40	0.40	0.31	0.42	0.57	0.39	0.38	0.37	0.10
11	0.44	0.41	0.68	0.60	0.49	0.48	0.04	0.41	0.64	0.53	0.33	0.36
12	0.75	0.44	0.63	0.66	0.28	0.44	0.30	0.42	0.56	0.64	0.11	0.16
13	0.27	0.59	0.79	1.00	0.34	0.47	0.20	0.58	0.77	0.83	0.28	0.08
14	0.48	0.77	0.87	0.86	0.18	0.24	0.24	0.77	0.77	0.76	0.14	0.26
15	0.35	0.84	0.82	0.28	0.52	0.06	0.29	0.82	0.62	0.23	0.51	0.38
16	1.00	0.69	0.36	0.28	0.19	0.34	0.66	0.67	0.22	0.06	0.02	0.24
17	0.15	0.77	0.97	0.71	0.18	0.37	0.22	0.74	0.89	0.70	0.14	0.20
18	0.29	0.98	0.63	0.71	0.07	0.59	0.30	0.97	0.40	0.59	0.30	0.50
19	0.00	0.74	0.57	0.59	0.29	0.54	0.54	0.74	0.49	0.15	0.29	0.17
							0.29	***0.55***	***0.55***	***0.42***	***0.22***	***0.23***

Table 4.13. Results of 5 parameter estimation using radial artery pressure, specifying parameter 5 (CVP). The estimated parameters are given as P1 - P6, and the corresponding fractional error from the actual values (Table 4.11) given as E1 - E6. The mean error for each parameter is given at the bottom, in bold italics.

#	P1	P2	P3	P4	P5	P6	E1	E2	E3	E4	E5	E6
1	0.80	0.44	0.61	0.35	-	0.60	0.03	0.11	0.09	0.13	-	0.04
2	0.57	0.50	0.38	0.37	-	0.46	0.12	0.05	0.09	0.14	-	0.18
3	0.74	0.54	0.27	0.15	-	0.62	0.19	0.22	0.25	0.08	-	0.20
4	0.64	0.57	0.82	0.32	-	0.27	0.01	0.02	0.02	0.01	-	0.03
5	0.43	0.63	0.68	0.70	-	0.17	0.01	0.11	0.01	0.26	-	0.01
6	0.63	0.55	0.45	0.81	-	0.44	0.07	0.12	0.13	0.06	-	0.12
7	0.07	0.34	1.00	0.56	-	0.72	0.02	0.11	0.01	0.38	-	0.03
8	0.71	0.29	0.68	0.61	-	0.41	0.02	0.19	0.14	0.35	-	0.02
9	0.58	0.52	0.53	0.19	-	0.55	0.05	0.24	0.33	0.12	-	0.05
10	0.73	0.66	0.55	0.40	-	0.16	0.03	0.07	0.01	0.03	-	0.01
11	0.44	0.41	0.71	0.57	-	0.44	0.01	0.05	0.09	0.19	-	0.05
12	0.75	0.42	0.63	0.69	-	0.55	0.02	0.10	0.02	0.15	-	0.08
13	0.29	0.63	0.97	1.00	-	0.19	0.02	0.03	0.02	0.06	-	0.01
14	0.45	0.51	1.00	0.34	-	0.19	0.03	0.16	0.03	0.19	-	0.07
15	0.27	0.74	0.53	0.44	-	0.38	0.05	0.10	0.23	0.15	-	0.18
16	0.78	0.99	0.28	0.26	-	0.20	0.20	0.44	0.41	0.15	-	0.18
17	0.15	0.71	0.97	0.66	-	0.43	0.03	0.01	0.01	0.01	-	0.02
18	0.32	0.89	0.70	0.58	-	0.50	0.01	0.14	0.05	0.23	-	0.01
19	0.00	0.56	0.72	0.59	-	0.27	0.00	0.11	0.28	0.59	-	0.27
							0.05	***0.13***	***0.12***	***0.17***	-	***0.08***

Table 4.14. Results of 5 parameter estimation using carotid artery pressure, specifying parameter 5 (CVP). The estimated parameters are given as P1 - P6, and the corresponding fractional error from the actual values (Table 4.11) given as E1 - E6. The mean error for each parameter is given at the bottom, in bold italics.

#	P1	P2	P3	P4	P5	P6	E1	E2	E3	E4	E5	E6
1	0.76	0.68	0.44	0.52	-	0.66	0.07	0.13	0.09	0.03	-	0.10
2	0.66	0.54	0.50	0.49	-	0.26	0.03	0.02	0.02	0.03	-	0.01
3	0.91	0.41	0.45	0.06	-	0.44	0.02	0.09	0.07	0.01	-	0.02
4	0.64	0.81	0.68	0.46	-	0.27	0.02	0.22	0.15	0.13	-	0.03
5	0.42	0.64	0.64	0.50	-	0.19	0.00	0.13	0.06	0.06	-	0.01
6	0.67	0.48	0.55	0.80	-	0.33	0.03	0.05	0.03	0.05	-	0.02
7	0.06	0.41	1.00	0.86	-	0.72	0.01	0.03	0.01	0.08	-	0.03
8	0.70	0.48	0.54	0.98	-	0.40	0.04	0.01	0.00	0.02	-	0.01
9	0.52	0.65	0.46	0.28	-	0.57	0.11	0.37	0.39	0.21	-	0.07
10	0.73	1.00	0.44	0.46	-	0.17	0.02	0.27	0.09	0.09	-	0.02
11	0.45	0.34	0.73	0.61	-	0.45	0.01	0.12	0.11	0.14	-	0.04
12	0.76	0.31	0.83	0.72	-	0.42	0.01	0.21	0.22	0.12	-	0.05
13	0.29	0.52	1.00	0.86	-	0.21	0.01	0.08	0.05	0.07	-	0.01
14	0.47	0.59	1.00	0.51	-	0.15	0.02	0.08	0.03	0.03	-	0.02
15	0.34	0.77	0.72	0.29	-	0.21	0.03	0.13	0.04	0.00	-	0.00
16	0.83	0.44	0.76	0.00	-	0.00	0.16	0.11	0.06	0.10	-	0.02
17	0.15	0.76	0.95	0.65	-	0.44	0.02	0.06	0.02	0.02	-	0.01
18	0.32	0.86	0.72	0.40	-	0.49	0.02	0.11	0.03	0.05	-	0.02
19	0.14	0.85	1.00	0.00	-	0.00	0.14	0.18	0.00	0.00	-	0.00
							0.04	***0.13***	***0.08***	***0.07***	-	***0.03***

obtained from converting Table 4.7 to the dimensionless scale using equation (4.2.1) and the minimum and maxiumum values for each parameter in the parameter space, specified previously in Section 4.3. The absolute difference in values between the actual and the estimated parameters are given as an indication of the error in the last 6 columns labeled E1 - E6, and can be thought of as a percent error over the total range of excursion of each parameter (from 0.0 to 1.0). As can be seen, the error in attempting to estimate the six parameters from the radial pressure pulse is quite high. Several reasons may exist to explain the inaccuracies.

Of primary concern is the issue of the "well-defined" nature of the features, as a function of the 6 parameters. For instance, an increase in heart rate not only leads to a shortening of the cycle period, but also an increase in the mean pressure, as the cardiac output increases. An increase in end-diastolic volume may also lead to an increase in mean pressure in a manner indistinguishable from an increase in cardiac output. Likewise, an increase in systemic vascular resistance leads to an increase in mean pressure, which may be inseparable from an increase in central venous pressure, where trans-capillary pressure gradient is lowered, thus decreasing the outflow of blood into the venous circulation. Thus, the ambiguity in the feature functions may result in separate features behaving identically, thus leading to a larger number of unknowns than equations. This ill-defined nature can be somewhat overcome by specifying values for some of the parameters, and then solving for the remaining. By fixing central venous pressure, which is a hemodynamic parameter that is relatively easy to measure, the ambiguity between identical effects of peripheral resistance and venous pressure can be eliminated, leading subsequently to a more accurate estimation of the peripheral resistance. The parameter estimation for the 19 test cases can be repeated while specifying venous pressure and solving for 5 unknowns (the remaining parameters) using the features mean pressure, peak systolic dP/dt, peak minus minimum diastolic pressure, time to peak pressure. The result is shown for the radial artery pressure in Table 4.13. As can be seen, the mean error associated with parameter 6 (systemic vascular resistance) decreases from 23% to only 8% of the total range of excursion of parameter 6. This demonstrates the significant improvement in estimation technique that can be achieved by minimizing the ill-defined nature of the feature function behavior.

An additional improvement can be obtained using the estimation technique if one considers analyzing waves other than the radial pressure pulse. The carotid pressure pulse is one that is easily obtained in patients, and may be expected to reflect more the global behavior of the arterial system than the radial pulse, which is far more dependent on the local changes in vascular tone in the arm. The estimation for the 18 parameters,

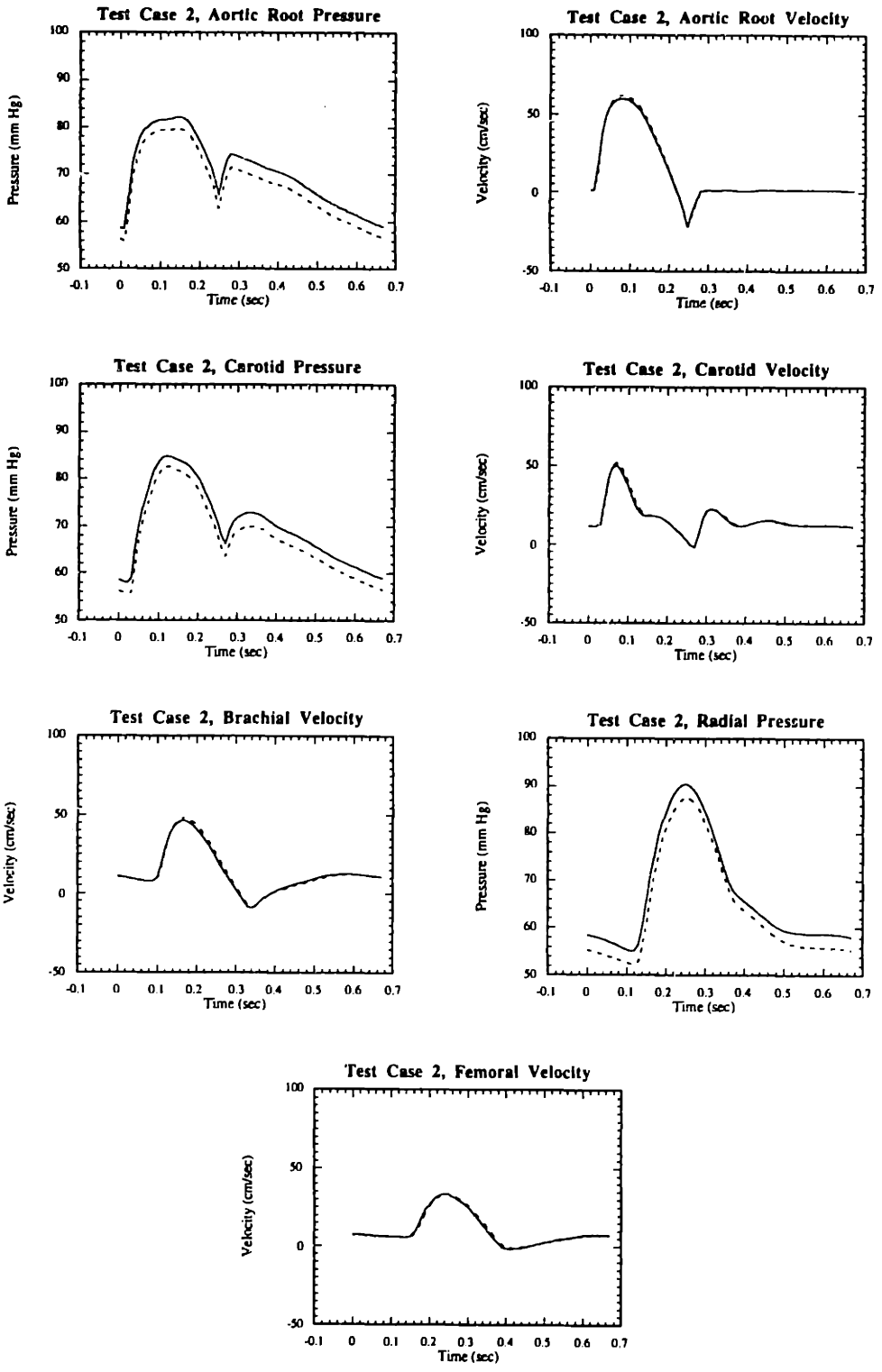

Figure 4.2. Comparison of actual test case outputs (solid line) and outputs generated from estimated parameters (dotted line), for test case #2, at several measurement locations.

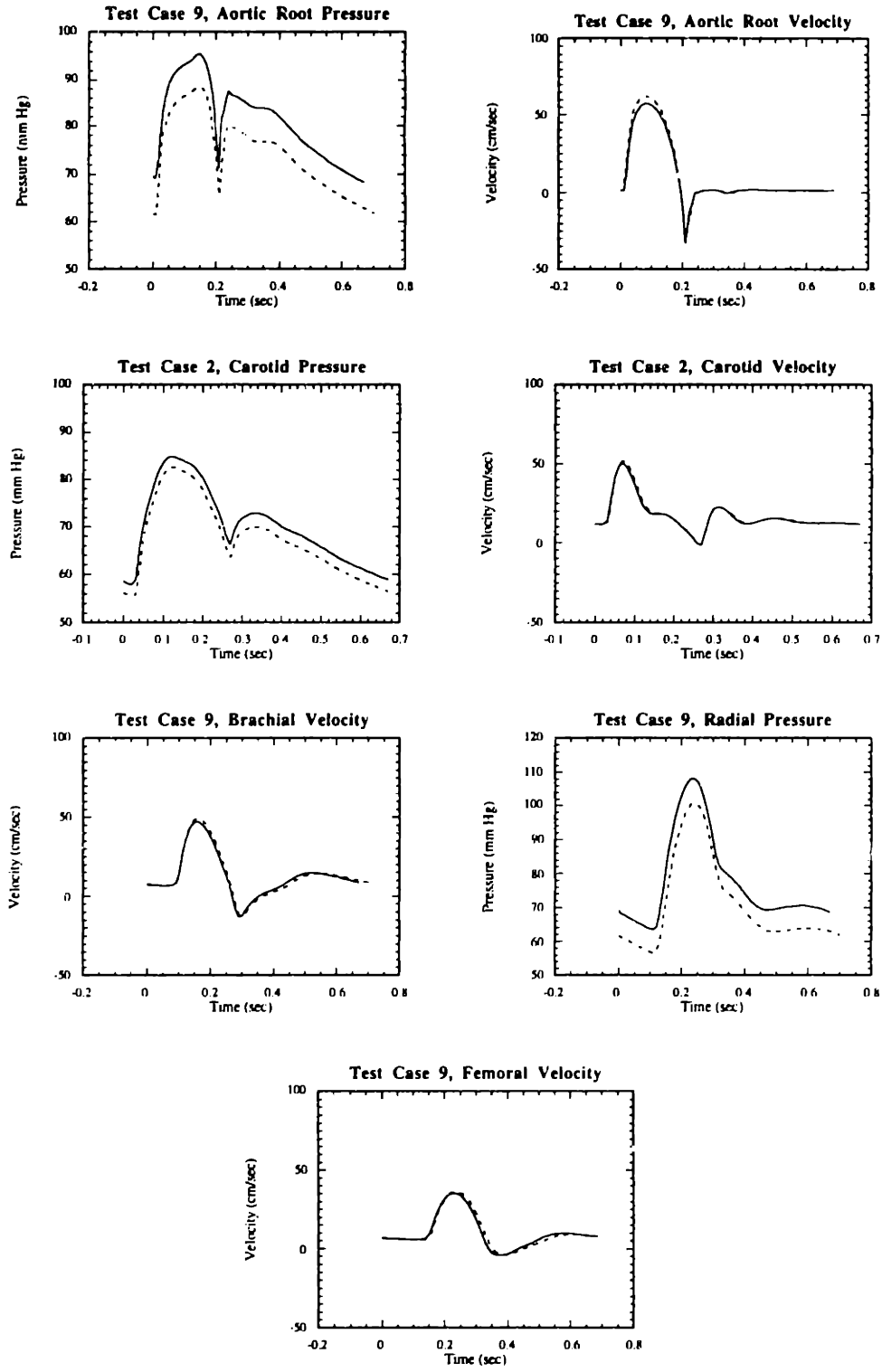

Figure 4.3. Comparison of actual test case outputs (solid line) and outputs generated from estimated parameters (dotted line), for test case #9, at several measurement locations.

using the same features as used for the radial pressure (except for the time to peak pressure, which is replaced by the time to the dichrotic notch), is repeated for the carotid pressure tracing and is shown in Table 4.14. As expected, a much more significant improvement in estimation of the peripheral resistance is achieved, where the mean error is only on the order of 3% of the total range of excursion of the parameter. Such a low error may allow for clinical measurement of the peripheral resistance, with only the carotid pressure pulse and mean central venous pressure.

Further study of the ill-defined nature of the problem can be made by comparing the output of the simulation for a given set of test paramters, and the output generated using the estimated parameters. In Table 4.14 for the carotid artery, one may observe that the result of test case 2 is extremely good, where all of the 5 estimated parameters are within 5% of the total range. In contrast, the result for test case 9 is quite poor. The output of the simulation run with parameters estimated for test case 2 are shown in Figure 4.2. As is shown, the slight error associated with the estimation is reflected as a small deviation mainly in mean pressure observed from the tracings for carotid pressure. It is also important to note that there is very little error associated with the velocity tracings, which again points out the difficulty one encounters when using velocity to carry out the parameter estimation. In comparison, the tracings for the "poor" estimation from test case 9 in Figure 4.3 shows a much larger amount of error in both pressure and time, although qualitatively the difference is not as substantial as one would expect from the large error obtained from the estimation technique. This demonstrates that several "near solutions" may exist within the vicinity of the true solution, and that the use of features related to absolute pressure values or slopes from pressure tracings are rather ambiguous, and do not provide the level of specificity required by the estimation scheme.

An additional study was performed by modifying the test of the parameter estimation against the 18 computed test cases as described above. The set of 6 parameters was again randomly selected within the physiological space. In addition, the remaining 21 parameters were also independently varied by selecting a random number between 0 and 1, to determine a value of the parameter based on the range of physiological values identical to those in the parameter screening. Parameter estimation was then applied to the new eighteen test cases, this time fixing both heart rate and central venous pressure (thus, only 4 parameters were estimated). The radial pressure pulse was used for feature extraction. These results are shown in Table 4.15. The same estimation with fixed HR and CVP was also applied to the previous 18 test cases with only the 6 governing parameters varied, for comparison. These results are shown in Table 4.16. The error between the two tables is shown in Table 4.17, with the mean error listed at the bottom in

Table 4.15 Results of parameter estimation for the 18 randomized test cases (27 parameters randomized). The parameters P2, P3, P4, and P6 were estimated. P1 and P5 were held fixed. The last column E represents the square of the RMS error between the predicted and actual feature values, and is an indication of solution convergence.

	P1	P2	P3	P4	*P5*	P6	E
1	*0.83*	0.09	0.80	0.62	*0.44*	0.64	0.03
2	*0.93*	0.49	0.00	0.77	*0.07*	0.50	2.57
3	*0.65*	0.39	0.00	0.77	*0.68*	0.71	0.32
4	*0.42*	1.00	0.17	0.09	*0.20*	0.40	0.53
5	*0.70*	0.03	0.66	0.39	*0.92*	0.09	0.02
6	*0.05*	0.06	0.97	0.30	*0.14*	1.00	0.09
7	*0.74*	0.00	0.39	0.77	*0.45*	0.71	4.00
8	*0.63*	0.38	0.11	0.78	*0.22*	0.48	0.07
9	*0.77*	0.00	0.51	0.59	*0.00*	0.46	0.07
10	*0.27*	1.00	0.99	0.05	*0.73*	0.49	0.35
11	*0.49*	0.21	0.88	0.53	*0.68*	0.04	0.02
12	*0.32*	0.29	0.01	0.72	*0.08*	0.57	0.14
13	*0.99*	0.87	0.41	1.00	*0.76*	0.04	0.41

Table 4.16. Results of parameter estimation for the 18 randomized test cases (6 parameters randomized). The parameters P2, P3, P4, and P6 were estimated. P1 and P5 were held fixed. The last column E represents the square of the RMS error between the predicted and actual feature values, and is an indication of solution convergence.

	P1	P2	P3	P4	*P5*	P6	E
1	*0.83*	0.52	0.58	0.44	*0.44*	0.54	0.00
2	*0.93*	0.71	0.23	0.50	*0.07*	0.51	0.02
3	*0.65*	0.74	0.70	0.46	*0.68*	0.27	0.00
4	*0.42*	0.52	0.66	0.43	*0.20*	0.22	0.00
5	*0.70*	0.45	0.56	0.76	*0.92*	0.33	0.00
6	*0.05*	0.29	1.00	0.39	*0.14*	0.96	0.03
7	*0.74*	0.24	0.74	0.52	*0.45*	0.40	0.01
8	*0.63*	0.64	0.49	0.35	*0.22*	0.48	0.01
9	*0.77*	0.40	0.69	0.67	*0.00*	0.48	0.01
10	*0.27*	0.61	1.00	0.99	*0.73*	0.19	0.00
11	*0.49*	0.47	1.00	0.25	*0.68*	0.19	0.04
12	*0.32*	0.58	0.75	0.15	*0.08*	0.24	0.02
13	*0.99*	0.68	0.55	0.21	*0.76*	0.06	0.00

Table 4.17. Error in parameter estimation between 13 of the 18 test cases with all 27 parameters randomized, and 13 of the 18 test cases with only 6 parameters randomized.

	E1	E2	E3	E4	*E5*	E6
1	-	0.43	0.23	0.18	-	0.10
2	-	0.22	0.23	0.26	-	0.01
3	-	0.34	0.70	0.32	-	0.43
4	-	0.48	0.49	0.35	-	0.18
5	-	0.42	0.10	0.37	-	0.24
6	-	0.23	0.03	0.09	-	0.04
7	-	0.24	0.34	0.25	-	0.31
8	-	0.26	0.39	0.43	-	0.00
9	-	0.40	0.18	0.09	-	0.02
10	-	0.39	0.01	0.94	-	0.30
11	-	0.26	0.12	0.28	-	0.15
12	-	0.29	0.74	0.57	-	0.34
13	-	0.18	0.14	0.79	-	0.02
	-	**0.32**	**0.28**	**0.38**	-	**0.17**

italics. Note that only 13 cases are shown for comparison. This is due to the fact that 5 runs with all of the parameters randomized were unable to converge upon a steady solution. Additionally, one may note that the error associated with the estimation of peripheral resistance (parameter 6) is the lowest, which is consistent with the results shown previously.

Full randomization of all of the parameters has generated test cases that lie outside of the physiological space. This is especially true with randomization of the parameter associated with left ventricular viscosity (parameter 2 in Table 4.3). Nonetheless, the same general trends with respect to estimation of the parameters P2, P3, and P4 remain consistent with the previous test summarized in Table 4.13. Thus, further investigation of the interrelationship between the parameters which lie in the middle band of influence from parameter screening in Table 4.2 is required. A physiological space based on the additional "non-essential" parameters must be defined. These include venticular viscosity, windkessel time constant (parameter 27 in Table 4.5), and bifurcation contraction coefficient, to name a few.

The system we outline here shows great promise in that by selecting carefully the correct combination of features and/or specifying those hemodynamic parameters that are easy to obtain, we are able to correctly estimate hemodynamic values to some level of accuracy, albeit only in the test case. The true test will be provided by how accurately the identification technique can estimate actual patient hemodynamic parameters, which is outlined in the next section.

Chapter 5

Clinical Study and Results

5.1 The Heart Failure Study

5.1.1 Introduction

The application of parameter estimation to a relevant clinical setting requires the identification of a disease process that can be easily captured by the physics contained in the numerical simulation. Since the model is based upon parameters that reflect global rather than local changes, it is appropriate to select a disease with global effects. Thus, for instance, the presence of an aortic stenosis would preclude parameter estimation through the present method, since no parameter exists to describe the placement of a single discontinuity among all of the possible positions in the arterial tree. Conversely, aging is a process where a global change in arterial wall stiffness is often seen (Karamanoglu, 1995), and is more applicable to the estimation technique.

Clinically, congestive heart failure is of importance, and can be easily modeled as an alteration of the parameter set defined in the previous chapter. Heart failure is a disease that merits much attention, as virtually all forms of heart disease eventually lead to heart failure. It is estimated that approximately 2 million people in the United States are currently being treated for this disease, while 400,000 new cases every year are diagnosed (Kannel, 1989). Mechanically, heart failure may be considered as a diminished capacity for the ventricles to pump blood, reflected by a decrease in myocardial contractility, as well as a generalized increase in systemic vascular resistance seen commonly in congestive heart failure (Zelis, 1982). The clinical manifestations of the disease vary widely from patient to patient, and thus parameter estimation may be expected to yield different results for each. Additionally, the majority of clinical interventions for heart failure make use of pharmaceuticals with clearly defined effects. These include reductions in ventricular afterload and changes in peripheral vascular resistance. In short, both heart failure and its clinical management may be modeled as specific mechanical changes, incorporated into a model of the circulation through altered model parameters. Complete success, however, may be difficult due to the many problems associated with

modeling a complex system. Despite these barriers, however, it is still fruitful to pursue the development of a model that has the potential to evolve into a useful clinical tool.

Standard treatment for the heart failure patient involves a wide range of pharmacological interventions, among which are vasodilation, or afterload reduction. The most commonly used vasodilator agents include captopril, an angiotensin-converting enzyme (ACE) inhibitor, and nitroglycerine, a potent smooth muscle relaxant. Both affect hemodynamics by decreasing systemic vascular resistance (SVR) through an increase in arteriolar cross-sectional area, secondary to reduction in arteriolar wall smooth muscle tone. Benefit to the patient is also achieved by reduction of venous tone, which further promotes capillary drainage and therefore also reduces the trans-arteriolar pressure gradient. The mechanical effect of vasodilation is to reduce the pressure load against which the left ventricle must push, therefore reducing the amount of work exerted by the myocardium. Furthermore, ACE-inhibitors reverse the inappropriate activation of the renin-angiotensin axis and angiotensin II, a vasoconstrictor, which is initiated by the kidneys in response to the falling cardiac output of the diseased heart.

Although the benefit of vasodilation in treating heart failure patients is clearly documented (Cohn, 1986; CONSENSUS, 1987; SOLVD, 1991), the mode of action is still in question. There exists some debate as to the whether afterload reduction agents affect SVR by purely altering smooth muscle tone, or whether some degree of reduction ventricular contractility is also present, possibly masked by the predominant effect of the lowered peripheral resistance (Cohn, 1993). It may be possible to introduce the pressure and flow tracings from an individual patient to the parameter estimation method, and extract values of systemic vascular resistance and peak ventricular elastance for the patient's state at the time that data is collected.

Thus, a clinical study was performed to collect hemodynamic data from heart failure patients through as many available methods as possible, before and immediately following the administration of a vasodilator. This study added a significant amount of clinical relevance to my dissertation work by allowing me to visualize how the hemodynamic parameter estimation scheme can be applied at the bedside. The study also provides data which aids in the validation of the numerical cardiovascular system model.

5.1.2 Study Procedures

The procedures of the study were as follows. Heart failure patients who were receiving afterload reducers (primarily captopril and sodium nitroprusside) and were constantly monitored hemodynamically through a central line, Swan-Ganz catheter, and/or an arterial line were used for this study. Since the numerical simulation contains

no provisions for mechanical assist, valvular insufficiency, or arterial stenosis, patients with these conditions were excluded from the study. All patients were obtained from the coronary care or stepdown units of the Brigham and Women's Hospital. Since the patients were selected from an environment where cardiovascular monitoring is paramount, a large amount of hemodynamic data were readily available. At the time of the study, it was not known exactly what pieces of information would eventually become useful in the context of parameter estimation. Consequently, an effort was made to obtain as much information as possible with the available equipment. Data were obtained by the use of Doppler ultrasound, which provides blood flow velocity measurements in the carotid, brachial, and/or the tibial and femoral arteries. The Doppler equipment used was a Toshiba ultrasound machine with a 7.5 MHz linear array transducer probe. In each patient, the artery of interest was identified using M-mode ultrasound with color Doppler overlay. Once the transducer was positioned over the artery, PW (Pulsed Wave) Doppler measurements were obtained over several cycles, with appropriate filter settings implemented to ensure quality signal capture. Additionally, the angle of incidence of the ultrasound beam was determined through existing measurement techniques built into the ultrasound unit. All images were recorded on videotape for later processing.

Pressure was measured in the radial and carotid arteries using a device known as a tonometer, which uses a piezoelectric transducer to detect artery wall deflection transmitted through the skin. The device (manufactured by PWV Medical of Australia), consists of a probe unit attached to an IBM compatible laptop computer containing the relevant software for data recording, calculation, and calibration. The software is capable of calculating the shape of the aortic pressure pulse by analysis of the pressure pulse recorded in a variety of possible measurement locations, including the radial, carotid, and brachial arteries.

Central venous, pulmonary arterial, pulmonary wedge, and arterial pressures were also monitored. Additionally, a number of normal healthy individuals were entered into this study. These subjects underwent Doppler ultrasound measurements of flow velocity in the brachial, tibial, and carotid arteries, and tonometer measurements of radial and carotid blood pressures. All measurements were performed by the author over a two month period. All test subjects gave informed consent to be used in this study. Permission from the Human Research Committee at Brigham and Women's Hospital was obtained for this purpose. The study outlined above also provided information that will aid in answering basic clinical questions regarding the action of afterload reduction in heart failure patients, and the mechanism by which heart function is improved. Thus, the data provided a means of applying the numerical cardiovascular simulation to a specific

clinical problem, as well attempting to reinforce the validity of the parameter estimation technique.

5.2 Results of Clinical Study With Parameter Estimation

In Chapter 4, the need for non-dimensionalization using a reference wavespeed, a characteristic length, and blood viscosity was motivated. Thus for parameter estimation of patient data, all features and parameters should be non-dimensionalized using equations (4.3.1) through (4.3.5) before comparison with model data, which is similarly non-dimensionalized. For a characteristic length, the assumption was made that the dimensions of the arterial system scale with the height of the individual. In this clinical study, measurements of patient height were recorded. For non-dimensionalization of the model data, a reference wavespeed of 462 cm/sec was assumed (aortic root reference wavespeed c_o), and a reference length of 165 cm, based on the total length of the aorta in the model, which corresponds roughly to an individual of that height. Additionally, the assumption may be made that fluid density in general changes little, so that specific densities for each patient need not be specified. Thus, what is left is the specification of wave speed as a requirement for non-dimensionalization of patient pressure and velocity waveforms for parameter estimation. Unfortunately, during the course of the clinical study, no attempt was made to gather information of this kind. Thus, in order to carry out the proposed parameter estimation scheme, it is necessary to make some broad assumptions which diminish the quality and reliability of the results described in this chapter. Nonetheless, the results are still telling of the capability of the model, and provides useful insight into what problems may be encountered in the future as the estimation scheme is refined.

An initial test of the parameter scheme may be carried out by first assuming that any variation in reference wavespeed and height from the standard case in the patients studied is insignificant. Since in the previous chapter it was shown that the peripheral resistance could be estimated to a fair degree using the radial artery pressure pulse, the same routine was applied using patient data and extracting a set of wave features for each of the patient's radial pressure pulse, before and after the vasodilator intervention. This was performed for six patients. The results of the estimation are summarized in Table 5.1, which also includes the clinical measurements of the patient's peripheral resistance, when available.

Table 5.1. Comparison of estimated versus measured systemic vascular resistance (SVR) for 6 patients, pre and post vasodilation.

#	patient	intervention status	SVR (measured) dyn-sec/cm^5	dimensionless SVR (estimated) dyn-sec/cm^5	SVR (estimated) dyn-sec/cm^5	factor= estimated SVR/ measured SVR
1	cr	pre	945.00	0.71	2086.46	2.21
		post	1410.00	0.55	1766.49	1.25
2	ea	pre	-	0.72	2106.46	-
		post	-	0.68	2026.46	-
3	lf	pre	1502.00	0.46	1586.51	1.06
		post	869.00	0.30	1266.54	1.46
4	mm	pre	1572.00	0.77	2206.45	1.40
		post	-	0.46	1586.51	-
5	ng	pre	1425.00	0.76	2186.45	1.53
		post	1155.00	0.82	2306.44	2.00
6	jp	pre	845.00	0.77	2210.65	2.62
		post	844.00	0.69	2046.46	2.42

One should note from Table 5.1 the predominantly high value of peripheral resistance that are estimated for each patient. This may be due to the fact that only pressure information obtained from a since pulse measured at one location was used to perform the estimation. Thus, the assumption that the behavior of the pressure and velocity waves in one location are dependent on each other may be inappropriate. It may be therefore necessary to include both pressure and velocity features simultaneously for the estimation procedures. One may also be able to include cardiac output as an alternative feature, such that the combination of both this feature and the mean pressure associated with one pulse together provide enough specificity to solve for peripheral resistance. The inaccuracy of the estimation technique with respect to left ventricle elastance and end-diastolic volume are most likely due to ill-conditioning of the simultaneous equations solved during estimation, which is directly connected to the selection of features. These features may not behave as independent functions of each other This problem may be surmounted by fixing one or more of the governing parameters (such as heart rate) with its known value.

In an effort to circumvent the lack of information regarding the patient reference wave speeds, an additional study was carried out on a handful of patient data sets. Thus, parameter estimation was performed by non-dimensionalizing the pressure wave (both for the absolute values of pressure and time) using the measured characteristic length, assuming a blood density of 1.04 g/cm^2, and three values of wavespeed at 300, 500, 700, and 900 cm/sec, again using the definitions in relationships (4.3.1) and (4.3.5) to carry out the normalization. Additionally, since the central venous pressures were measured for all patients, the parameters for heart rate and venous pressure may be fixed during estimation. The sensitivity of the parameter estimation to 2 patients are shown in Table 5.2, which shows the estimated values associated with each run. Note that the objective function is defined as:

$$\left[\left(\boldsymbol{F}_p - \boldsymbol{F}_s\right)\cdot\left(\boldsymbol{F}_p\right)^{-1}\right]^2 \tag{5.1}$$

where $\boldsymbol{F}_p$ is the patient feature set and $\boldsymbol{F}_s$ is the estimated surrogate feature set. From Table 5.2, it is easily apparent that the value of the objective function changes with the wavespeed. It may be possible that the lowest values of the objective function obtained at the 4 wave speeds correspond to values that are closest to those of the patient. However, without actual patient measurements of the wavespeed this hypothesis cannot be confirmed.

Table 5.2. Comparison of actual non-dimensional features from the radial pressure pulse, and non-dimensional features obtained from the surrogate for the set of converged parameters. Feature 1 is mean pressure, feature 2 is peak systolic *dP/dt*, feature 3 is peak pressure, and feature 4 is minimum diastolic pressure. All feature values are normalized with characteristic length, density, and wave speed.

patient		feature 1	feature 2	feature 3	feature 4	objective
lf	actual	0.242	0.321	0.197	0.707	
	estimated	0.236	0.326	0.199	0.707	0.031
ng	actual	0.416	0.510	0.389	0.680	
	estimated	0.416	0.510	0.389	0.680	0.003

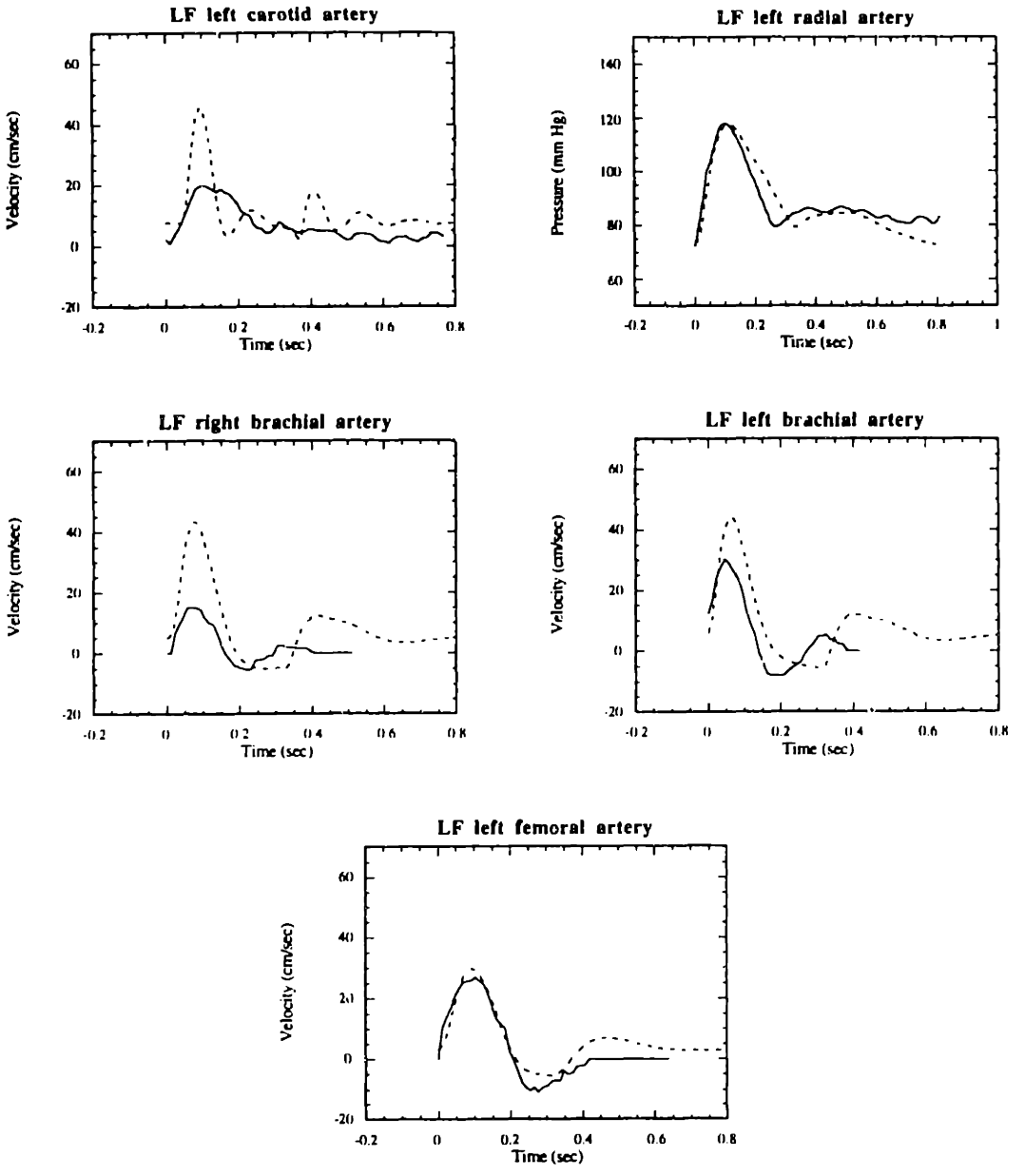

Figure 5.1. Comparison of patient data for patient LF (solid lines) with simulation (dotted lines) using matched features of the left radial artery pressure.

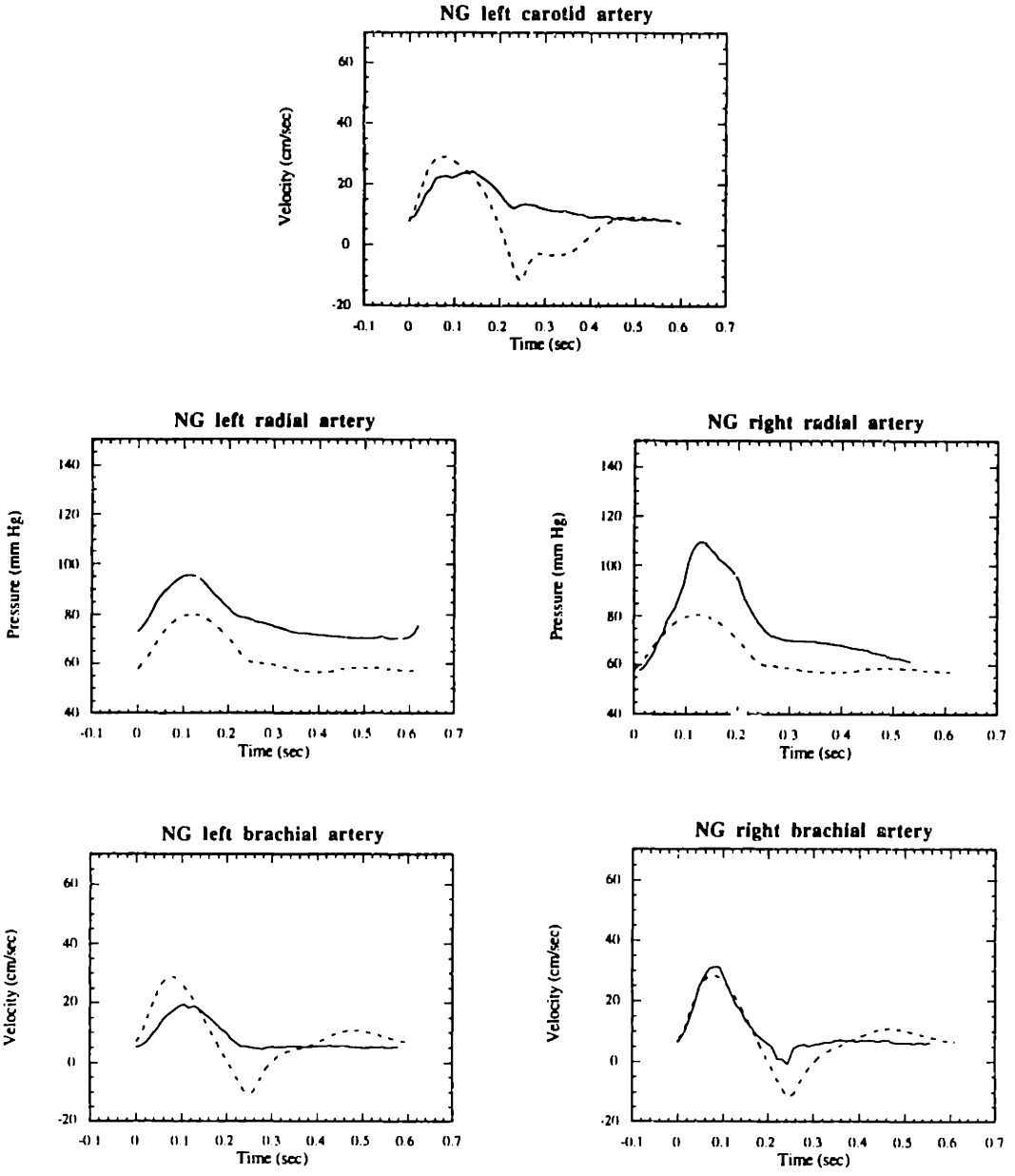

Figure 5.2. Comparison of patient data for patient NG (solid lines) with simulation (dotted lines) using matched features of the left radial artery pressure.

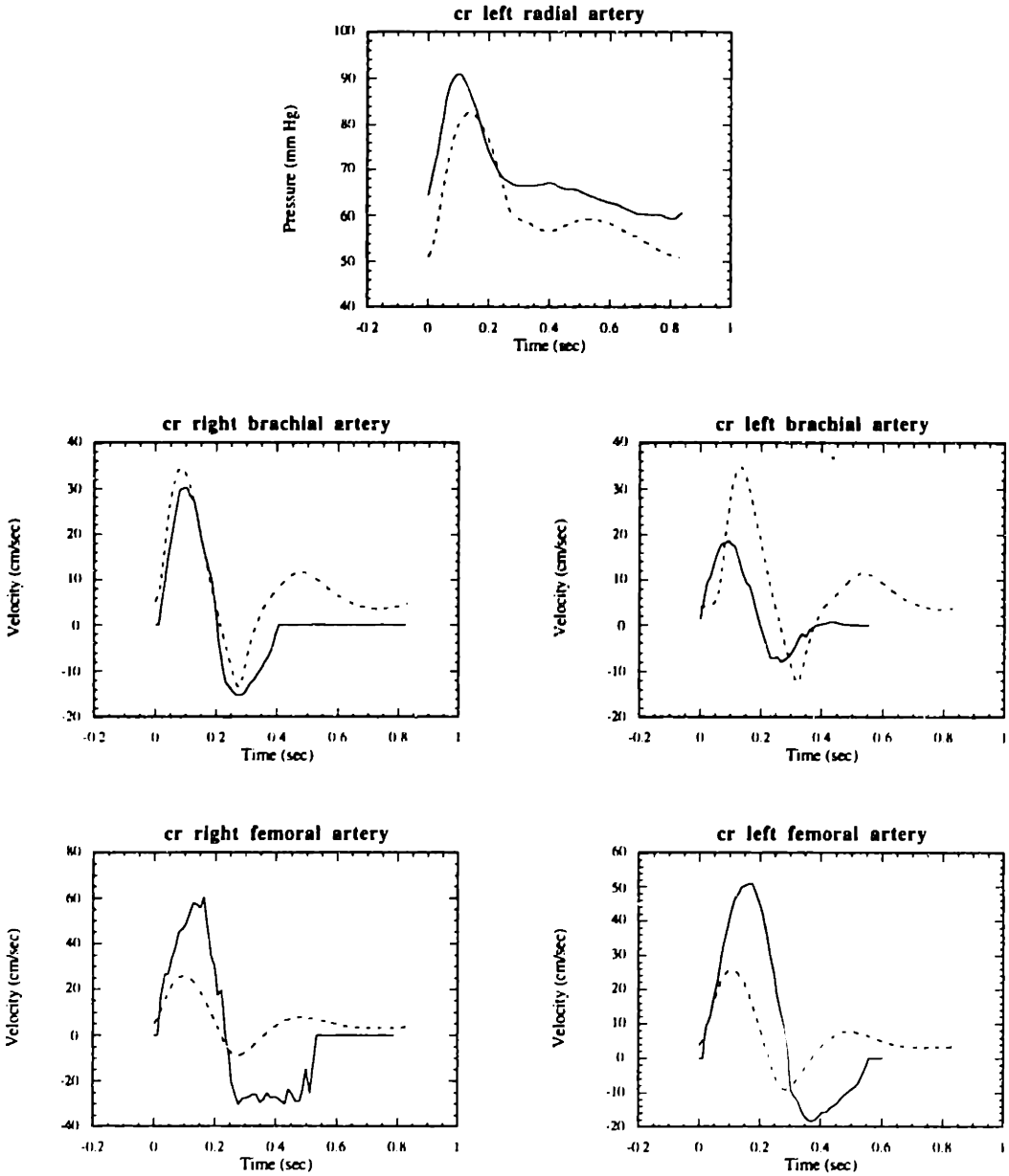

Figure 5.3. Comparison of patient data for patient CR *pre-intervention* (solid lines) with simulation (dotted lines) using matched features of the left radial artery pressure.

It should be noted that difficulties are potentially encountered when wavespeed values are increased, since non-dimensional values of pressure are reduced by the square of the ratio of patient wavespeed to model reference wavespeed. For instance, dimensional values of patient mean pressure close to 50 mm Hg cannot be non-dimensionalized using wave speeds higher than 462 cm/sec. This is because non-dimensional value of means pressure would result that are outside of the physiological range specified for reduction of the number of library grid points. Likewise, if the patient heart rate is close to 50 BPM, which is the bottom of the specified range of excursion for heart rate in the physiological space, the parameter estimation scheme will again fail for reference wave speeds higher than the standard values, since non-dimensional values of heart rate outside of the space would result. Clearly, the use of a limited range of test points within a "narrow" region representing physiologically possible values has some limitations when non-dimensionalization of features must be carried out.

The set of parameter values estimated from the features in Table 5.2 can be used to construct runs of *networks.c* for comparison of the numerically generated waves with that of the patients. Figures 5.1 through 5.3 show the results of this comparison, with one additional patient not listed in Table 5.2. The plots are very telling, in that the estimation technique is capable of determining parameters which result in numerical curves that are qualitatively similar to the patient waves used for the estimation procedure (in these cases, the radial artery pressure). However, the tracings obtained from other regions of the body are not as well matched, which indicates that some of the assumptions that were made for construction of the core simulation *networks.c* may have to be revised in the future. Furthermore, it is important to note that asymmetries exist within individuals. For instance, patient NG demonstrates a large asymmetry in radial pressure between the left and right arms. This asymmetry is not artifactual, and raises the issue of how disease processes or trauma that are able to cause asymmetric changes to vessel geometry or material properties may be incorporated into the model. Indeed, one must consider the possibility that each *individual* element within the system circulation is capable of changing independently of each other, which is a phenomenon that was neglected in the construction of the present estimation system. The core cardiovascular simulation is capable of handling such independent changes, but at a high computational cost.

It should be noted that there exists uncertainty regarding the accuracy of the measurement techniques employed in the clinical study. Human error is one source that is of significance, as often times accurate clinical measurements require a skilled, trained measurement taker. For instance, measurement of the peripheral resistance requires accurate estimations of the cardiac output, which in turn requires that the thermodilution

technique that is commonly used is carried out properly. Since during the clinical study these measurements were performed by the nurses, it can again be assumed that the values of peripheral resistance and cardiac output recorded are accurate. A potential source of error, however, may exist from the fact that thermodilution measurements did not always coincide in time with collection of the pressure and velocity measurements.

The Doppler ultrasound machines employed to record blood velocity tracings are also accurate when used by a skilled operator. Thus, another source of measurement error exists since the author learned the use of the devices weeks before the actual patient clinical data was collected. The conversion of the audio recording of the Doppler ultrasound to a single, averaged velocity wave also may carry inherent error that is not yet defined. Additionally, the tonometer is a device that gives reasonable recordings of the shape of the pressure wave, but unfortunately cannot provide absolute values pressure. This is provided by the measurement of blood pressure using a cuff, which again inherently contains error that is compounded lack of training on the part of the user. Furthermore, only two to three measurements of cuff pressure were recorded during the study performed on each patient. which were then averaged to provide an input for systolic and diastolic pressures at the brachial artery. A more accurate practice would have been to take a much larger number of pressure measurements, performed by two individual, so that errors due to human error and transient changes in the patient hemodynamics may be minimized. Thus, it is difficult at this point to make an accurate estimate of the total measurement error that may have been incurred through possible misuse of all of the devices involved in this study.

Analysis of the available patient data using the parameter estimation technique shows that a number of improvements can be made to the clinical study protocol. The clinical study served mainly to provide a framework with which to design the estimation scheme. Thus, it has been useful to perform the analyses described above in order to refine and hone the approach in preparation for future clinical studies, which are at present beyond the scope of this thesis.

Chapter 6

Discussion and Future Research

This thesis set out to develop a comprehensive model of the arterial system, and to demonstrate its flexibility by applying it to the problem of parameter estimation. Attempts at hemodynamic system identification have been previously made by other investigators. None, however, has used a systematic approach incorporating optimization algorithms to arrive at a promising scheme that has the power to extract as much information from non-invasive measurements as has been attempted here. The primary contribution of this work, then, was not to completely solve the problem by developing a foolproof method for hemodynamic parameter estimation, but rather to outline a possible direction that merits future investigation. The demonstration of the feasibility of hemodynamic parameter estimation is an appropriate ending point for this thesis, since it opens many new directions to pursue. To reiterate, the application of existing parameter estimation schemes to the problems of cardiovascular monitoring is quite novel, and as shown in this thesis required the construction of a numerical model of the cardiovascular system to meet the needs of the estimation scheme.

This chapter is split into two parts. Firstly the immediate directions for the parameter estimation scheme are discussed. Secondly, as we have alluded to throughout the thesis, the model is constructed to be flexible so that numerous applications may be investigated by its use. The demonstration of the potential feasibility of the hemodynamic parameter estimation is an important first step that opens up whole other directions for study.

6.1 Near Future Goals

The level at which the estimation is currently being performed has not been fully optimized. More sophisticated parameter estimation techniques are currently available in the engineering literature. This thesis has progressed to the level that most doubts about the eventual feasibility of hemodynamic parameter estimation have been dispelled.

However, the inability of the present system to successfully estimate parameters for patient data points to the need for future work.

Firstly, the collection of patient data must be significantly improved. Thus, a repeat study of the effect of vasodilator therapy on patient hemodynamics is essential. This will entail more detailed measurements of the carotid pressure wave through non-invasive means, as well as an estimation of the characteristic wavespeed of the individual, which was shown in Chapter 5 to be of enormous importance to the proposed estimation scheme. Tonometry proved to be ineffective in monitoring of the carotid pulse in heart failure patients, due to the weakness of the pulse which made isolation of the wave difficult. This problem was not encountered in normal healthy individuals where the carotid pulse is strong and brisk enough to result in high signal to noise ratios. An alternative method of monitoring the carotid pressure pulse would be to use a device which consists of a glass bulb containing a pressure transducer which can be firmly placed over a patient's neck using straps, thus providing a tight seal across which the pulse can be transmitted through the air filled bulb. This would provide measurements of carotid pressure waves that may prove invaluable in accurate application of the proposed parameter estimation scheme.

It is unfortunate that no attempt was made in the clinical study to estimate the reference wavespeed in the patients, which would have eliminated the need to perform the estimation technique using a range of arbitrary wavespeed values. Estimation of the wavespeed is easily accomplished by including the electrocardiogram with Doppler measurements, so that the signal may be used as a reference point in time with which to gate measurements. For instance, if both the Doppler signals from the carotid artery and the femoral artery are compared, the delay in time between the upstroke of the two waves can be estimated as the difference in lag times between the upstroke of the Q wave and the upstroke of the velocity wave, in both respective measurement locations. Given the distance between the two measurement locations, and the assumption that the wavespeed scales within an individual as it does in the model, the aortic root reference wavespeed can be easily determined. Thus, this wavespeed can be used to non-dimensionalize the patient data for insertion into the parameter estimation scheme.

In addition to these new measurements, the study will also require diligent measurements of cardiac output and systemic vascular resistance using the thermodilution technique for comparison purposes. Secondly, a larger sampling of patients will be required to statistically determine the accuracy of the estimation technique on human measurements. In order for the technique to demonstrate clinical effectiveness, it must be tested in the same manner as any drug or device, against a large sample population.

The application of patient data to the estimation technique also points to possible modification of the core model, *networks.c*. One notes that although pressure waves may be estimated and matched to some degree, the matching of velocity waves is somewhat less satisfactory. This is readily seen in Figures 5.1 through 5.2 for the patient pressure and velocity curves. To address this issue, one could define separate parameters that take into account flow to the head region, the arms, the legs and the splanchnic regions separately: this, for instance, would introduce an additional 4 parameters which would replace the one single parameter currently used to describe the peripheral resistance. Modifications such as these are beyond the scope of the present project, primarily due to the prohibitive number of parameter space runs required for higher parameter dimensions.

Because a large amount of velocity data were collected during the clinical study, the development of a feature extraction for velocity waves needs to be considered. It is yet to be determined if the mixing of features from both pressure and velocity waves will allow for more accurate resolution of certain parameters, since the combination of both pressure and flow yields information related to peripheral resistance, arterial impedance and compliance, and so forth. Again, further work needs to be performed in this area within the near future. In general, the present set of features used to carry out the parameter estimation is not well characterized nor well understood, for both pressure and velocity waves. Effort should be directed towards further developing a set of independent features that will boost the effectiveness of the present scheme.

Several additional qualitative adjustments may be made to the core program. Firstly, it has been noted on a number of grid points used to generate the parameter space the dichrotic notch is extremely large, to the point that the minimum pressure within the notch is below the minimum diastolic pressure within the cycle. This may be easily corrected by using a more conservative value of the volume of the sinus of valsalva, or the amount of fluid volume allowed to reflex at the root of the aorta before the numerical aortic root velocity is forced to zero. Furthermore, the down stroke of the aortic pressure wave during late systole appears qualitatively less steep than observed *in-vivo*. This may be corrected by making adjustments to the isovolumic left ventricle elastance curve, such that the downslope during late systole is made steeper. The shallow diastolic slope is also apparent in the computed elastance curves in Figure 2.13, when compared to the corresponding tracing from a patient in Figure 2.12-d. These adjustments to the core program are not essential within the framework of the parameter estimation scheme, but rather are cosmetic details which may detract from the overall quality of the generated data.

6.2 Additional Applications of the Computational Model.

Beyond parameter estimation, the model can be used to answer many other questions in cardiovascular mechanics. The model was originally developed with the intent of making it sufficiently flexible to be used to study the interaction between various forms of cardiac assist and the circulation. It would be a relatively simple matter to connect the existing code and couple it to an external model of a left ventricular assist device, for instance, where the model could provide a boundary condition of the device simulation. The model could in turn react to the simulated device, and the interactions studied with respect to the set of device parameters which correspond to the most optimal operating conditions. The effects of external counterpulsation may also be investigated using similar techniques. Model and assist device interaction may be studied by interfacing an existing commercial software package such as Simulink with the present core cardiovascular model.

Since we have included the baroreflex loop in the model, the opportunity exists to study the effects of cardiovascular control. For the purposes of parameter estimation, the reflex was found to be unnecessary, and thus was not developed or tested beyond what has been presented in this thesis. Several opportunities to study the relationship between the hemodynamics and physiological control exist. For instance, since gravity may be applied as an external force through the equations of motion, the effects of flight and space travel on the cardiovascular system may be studied with relative ease and little modification to the present code. The baroreflex has not been thoroughly characterized and validated at this point in time. Nonetheless, little work remains to obtain a working cardiovascular model with baroreflex control.

Many times it has been suggested that the use of animals may help in providing data to help refine the contents of this thesis in a way that human patient data cannot. Animal studies may indeed prove to be useful in refining the estimation scheme, as well as improving the core model. With animals, it is much easier to account for all of the pharmaceutical interventions which may be applied independently, allowing for easy characterization of the changes in hemodynamics from baseline. As has been seen from the clinical study, it is extremely difficult to locate a large enough sample of patients with well-defined interventions. Animal models will allow for a large enough statistical sampling of individual cases where the physiological conditions may be easily controlled. Additionally, a more accurate study may be done of the geometry and material properties

of the arterial tree in a number of sacrificed animals, thereby increasing further the potential accuracy of the technique as applied to that specific animal model.

This chapter has merely outlined what I perceive to be the most immediate and obvious applications of the thesis work. It is entirely possible that many additional applications may exist that have not been realized by myself, although others may find hidden potential. In general, there has been historically a push to obtain a system that is capable of extracting from an arterial pulse the important hemodynamic parameters that are necessary for the clinician to design therapeutic strategies for cardiovascular disease. I believe that this thesis is the first serious attempt to do so by incorporating a sophisticated model of the arterial system with engineering system identification techniques in order to approach the problem. No other previous work has attempted to approach the problem from this direction, and none has shown as much promise for future success. The value of a fully operating hemodynamic estimation system based on non- invasive patient measurements is clear: the majority of present hemodynamic monitoring methods requires the use of minimally invasive techniques which carry inherent risks and costs that can be eliminated using the proposed estimation scheme. To summarize, this technique will allow for *continuous* monitoring of hemodynamic parameters with little to no risk of injury to the patient. I would like to close by saying that it is my sincere hope that this work will continue to be built upon, either by myself or others, to develop a system that may one day become commonplace in the clinical setting.

Bibliography

Anliker, M., Histand, M.B., Ogden, E. *(a)* Dispersion and Attenuation of Small Artificial Pressure Waves in the Canine Aorta. *Circulation Research*, Vol. 23: 539:551; *(b)* Transmission Characteristics of Axial Waves in Blood Vessels. *Journal of Biomechanics*, Vol. 1: 235-246, 1968.

Avolio, A.P. Multi-branched model of the human arterial system. *Med. Biol. Eng. Comput.* 18, 709-18, 1980.

Berger, D.S., Li, J.K-J, Noordergraf, A. Differential effects of wave reflections and peripheral resistance on aortic blood pressure: a model-based study. *Am. J. Physiol.* 266 (*Heart Circ. Physiol.* 35): H1626-H1642, 1994.

Berger, D.S., Li, J.K-J, Noordergraf, A. Arterial Wave Propagation Phenomena, Ventricular Work, and Power Dissipation. *Annals of Biomedical Engineering*. Vol. 23, 804-811, 1995.

Berger, R.D., Saul, J.P., Cohen, R.J. Transfer function analysis of autonomic regulation I. Canine atrial rate response. *American Journal of Physiology*, 256 (Heart Circulation Physiology 25): H142-52, 1989.

Berne, R.M., Levy, M.N. Cardiovascular Physiology 6th ed. Mosby Year Book, St. Louis, 1992.

Bharadvaj, B.K., Mabon, R.F., Giddens, D.P. Steady Flow in a Model of the Human Carotid Bifurcation. Part I - Flow Visualization. *J. Biomechanics*. Vol. 15, No. 5, 198, 349-362, 1982.

Bharadvaj, B.K., Mabon, R.F., Giddens, D.P. Steady Flow in a Model of the Human Carotid Bifurcation. Part II - Laser-Doppler Anemometer Measurements. *J. Biomechanics*. Vol. 15, No. 5, 368-378, 1982

Brin, K.P., Yin, F.C.P. Reflections in patients with heart failure. *Annals of Biomedical Engineering*, Vol. 12, 135-150, 1984.

Cappello, A., Gnudi, G., Lamberti, C. Identification of the Three-Element Windkessel Model Incorporating a Pressure-Dependant Compliance. *Annals of Biomedical Engineering*. Vol. 23, 164-177, 1995.

Clemente, C.D. Anatomy: A Regional Atlas of the Human Body 3rd Ed. Urban and Schwarzenberg, Baltimore: 1997.

Cochrane, T. Simple model of circulatory system dynamics including heart valve mechanics. *J. Biomed. Eng.*, Vol. 13, 335-340, July 1991.

Cohn, J.N. Efficacy of Vasodilators in the Treatment of Heart Failure. *JACC* Vol. 22, No. 4 (Suppl. A), October, 135A-138A, 1993.

Cohn, J.N., Archibald, D.G., Ziesche, S., et al.: Effect of vasodilator therapy on mortality in chronic congestive heart failure: Results of a Veterans Administration Cooperative Study. N. Engl. J. Med. 314:1547, 1986.

Collins, J.M., Shapiro, A.H., Kimmel, E., and Kamm, R.D. The Steady Expiratory Pressure-Flow Relation in a Model Pulmonary Bifurcation. *Journal of Biomechanical Engineering*. 115:299-305, 1993.

The CONSENSUS Trial Group: Effects of enalapril on mortality in severe congestive heart failure: Results of the Cooperative North Scandinavian Enalapril Survival Study. N. Engl. J. Med. 316:1429, 1987.

Davis, T.L. Teaching Physiology Through Interactive Simulation of Hemodynamics. M.S. thesis, Dept. of Electrical Engineering, Massachusetts Institute of Technology: February, 1991.

DeBoer, R.W., Karemaker, J.M., and Strackee, J. Hemodynamic fluctuations and baroreflex sensitivity in humans: A beat-to-beat model. *American Journal of Physiology*, 253(Heart Circulation Physiology 22):H680-H689, 1987.

Feigenbaum, H. Echocardiography, 4th ed. Philadelphia: Lea and Febiger, 1994.

Franke, R., Nielson, G.M. Scattered data interpolation and applications: A tutorial and study, in: H. Hagen and D. Roller, eds., Geometric Modelling: Methods and Applications. (131-160). Springer-Verlag, Berlin, 1990.

Fung, Y.C. Stress-strain-history relations of soft tissues in simple elongation. In: Biomechanics, its foundations and objectives. Y.C. Fung, N. Perrone, M. Anliker (eds.), Prentice-Hall, Englewood Cliffs, 1972.

Giddens, D.P., Zarins, C.K., Glagov, S The Role of Fluid Mechanics in the Localization and Detection of Atherosclerosis. Journal of Biomedical Engineering. Vol. 115, 588-594, November, 1993.

Groden, D.L. Vasodilator Therapy for Congestive Heart Failure: Lessons From Mortality Trials. *Arch. Intern. Med.*, Vol. 153: 445:454, Feb. 22, 1993.

Helal, M.A., Watts, K.C., Marble, A.E. Hydrodynamic simulation of arterial networks which include compliant and rigid bypass grafts. *J. Biomechanics*, Vol. 27, No. 3, 277-287, 1994.

Holenstein, R., Niederer, P., and Anliker, M. A Viscoelastic Model for Use in Predicting Arterial Pulse Waves. *Journal of Biomechanical Engineering*. 102, 318-325, 1980.

Kamiya, A., Bukhari, R., and Togawa, T. Adaptive regulation of wall shear stress optimizing vascular tree function. *Bull. Math. Biol.* 46(1):127-137, 1984.

Kamm, R.D. A Study of External Pneumatic Compression for the Prevention of Deep Venous Thrombosis. Ph.D. thesis, Dept. of Mechanical Engineering, Massachusetts Institute of Technology: May 1977.

Kamm, R.D. Bioengineering Studies of Periodic External Compression as Prophylaxis Against Deep Vein Thrombosis - Part I: Numerical Studies. *Journal of Biomechanical Engineering*, Vol. 104, 87-95, May 1982.

Kannel, W.B. Epidemiological aspects of heart failure. in Weber, K.T. (ed.) Heart Failure: Current Concepts and Management. Cardiology Clinics Series 7/1, Philadelphia, W.B. Saunders Co, 1989.

Karamanoglu, M., Gallagher, D.E., Avolio, A.P., O'Rourke, M.F. Pressure wave propagation in a multibranched model of the human upper limb. *Am. J. Physiol.* 269 (*Heart Circ. Physiol.* 38): H1363-H1369, 1995.

Kassab, G.S., Fung, Y.C. The Pattern of Coronary Arteriolar Bifurcations and the Uniform Shear Hypothesis. *Annals of Biomedical Engineering.* Vol. 23, 13-20, 1995.

Kimmel, E., Kamm, R.D., and Shapiro, A.H. Numerical Solutions for Steady and Unsteady Flow in a Model of the Pulmonary Airways. *Journal of Biomechanical Engineering.* 110(292-299), 1988.

Ku, D.N., Giddens, D.P., Zarins, C.K., Glagov, S. Pulsatile flow and atherosclerosis in the human carotid bifurcation, positive correlation between plaque location and low oscillating shear stress. *Arteriosclerosis.* 5:293-302, 1989.

Lueptow, R.M., Karlen, J.M., Kamm, R.D., Shapiro, A.H. Circulatory Model Studies of External Cardiac Assist by Counterpulsation. Cardiovascular Research, Vol. 15, No. 8, 443-455, August 1981.

LaBarbera, M. Principles of Design of Fluid Transport Systems in Zoology. *Science*, Vol. 249, 992-1000, August 1990.

Laskey, W.K., et al. Estimation of total systemic arterial compliance in humans. *J. Appl. Physiol.* 69(1):112-119, 1990.

Laskey, W.K., Kussmaul, W.G. Arterial wave reflection in heart failure. *Circulation* 75, No. 4, 711-722, 1987.

Latham, R.D. Technique of micromanometric catheterization of the descending aorta in man: A method to study regional arterial dynamics. *Heart Vessels* 3:166-169, 1987.

Lee, C.C., Mark, R.G. Analysis of Arterial Waves by the Single-Pulse-Response Method. IEEE Transactions on Biomedical Engineering, Vol. 40, No. 8, 833-836, August 1993.

Li, J.K-J. Time Domain Resolution of Forward and Reflected Waves in the Aorta. *IEEE Transactions on Biomedical Engineering*, Vol. BME-33, No. 8, 783-785, August, 1986.

Lighthill, J. Waves in Fluids. Cambridge Univ. Press, Cambridge, 1978.

McDonald, D.A. Blood Flow in Arteries, 2nd Ed.. The Williams and Wilkins Co., Baltimore, 1974.

McKay, R.G., et al. Left ventricular pressure-volume diagrams and end-systolic pressure-volume relations in human beings. *J. Am. Coll. Cardiol.* 3:301, 1984.

McMahon, T.A., Clark, C., Murthy, V.S., Shapiro, A.H. Intra-Aortic Balloon Experiments in a Lumped-Element Hydraulic Model of the Circulation. J. *Biomechanics*, Vol. 4, 335-350, 1971.

Mills, C.J., et al. Pressure-flow relationships and vascular impedance in man. Cardiovascular Research, 4, 405-417, 1970.

Mirsky, I. *Elastic Properties of the myocardium: A quantitative approach with physiological and clinical applications.* In Berne, R.M. ed., Handbook of Physiology, Section 2: The Cardiovascular System, Vol. I, 2nd Ed., Chap. 14 (497-531). American Physiological Society, Bethesda Maryland, 1979.

Moore, J.E., Ku, D.N. Pulsatile Velocity Measurements in a Model of the Human Abdominal Aorta Under Resting Conditions. *Journal of Biomechanical Engineering*, Vol. 116, 337-346, August 1994.

Moore, J.E., Ku, D.N. , Zarins, C.K., Glagov, S. Pulsatile Flow Visualization in the Abdominal Aorta Under Differing Physiologic Conditions: Implications for Increased Susceptibility to Atherosclerosis. *Journal of Biomechanical Engineering*, Vol. 114, August, 1992: 391-397.

Nichols, W.W., Conti, C.R., Walker, W.E., Milnor, W.R. Input Impedance of the Systemic Circulation in Man. *Circulation Research.* Vol. 40, No. 5, May 1977, 451-458.

Niederer, P. Damping mechanisms and shock transitions in the human arterial tree. *Journal of Applied Mathematics and Physics.* 36, 204-220, 1985.

Niederer, P., Schilt, W. Experimental and theoretical modelling of intra-aortic balloon pump operation. *Med. Biol. Eng. Comput.* 26, 167-174, March 1988.

O'Rourke, M.F., Kelly, R., Avolio, A. The Arterial Pulse. Lea and Febiger, Philadelphia, 1992.

Otto, J., Paraschivoiu, M. , Yesilyurt, S., Patera, A.T. Bayesian-Validated Computer-Simulation Surrogates for Optimization and Design. In publication, M.I.T. Fluid Mechanics Laboratory.

Patel, D.J., Greenfield, J.C., Austen, W.G., Morrow, A.G., Fry, D.L. Pressure-flow relationships in the ascending aorta and femoral artery of man. *J. Appl. Physiol.* 20(3):459-463, 1965.

Pedley, T.J. The Fluid Mechanics of Large Blood Vessels. Cambridge University Press, 1980.

Pedley, T.J., Schroter, R.C. and Sudlow, M.F. Energy losses and pressure drop in models of human airways. Resp. Physiol., 9:371-386, 1970.

Perktold, K., Resch, M. Numerical flow studies in human carotid artery bifurcations: basic discussion of the geometric factor in atherogenesis. J. Biomed. Eng., Vol. 12, 111-123, March 1990.

Raines, J.K. Diagnoosis and Analysis of Arteriosclerosis in Lower Limbs from the Arterial Pressure Pulse. Ph.D. thesis, Dept. of Mechanical Engineering, Massachusetts Institute of Technology: 1972.

Renka, R.L. Algorithm 660: QSHEP2D: Quadratic Shepard method for bivariate interpolation of scattered data. *ACM TOMS*, 14, (149-150), 1988.

Sah, R., Moody, G. *User manual for the Cardiovascular Simulator,* 1985.

Shapiro, A.H. Steady Flow in Collapsible Tubes. *Journal of Biomechanical Engineering*, Vol. 99, 126-147, August 1977.

Shin, J. Numerical Modeling of Forced Expiratory Flow in a Human Lung. M.S. thesis, Dept. of Mechanical Engineering, Massachusetts Institute of Technology: February, 1992.

The SOLVD investigators: Effect of the angiotensin converting enzyme enalapril on survival in patients with reduced left ventricular ejection fraction and congestive heart failure. N. Engl. J. Med. 325:293, 1991.

Soroff, H.S., Hui, J., Giron, F. Current Status of Counterpulsation. Critical Care Clinics, Vol. 2, No. 2, 277-295, April 1986.

Stettler, J.C., Niederer, P. and Anliker, M. Theoretical analysis of arterial hemodynamics including the influence of bifurcations. Part I: Mathematical Model and Prediction of Normal Pulse Patterns. *Annals of Biomedical Engineering*. 9(145-164), 1981.

Stettler, J.C., Niederer, P. and Anliker, M. Nonlinear mathematical models of the arterial system: effects of bifurcations, wall viscoelasticity, stenoses, and counterpulsation on pressure and flow pulses. From Handbook of Bioengineering. Eds. Skalak and Chien, McGraw Hill 1987.

Suga, H. and Sagawa, K. Instantaneous Pressure-Volume Relationships and Their Ratio in the Excised, Supported Canine Left Ventricle. *Circulation Research*, Vol 35, July 1974.

Suga, H., Sagawa, K., Demer, L. Determinants of Instantaneous Pressure in Canine Left Ventricle: Time and Volume Specification. *Circ. Res.* 46: 256-263, 1980.

Symposium on Cardiovascular Physiology. Presented by the NASA Center for Space Cardiovascular Physiology in the Harvard-M.I.T. Division of Health Sciences and Technology. November 17 1994.

Taylor, T.W., Yamaguchi, T. Three-Dimensional Simulation of Blood Flow in an Abdominal Aortic Aneurysm - Steady and Unsteady Flow Cases. *J. Biomech Eng*, Vol. 116: 89-97, February 1994

Tsurata, H., Sato, T., Ikeda, N. Mathematical model of cardiovascular mechanics for diagnostic analysis and treatment of heart failure: Part 1 model description and theoretical analysis. *Med. & Biol. Eng. & Comput.*, 1994, 32, 3-11.

Tsurata, H., Sato, T., Ikeda, N. Mathematical model of cardiovascular mechanics for diagnostic analysis and treatment of heart failure: Part 2 analysis of vasodilator therapy and planning of optimal drug therapy. *Med. & Biol. Eng. & Comput.*, 32, 12-18, 1994.

Wade, O.L. and Bishop, J.M. Cardiac Output and Regional Blood Flow. Blackwell Scientific Publications, Oxford, 1962.

Welch, W.J., et al. Screening, Predicting, and Computer Experiments. *Technometrics*, Vol. 34, No. 1, 15-25, February 1992.

Welkowitz, W. Engineering Hemodynamics: Application to Cardiac Assist Devices, 2nd ed. NYU Press, New York, 1987.

Westerhof, N., Bosman, F., DeVries, C.J., and Noordergraf, A. *Analog Studies of the Human Systemic Arterial Tree.* J. Biomechanics, Vol. 2, 121-143, 1968.

Westerhof, N., Elzinga, G., Sipkema, P. An artificial arterial system for pumping hearts. *Journal of Applied Physiology*, Vol. 31, No. 5, 776-781, November 1971.

White, R.J., Croston, R.C., Fitzjerrell, D.G. Fundamentals of Lumped Compartmental Modelling of the Cardiovascular System. in Cardiovascular Engineering Part I: Modeling (Adv. Cardiovasc. Phys.), D.N. Ghista, ed.Vol. 5, 162-184: S. Kager, Basel, 1983.

White, R.J., Croston, R.C., Fitzjerrell, D.G. Cardiovascular Modelling: Simulating the Human Response to Exercise, Lower Body Negative Pressure, Zero Gravity and Clinical Conditions. in Cardiovascular Engineering Part I: Modeling (Adv. Cardiovasc. Phys.), D.N. Ghista, ed.Vol. 5, 195-229: S. Kager, Basel, 1983.

Whitmore, R.L. Rheology of the Circulation. Pergamon Press, Oxford, 1968.

Wolf, T. An Experimental/Theoretical Investigation of Parallel Inhomogeneities in Respiratory Flows. Ph.D. thesis, Dept. of Mechanical Engineering, Massachusetts Institute of Technology: June, 1990.

Yamaguchi, R., Kohtoh, K. Sinusoidal Variation of Wall Shear Stress in Daughter Tube Through 45 Deg Branch Model in Laminar Flow. *Journal of Biomechanical Engineering.* Vol. 116:119-126, 1994.

Yang, S.S., Bentivoglio, L.G., Maranhao, V., Goldberg, H. From Cardiac Catheterization Data to Hemodynamic Parameters, 3rd Ed. F.A. Davis Co., Philadelphia, 1988.

Yesilyurt, S. Construction and validation of computer-simulation surrogates for engineering design and optimization. Ph.D. thesis, Dept. of Mechanical Engineering, Massachusetts Institute of Technology: April, 1995.

Yesilyurt, S., Patera, A.T. Surrogates for numerical simulations: optimization of eddy-promoter heat exchangers. *Computer Methods in Applied Mechanics and Engineering* 121, 231-257, 1995.

Youngtack, S., et al. Arterial Windkessel Parameter Estimation: A New Time-Domain Method. *Annals of Biomedical Engineering*, Vol. 22, 66-77, 1994.

Zeilke, W. *Frequency-Depenedent Friction in Transient Pipe Flow.* Journal of Basic Engineering. *90*, series D, No. 1, 109 (1968).

Zelis, R., Flaim, S.F. Alterations in vasomotor tone in congestive heart failure. *Prog. Cardiovasc. Dis.* 24:437, 1982.